Title

Tectonostratigraphic reconstruction of the Neoproterozoic rift-to-drift transition in Southeast Death Valley

Author

LOBIANCO, SAMUEL

Publication Date

2022

UNIVERSITY OF CALIFORNIA

Santa Barbara

Tectonostratigraphic reconstruction of the Neoproterozoic rift-to-drift transition in Southeast Death Valley

A Thesis submitted in partial satisfaction of the
requirements for the degree Master of Science
in Earth Science

by

Samuel J. C. LoBianco

Committee in charge:

Professor Francis Macdonald, Chair

Professor Matt Rioux

Professor Phil Gans

December 2022

The thesis of Samuel J. C. LoBianco is approved.

Matt Rioux

Phil Gans

Francis Macdonald, Committee Chair

October 2022

ABSTRACT

Tectonostratigraphic reconstruction of the Neoproterozoic rift-to-drift transition in Southeast Death Valley

by

Samuel J. C. LoBianco

Models for rifting of the supercontinent Rodinia suggest complete separation of the conjugate plate and development of a passive margin sometime from the early-Cryogenian – middle-Cambrian. New tectonostratigraphic reconstructions along two parallel transects in Southeast Death Valley (SEDV) depict a Tonian – Cryogenian rift basin formed against Paleoproterozoic basement. The Ediacaran – middle-Cambrian siliciclastic and carbonate sequence, originally interpreted as recording a tectonically active hinge zone across SEDV, is now constrained in space and time with new chemostratigraphic correlations within a regional and global geochronologic framework. These new tectonostratigraphic data indicate repeated transgressive-regressive stratigraphic sequences from the earliest-Ediacaran – middle-Cambrian atop the craton margin, or rift boundary, and support the model of pre-Ediacaran rifting of southwest Laurentia. Ediacaran unconformities appear to be erosional and the product of large eustatic change rather than Ediacaran reactivation of the rift. Furthermore, reconstruction of this Neoproterozoic basin defines a parautochthonous zone formed against the craton and inverted within the Clark Mountain thrust complex. New U-Pb geochronology from basement exposures in the eastern SEDV distinguish gneissic basement from widespread, highly-strained Mesozoic plutons associated with this crustal shortening and is defined by overlapping Ediacaran unconformities across this zone. New U-Pb geochronological minimum age constraints on ductile deformation in the western transect corroborate the model of basin inversion during Early-Cretaceous Sevier shortening at Clark Mountain.

TABLE OF CONTENTS

ABSTRACT iii
TABLE OF CONTENTS v
LIST OF FIGURES vi
LIST OF TABLES vii

1. INTRODUCTION 1
1.1. Rift-to-drift transition in Southwest Laurentia 1
1.2. Existing tectonic models 2

2. GEOLOGIC SETTING 6
2.1. The Southeast Death Valley rift boundary 6
2.2. Mesozoic & Miocene deformation in SEDV 7
2.3. SEDV Paleoproterozoic – Paleozoic stratigraphy 10
2.4. SEDV Western Transect 14
2.5. SEDV Eastern Transect 18

3. METHODS 21
3.1. Chemostratigraphy 21
3.2. U-Pb zircon geochronology 21
3.3. Subsidence Analysis 22

4. RESULTS 23
4.1. Western SDEV transect 23
4.2. Eastern SEDV transect 31

5. DISCUSSION 37
5.1. Western SEDV transect 37
5.2. Eastern SEDV transect 38
5.3. Implications for timing of 'rift-to-drift' model 39
5.4. Implications for the inversion of Neoproterozoic stratigraphy within the CMTC 42

6. CONCLUSION 44
6.1. Reconstruction of the SEDV Neoproterozoic geology 44
6.2. Tonian – Cryogenian rifting 45
6.3. Early-Ediacaran – Middle-Cambrian transgressive sequences 47

7. REFERENCES 49

8. APPENDIX 78

LIST OF FIGURES

1. SEDV regional geologic map 55
2. SEDV regional stratigraphy & Ediacaran chemostratigraphy 56
3. South Salt Springs geologic map 57
4. South Salt Spring Hills Ediacaran stratigraphy 58
5. Silurian Hills, Halloran Hills & Silver Lake overview geologic map 59
6. Northwest Silurian Hills geologic map 60
7. East Silurian Hills geologic map 61
8. Northwest Silurian Hills & Silver Lake Ediacaran stratigraphy 62
9. North Old Dad Mountain geologic map 63
10. North Old Dad Mountain Ediacaran stratigraphy 64
11. Silurian Hills, Halloran Hills, & Old Dad Mtn. U-Pb geochronology 65
12. Kelso Mountains & Providence Mountains Ediacaran stratigraphy 66
13. SEDV western tectonostratigraphic transect 67
14. SEDV western transect subsidence 68
15. SEDV eastern transect overview geologic map 69
16. Southeast Kingston Range & Winter's Pass Ediacaran stratigraphy 70
17. Northwest Clark Mountain & Mesquite Hills geologic map 71
18. Northwest Clark Mountain Ediacaran stratigraphy 72
19. Winter's Pass & Clark Mountain basement U-Pb geochronology 73
20. SEDV eastern tectonostratigraphic transect 74
21. SEDV eastern transect subsidence 75
22. SEDV Miocene extension reconstruction 76
23. SEDV Neoproterozoic rift basin & inversion 77

LIST OF TABLES

1. List of measured section and sample locations 78
2. List of C and O isotopic data 79
3. List of U-Pb LA-ICP-MS analyses 92
4. Tables of site-specific data in *Backstrip* subsidence calculations 95

1. INTRODUCTION

1.1. Rift-to-drift transition in Southwestern Laurentia

Geologic evidence for the Neoproterozoic break-up of the supercontinent Rodinia is documented on all margins of Laurentia, including in the Death Valley region. The westernmost exposure of Paleoproterozoic basement in southeastern California defines the area from which a conjugate plate to Laurentia rifted and consequently bounds the rift basin(s) formed in between (Hoffman, 1991). The highly variable Death Valley regional stratigraphy records syn-rift sedimentation adjacent to, and unconformably above, Neoproterozoic basement topographic highs in the Death Valley region (Nelson et al., 2020; Macdonald et al., 2013). Although Neoproterozoic extension along the margin began during or directly after the emplacement of the ~778 Ma Gunbarrel LIP (Harlan et al., 2003) and deposition of the Tonian 'ChUMP' basins (e.g., Dehler et al., 2017), the age and geometry of rifting and associated sedimentation remain unclear. Abundant Cryogenian rift-related magmatism has also been described along the western margin of Laurentia from the Yukon, through British Columbia, Washington and Idaho, and into California (Moynihan et al., 2019; Eyster et al., 2020; Isakson et al., 2020; Nelson et al., 2020). Neoproterozoic – Cambrian strata in Southeast Death Valley (SEDV) record the 'rift-to-drift' transition of the SW Laurentian margin, defined as the duration between initial breakup of Rodinia and eventual Paleozoic passive margin. These exposures are the basis for a putative northwest-facing Ediacaran craton-margin 'hinge zone' – a spatial record of this fundamental, but localized, change in tectonic setting (e.g., Fedo & Cooper, 2001).

The complete evolution of the Neoproterozoic – early-Paleozoic Laurentian margin can be summarized in three general phases: (1) initial Tonian – Cryogenian magmatism, and syn-rift pre-glacial and glaciogenic sedimentation recorded in the Kingston Peak Formation (Fm) (e.g., Prave, 1999; Macdonald et al., 2013); (2) development of a wedge-shaped sedimentary package deposited atop these rift deposits during the putative nascent phase of passive margin subsidence in the latest-Ediacaran – Cambrian (e.g., Levy & Christie-Blick, 1991); (3) the development of widespread Paleozoic miogeoclinal and cratonic sedimentary successions across the American Southwest, deposition of which continued until the middle-Paleozoic Antler orogeny (e.g., Stevens et al., 1997). Estimates of the rift-to-drift transition range from: (1) earliest-Ediacaran at ca. 635 Ma (Witkosky & Wernicke, 2018); (2) Late-Ediacaran – Ediacaran-Cambrian boundary (Levy & Christie-Blick, 1991; Fedo & Cooper, 2001); (3) Early – Middle Cambrian (Moynihan et al., 2019).

1.2. Existing tectonic models

Stewart (1970) first described a “remarkable persistence” in the Ediacaran lithostratigraphy overlying the Precambrian Pahrump Group (Gp) and attributed the requisite subsidence to a fully-developed passive-margin setting. Armin & Mayer (1983) suggested that rifting began at ca. 600 Ma and Levy & Christie-Blick (1991) applied a more quantitative subsidence analysis to this model and interpreted “continental separation” between ca. 590-545 Ma, based on Ediacaran sections measured in the Spring, Nopah, Funeral, and Inyo Mountains. These sections are all located to the north of the inferred SEDV Cryogenian basin and, consequently, the subsidence model does not directly account for onlapped Ediacaran stratigraphy there. The authors do note, however, the variability of the regional early-Ediacaran facies and suggest that deposition was likely fault-bounded. Furthermore, they recognized how the early-Ediacaran sequence directly overlies all of the Pahrump Gp map units regionally, including gneissic basement.

Fedo & Cooper (2001) defined the Ediacaran – early-Cambrian rift-to-drift transition across a "hinge zone", based on the broad siliciclastic-carbonate transition in the regional stratigraphy beginning with the Carrara Fm, considered to be deposited at ~540 Ma, following a Precambrian boundary defined at ~570 Ma at the time of publication. The authors also did not know the age of the Cryogenian – early-Cambrian formations and suggested that the rift-drift transition occurred at ~590 Ma, similar to Levy & Christie-Blick (1991), but based on an inaccurate age model. In their model, the late-Ediacaran – Early-Cambrian unconformities (Stirling & Wood Canyon formations) developed due to flexure associated with sedimentation across a passively subsiding hinge-zone through ~540 Ma. Nonetheless, they acknowledge the considerable duration of this transition and define a miogeocline-cratonal transition zone, or formal axis of the hinge, between the Old Dad and Kelso mountains in southern SEDV (Figs. 1, 2).

More recently, Witkosky & Wernicke (2018) used existing biostratigraphic ages of the early Paleozoic carbonates overlying the Neoproterozoic sequence in the greater Death Valley region to produce an exponential, thermal subsidence curve for passive margin subsidence along the incipient continental margin. Their Ediacaran subsidence model is extrapolated back to ca. 635 Ma and the ages they assign to distinct Ediacaran sedimentary horizons are inferred from backstripping of these formations in a thermal subsidence framework. Importantly, their inferred age model defines the upper Johnnie Rainstorm Member (Mb) as deposited ca. 585-579 Ma and places the basal Stirling unconformity at ca. 579 Ma, coeval with the Gaskiers glaciation (Fig. 2). Based on extrapolation of thermal subsidence back to ca. 635 Ma, their model explains deposition of the siliciclastic and carbonate lower-to-middle Ediacaran Johnnie Fm as driven by sediment compaction and the initial, quicker pace of passive margin thermal subsidence, as depicted in the steepest portion of such an exponential curve. In this context, the authors argue that rift-related sedimentation occurred contemporaneously with deposition of the Noonday Sentinel Peak cap carbonate and very top of the syn-rift Kingston Peak Fm.

A complication with the subsidence models described above is how to account for the extreme base level changes and disruption to sedimentary cycling associated with the Cryogenian Snowball Earth events. Not only did these events load and unload the margin with thick icesheets, which would have driven a glacio-isostatic response, but also these glaciations were likely associated with major eustatic change and extreme basin starvation as documented with the uniquely low sedimentation rates during Cryogenian glaciations (Partin & Sadler, 2016; Hoffman et al., 2017; Hoffman, 2022).

Along with the timing of the rift-drift transition, the geometry of the orientation of the rifted passive margin has remained unclear. Fedo and Cooper (2001) depict a NW-facing Ediacaran rifted passive margin whereas Lund (2008) proposes a SW-facing Cryogenian rifted margin. In the Lund (2008) model, the NW margin of the SEDV region is a transform zone. Inconsistencies in these models are often due to one or multiple inaccurate ages for the regional stratigraphy. Distinguishing between these hypotheses requires refining the geometry and timing of Ediacaran – Cambrian unconformities across the proposed hinge zone, along with more thorough identification and correlation of the regional Ediacaran facies changes. A new age model is possible because of new direct geochronological constraints on Neoproterozoic stratigraphy both locally (Nelson et al., 2020) and globally (Rooney et al., 2020; Yang et al., 2021) that help further refine the Ediacaran-Cambrian history of basin fill across SEDV (Fig.

2). The study presented herein mapped and described these inverted strata, in order to reconstruct the margin of the Neoproterozoic basin in space and better constrain the rift-to-drift model for southwestern Laurentia in time. Ediacaran sedimentary sections were measured in two separate transects, focusing on the Cryogenian – Ediacaran transition recorded in the Ediacaran Noonday and Johnnie formations exposed across Fedo and Cooper's (2001) hinge zone (Fig. 1).

2. GEOLOGIC SETTING

2.1. The Southeast Death Valley rift boundary

SEDV extends south of Death Valley proper and runs ~NNW-SSE from the Salt Spring Hills and Kingston Range in the north to the Marble and Ivanpah mountains in the south (Fig. 1). Miocene – present extensional tectonics and magmatism define the topography throughout (Wernicke and Snow, 1998; Hodges et al., 1989) and the dextral Death Valley shear zone and associated Garlock fault separates the Southern California Cordillera into the Mojave and Sierran blocks, restoration of which places Death Valley proper directly ~NNW of the Mojave segment (Wernicke et al., 1990).

Proterozoic rift boundaries broadly define the original western Laurentian margin and bound some of the earliest sedimentary basins (Macdonald et al., 2022). The Neoproterozoic – Cambrian strata record the formation of sub-basins during incipient rifting of the Rodinia supercontinent (Eisbacher, 1983; Hoffman, 1991; Prave, 1999) and the overlying Paleozoic succession records the development of a passive margin, characterized by the transition to a thermal decay curve in subsidence models and widespread deep-water carbonates (Levy & Christie-Blick, 1991). Preservation of the westernmost basement exposed in the Cordilleran hinterland along with the Neoproterozoic syn-rift sedimentary succession in various Mesozoic thrust plates (Burchfiel & Davis, 1971) provides a window into the relationship between the western Laurentian margin, Paleoproterozoic craton, and continental arc (Decelles, 2004; Yonkee & Weil, 2015).

Recognition of an abutting relationship between these Mesozoic structures and inferred Neoproterozoic paleo-highs and lows suggests buttressing between the cratonal margin and the thickening continental arc during Mesozoic hinterland shortening (Dunne & Walker, 2004).

The eastern boundary of this crustal shortening is delineated along the ancient rift boundary, or cratonal margin. Here, Paleoproterozoic 'Ivanpah' gneissic basement extends ~NNW-SSE in eastern SEDV (Fig. 1) and is the nucleus of both shortening and extension in the Mojave crust from the Mesoproterozoic – present. A similar relationship has been documented in the Central Cordilleran "Wasatch hinge line", a northern extension of the same Neoproterozoic rift system that defines formation of the western continental margin and is now similarly distended by basin-and-range extension (Yonkee et al., 2014). Classically, crustal shortening during Mesozoic Cordilleran tectonism in SEDV is thought to have driven the inversion of a broad Neoproterozoic – Paleozoic miogeocline within the Clark Mountain thrust complex (CMTC) (Burchfiel & Davis, 1971). Questions around the geometry of this basin and the complex lateral facies variations of its infill remain, which limit regional correlation with other Late Jurassic – early-Cretaceous 'Nevadan' and late-Cretaceous 'Sevier' deformation documented in adjacent ranges (Walker et al., 1995; Giallorenzo et al., 2018). Miocene basin-and-range extension further complicates restoration of these folded, inverted strata across a now highly distended, rotated, and intruded Mojave crust (Friedmann et al., 1995).

2.2. Mesozoic & Miocene deformation in SEDV

Mesozoic thrusting and associated magmatism throughout SEDV deform much of the Proterozoic – Paleozoic geology and complicates reconstruction of the pre-Cordilleran environment. Permian – earliest-Triassic granitic plutonism in the El Paso Mountains (Stevens et al., 1997) and Cottonwood Mountains (Snow, 1992) indicate eastward-dipping subduction beneath the southern California margin by this time, followed by the development of a regional Triassic – early-to-middle-Jurassic continental arc documented across the region. ~100 Ma

Sierran magmatism and late-Cretaceous magmatism is also widespread (e.g., Dunne, 1977; Busby et al., 2002).

The two major Mesozoic deformational events, the Sevier and Laramide orogenies, are broadly defined in the hinterland (e.g., Wells & Hoisch, 2008; Decelles, 2004; Yonkee & Weil, 2015). Late Jurassic – early-Cretaceous "Sevier" deformation in the retroarc region is differentiated from "Nevadan" deformation in the California forearc (e.g., Giallorenzo et al., 2018). Originally defined in the Klamath Mountains in the Pacific Northwest (e.g., Ingersoll & Schweikert, 1985), "Nevadan" deformation has generally been considered to extend no farther than the central Sierra Nevada (Tobisch et al., 1987), due to the overlapping nature of the Permian Death Valley fold-thrust belt (Snow, 1992), southern Jurassic Eastern Sierran thrust system (ESTS) (Dunne & Walker, 2004), and adjacent Sevier fold-thrust belt (Hoisch et al., 2014; Yonkee and Weil, 2015). Interpretations of surrounding late-Jurassic thrust systems in the southern Sierra and Death Valley region has generally been attributed to the ESTS (Affinati et al., 2020). Dunne & Walker (2004) interpret the protracted evolution of the system (~50 myr) to "episodic underthrusting" of the lithosphere behind the Sierran continental arc and, most importantly, a buttressing effect of the cratonic margin to the east. This shortening in the eastern Mojave is taken up by inversion of the Neoproterozoic – Paleozoic sub-basins and overlying passive margin supersequence against the Ivanpah basement along the CA-NV border in the CMTC (Fig. 1).

The CMTC was originally interpreted to represent a stack of 3 allochthonous thrust plates: (1) thick-skinned Winter's Pass thrust; (2) thick-skinned Mesquite thrust; and (3) thin-skinned Keystone thrust (Burchfiel & Davis, 1971). Shortening within the Mojave segment of the Sevier belt began during the latest-Jurassic in the CMTC and terminated by ca. 140 Ma

(Giallorenzo et al., 2018). The complex is uniquely located at the intersection of the Mesozoic magmatic arc, the ESTS, and Sevier thrust belt, and exhibits a combination of foreland and hinterland deformation styles (Walker et al., 1995; Burchfiel & Davis, 1971). The CMTC consists of an eastern autochthon composed of gneissic basement and Cambrian – Jurassic cratonal sedimentary cover. Importantly, the strata in the structurally higher allochthonous plates were deposited across the transition zone between cratonal Paleozoic sequences and "miogeoclinal" Neoproterozoic – early-Paleozoic strata, in contrast to the autochthonous strata with a cratonal affinity and overlying Jurassic siliciclastics (Fedo & Cooper, 2001). Therefore, each overlying allochthon must restore to the west from beyond the Neoproterozoic – Cambrian hinge zone on the proto-Laurentian margin, prior to Cenozoic extension. Walker et al. (1995) mapped and described the complicated relationships between the extremely deformed Ediacaran – Cambrian strata on the west side of Clark Mountain, collectively referred to as the Pachalka thrust. Their U-Pb ages on cross-cutting relationships between the strata and granite plutons at Pachalka Springs constrain movement along the thrust there to between ~147-142 Ma, part of the earliest Sevier shortening documented in the region, in addition to pre-140 Ma crustal thickening in the Funeral Mountains to the north (Giallorenzo et al., 2018).

Today, Death Valley and the greater Mojave region are entirely controlled by extensional tectonics and block rotation as part of greater basin-and-range extension in the American Southwest and translation along the San Andreas fault zone (Wernicke and Snow, 1998). Restoration of the associated deformation is crucial to understanding the spatial and temporal relationships within the Neoproterozoic – Paleozoic SEDV strata. The most prominent Miocene structure in the SEDV is the north-south-trending Kingston-Halloran detachment system that cuts through the CMTC, and its associated west-dipping detachments and strike-slip systems have dispersed blocks of the deformed Neoproterozoic – Paleozoic strata. These 'slide blocks' have been primarily transported westward from the CMTC across the adjacent Shadow Valley and, in some cases, translated along regional shear zones, such as the Salt Spring Hills and eastern Avawatz Mountains strata (Fig. 1). These slide blocks exhibit large <50 cm mega-breccias along their boundaries and often internally, indicative of significant brittle deformation throughout. Slide blocks in the SEDV and especially Shadow Valley are remarkably low-angle for being extensional structures, a geometry thought to be generated by block and fault plane rotation during syn-extensional intrusion and crustal uplift associated with the km-scale Miocene Kingston pluton in northern SEDV (Friedmann, 2005; Spencer, 1990) (Fig. 1).

2.3. Southeast Death Valley Paleoproterozoic – Paleozoic stratigraphy

The Death Valley regional stratigraphy records nearly 2 billion years of basin formation events and tectonism along the southwestern corner of the Archean – Paleoproterozoic North American craton. The Mesoproterozoic – Cryogenian Pahrump Gp overlies basement composed of Paleoproterozoic paragneiss and orthogneiss deformed by the regional ~1.7 Ivanpah orogeny (Wooden and Miller, 1990; Whitmeyer and Karlstrom, 2007). The eponymous ~NNE-SSW-trending Ivanpah basement exposure in the eastern SEDV is both the structural and topographic backbone of the SEDV from Winter's Pass to the Ivanpah Mountains (Fig. 1).

In SEDV, this basement is unconformably overlain by the Mesoproterozoic Crystal Springs Fm, which thickens to the northwest in present coordinates (Roberts, 1985) and records

Mesoproterozoic foreland basin development to the SE margin of Laurentia (Whitmeyer & Karlstrom, 2007; Mulder et al., 2017). This mixed siliciclastic and carbonate sequence is dominated by relatively coarse-grained siliciclastic rocks in the lower members, and the upper members preserve stromatolites and host talc deposits derived from hornfels metamorphism during intrusion of the ~ 1.1 Ga Crystal Springs diabase (Heaman and Grotzinger, 1992). A >300 Myr unconformity separates the Crystal Springs Fm from the unconformably overlying Tonian Horsethief Springs Fm (Macdonald et al., 2013; Mahon et al., 2014). The Horsethief Springs Fm and overlying Beck Springs Fm (ca. 750-735 Ma) are separated from the underlying Crystal Springs Fm by a regional Tonian unconformity and record the development of a Tonian basin in the SEDV with an inferred facing direction to the present NE (Smith et al., 2016; Maud, 1983). The Horsethief Springs, Beck Springs, and putative Beck-equivalent Silurian Hills sandstone are documented in northwest SEDV at the Kingston Range and in western SEDV at the Silurian Hills, respectively (Kupfer, 1960; Comstock, 1997; Smith et al., 2016), but have not been observed within any Pahrump Gp outcrops farther to the southeast. Furthermore, the Tonian units have not been defined in the eastern and southeastern corridor, either adjacent to or atop the Paleoproterozoic Ivanpah basement (Figs. 1, 2).

The overlying Kingston Peak Fm is well-known for its diverse glaciogenic diamictite facies which record one or both of the Cryogenian 'Snowball Earth' events: (1) Sturtian (~720-660 Ma); (2) Marinoan (~650-635 Ma) (Miller et al., 1985; Prave, 1999; Macdonald et al., 2013; Nelson et al., 2021). Recently, these two members of the Kingston Peak Fm have been bracketed in time with new U-Pb ages north of SEDV in the Panamint Range (Nelson et al., 2020) (Fig. 2), although attribution of the Kingston Peak Fm facies in SEDV at the Silurian Hills and Kingston Range to either the first or second glaciation remains uncertain (Macdonald et al., 2013). The Kingston Peak diamictite is unique relative to the Mesoproterozoic Pahrump Gp stratigraphy and younger Ediacaran – Cambrian sequence in that it outcrops in concentrated, inferred sub-basins throughout SEDV. These inferred depocenters, rift-related km-scale olistostromes, associated mega-breccias, and regional pillow basalts is the basis for the consensus interpretation of an active rift setting in the Cryogenian during already variable diamictite deposition (e.g., Macdonald et al., 2013; Prave, 1999).

The basal Ediacaran Sentinel Peak Mb of the Noonday Formation outcrops prominently across the SEDV with facies varying from thick stromatolitic dolostone (>100 m) to thin (<1 m) dolo-arenites obscured within thick (>100 m) turbidite sequences (Petterson et al., 2011). Together with the upper Noonday Radcliffe Mb, these facies all record post-Cryogenian cap carbonate deposition from ca. 635 – 630 Ma during the post-Marinoan glacial transgression (Nelson et al., 2020), with concentrations of carbonate and siliciclastic deposition varying locally within the transgressive sequence (Summa, 1993). The Ediacaran mixed siliciclastic and carbonate strata of the Johnnie Fm overly the Noonday Fm and have been differentiated in multiple ways, due to the complicated lateral facies variations and unconformable relationship with the units. Stewart (1970) originally defined the Radcliffe as a "transitional" lowermost member in the Johnnie Fm, with 5 additional members defined throughout the formation based on differentiation of coarse siliciclastics, fine siliciclastics, and the presence of dolostone beds. The middle member is most regionally diverse with alternating carbonate or siliciclastic-dominated packages on anywhere from ~10-100 m-scales and in different orders. The upper member, or Rainstorm Mb, is better exposed regionally and is marked at the base by the distinctive Johnnie oolite which records the Shuram carbon isotope (δ^{13}C) excursion, now dated globally at ca. 570 Ma using Re-Os and U-Pb geochronology (Rooney et al., 2020; Yang et al., 2021) (Fig. 2). The transgressive Rainstorm Mb outcrops across SEDV more than the lower Johnnie members (Stewart, 1970), with the top contact incised by the Stirling quartzite over ~100m deep in some places (Clapham and Corsetti, 2005).

Stewart (1970) correlated the uppermost Rainstorm Mb regionally, but did not for the underlying five members defined only by their local facies. In a comprehensive thesis on the Johnnie Fm, Summa (1993) proposed two generalized groupings for the Johnnie facies, the lower consisting of Stewart's (1970) transitional, quartzite, and lower carbonate-bearing unit. The second was defined at the first distinct siltstone interval in the Johnnie with a second overlying carbonate-bearing unit, before the regionally distinct Rainstorm Mb and oolite. Importantly, Summa (1993) interpreted regionally-correlative transgressive sequence tracts within the Johnnie Fm and associated exposure surfaces as recording active tectonism and episodic tectonic subsidence well past ca. 635 Ma and through most of the Ediacaran.

The Johnnie Fm extends farther south than the southernmost Noonday exposures where its younger members sit progressively and unconformably atop basement. Both the overlying Stirling (~560-540 Ma) and Wood Canyon formations (~540-510 Ma) also begin with basal unconformities exposed across the entire SEDV and exhibit similar shallow marine mixed siliciclastic and carbonate facies that pinch out to the SE (Fedo & Cooper, 2001; Stewart, 1970). Together, these Ediacaran unconformities record "backstepping" of coeval carbonate and shallow siliciclastic platforms to the southeast, well beyond the extent of the Tonian – Cryogenian units and farther than early-Ediacaran onlapping directly adjacent to the Tonian – Cryogenian basin. The Cambrian Wood Canyon Fm records the development of distal fluvial and shallow marine strata between the incipient passive margin and cratonal interior and is, again, unconformably overlain by the late-Cambrian Zabriskie Fm, the final siliciclastic-dominated unit in the early-Paleozoic stratigraphy (Fedo & Cooper, 2001). The overlying Carrera (~510-504 Ma) and late-Cambrian Bonanza King formations begin this early-Paleozoic carbonate supersequence that mantles the Paleoproterozoic craton to the southeast. The Paleozoic Good Springs, Sultan, Monte Cristo, and Bird Springs formations are documented across SEDV (e.g., Dunne, 1977), sitting both along and behind the fully-developed tectonostratigraphic hinge zone and deposited definitively after the rift-to-drift transition in SW Laurentia along the Paleozoic passive margin (Levy and Christie Blick, 1991; Fedo & Cooper, 2001).

2.4. SEDV Western Transect

Together, the north and south Salt Spring Hills expose the complete Ediacaran – Cambrian SEDV stratigraphy. In the southern Salt Spring Hills, the Ediacaran units have been measured and described in detail by Stewart (1970) and Summa (1993), but not differentiated by stratigraphic member at map-scale. The full Pahrump Gp is exposed at the Silurian Hills with the basal Crystal Springs Fm overlying gneissic basement and the full Tonian sequence above. Kupfer (1960) originally mapped the Silurian Hills with numbered units differentiated by facies which have since been assigned to the regional stratigraphy (Smith et al., 2016; Le Heron et al., 2017). The ~500 m thick Crystal Springs Fm unconformably overlies basement with a ~50 m thick cobble-to-pebble conglomerate that grades upward into a quartzite. The overlying mixed siliciclastic and carbonate facies consist of the Crystal Springs Fm unconformably overlain by the Tonian Horsethief Springs Fm In the southernmost South Salt Spring Hills, the Kingston Peak Fm is exposed with no base, although some of the underlying Pahrump Gp rocks are faulted against Mesozoic plutons in the Avawatz Mountains ~3 km to the west at Sheep Creek with a significant distance of quaternary cover in between (Fig. 1). Here, and at the Silurian Hills, the Cryogenian Kingston Peak Fm is underlain by the putative Beck-Springs equivalent Silurian Hills Sandstone (SHS) (Smith et al., 2016). The Kingston Peak records a ~1.5 km thick diamictite section with three distinct olistolith-bearing units (Le Heron et al., 2017). The thick (>1.5 km) sequence of diamictite and overlying section of the Ediacaran – Cambrian Death Valley stratigraphy are best exposed in the northwest.

The "Riggs thrust" was originally defined by Kupfer (1960) in the southeastern corner of the Silurian Hills above a highly strained metamorphic core complex. The thrust was invoked to explain the juxtaposition of massive km-scale blocks of isoclinally folded, brecciated 'Riggs' carbonate above the metasediments. Comstock (1997) built off of this work and suggested a "polyphase Mesozoic ductile deformation" in the Silurian Hills to explain his observations of four discrete metamorphic domains within the core of the hills, although focused more specifically on Cenozoic overprinting of these older Mesozoic structures, including clockwise basin-and-range block rotation associated with the southern Death Valley shear zone. East of the Silurian Hills, the Shadow Valley basin formed above the Kingston-Halloran Hills crustal detachment system where only some of the regional strata is exposed (Davis et al. 1993; Friedmann et al. 1996). The Shadow Valley basin was active between 13.5 – 7 Ma and filled with 2.5–3.5 km of landslide breccias and km-scale low-angle slide blocks (Friedmann, 1997).

The Halloran Hills are the most prominent exposure of gneissic basement in western SEDV (Fig. 1). Discordant U-Th-Pb dates ranging from ~1.7-1.8 Ga confirm the Ivanpah-related basement domain here, in addition to numerous Jurassic-Cretaceous plutons associated with the adjacent Mesozoic arc to the west (DeWitt, 1984). Ediacaran metasediments in the

Halloran Hills are poorly exposed, but are best exposed immediately to the west in the hills north of Silver Lake where Stewart (1970) measured a section of Johnnie, Stirling, and lower Wood Canyon formations without an exposed base. Given the uncertain thickness of the Johnnie Fm, but a clear erosive unconformity with the basal Stirling Fm, Stewart (1970) suggested that the exposed Johnnie Fm at Silver Lake is a portion of the upper Rainstorm Mb. At both Halloran and Silver Lake, thick >100 m blocks of marbleized Paleozoic carbonates are faulted against basement and older meta-sediments, although nearly all are deformed beyond recognition and have historically been lumped by all workers and defined as the "Riggs carbonates" given their proximity to the southern Silurian Hills (Kupfer, 1960).

Approximately 30 km south of Halloran Hills, Old Dad Mountain preserves Ediacaran strata deposited unconformably on gneissic basement (Dunne, 1977; Bergmann et al., 2011), although the Ediacaran – early-Cambrian stratigraphy has not been detailed on a map-scale due to widespread intrusions in the basement and Neoproterozoic stratigraphy. Dunne (1977) originally described the Old Dad stratigraphy with an emphasis on the thick (> 2km) sequence of ridge-forming Paleozoic carbonates and their structural relationship with the undifferentiated Neoproterozoic – Cambrian stratigraphy below. Additionally, Dunne (1977) mapped small outcrops of Jurassic Aztec sandstone in southern Old Dad atop the Permian Bird Springs Fm. Similar to the "Riggs thrust" at Silurian, the "Playground" thrust was originally mapped as the major structure at Old Dad responsible for the km-scale isoclinal folding of the upper carbonates, although exposures of the actual ductile surface are limited and are mostly obscured by the local brittle fault systems and Neogene landslide deposits that bound the flanks of Old Dad Mountain. Dunne (1977) did not correlate the Playground thrust with a specific regional thrust, but suggested it may be the southern continuation of one of the eastern Mojave thrust systems described at the time as “anastomosing” along strike in-and-around the CMTC (Burchfiel & Davis, 1971).

Southeast of Old Dad Mountain, the Kelso Mountains consist of gneissic basement intruded by Mesozoic granitoid plutons and distended along Miocene extension associated with the Cima volcanic field (Fig. 1). The major basement domain at southeastern Old Dad Mountain is separated from the exposed basement in the Kelso Mountains by the southernmost extension of the Cima field. Stewart (1970) originally described the Johnnie Fm at Kelso, but did not report Stirling or Wood Canyon thicknesses. Fedo and Cooper (2001) further distinguished the Johnnie, Stirling, and Wood Canyon formations at in the Kelso Mountains with measured sections and facies descriptions, and Miller et al. (2003) mapped undifferentiated pockets of Neoproterozoic outcrops in the Kelso Mountains, highlighting the limited preservation of the Neoproterozoic strata there.

The Providence Mountains are ~15 km southeast of Kelso and expose the full Ediacaran – early-Paleozoic stratigraphy dissected by systems of basin-and-range normal faulting (Stone et al., 2017). Fedo and Cooper (2001) described the decreasing thickness of the Ediacaran strata moving southeast from Old Dad, to Kelso, and finally the Providence Mountains, beyond which the Johnnie, Stirling, and Wood Canyon formations all taper and eventually disappear at the Marble Mountains. Approximately 25 km to the southeast, the late-Cambrian Wood Canyon to Zabriskie-equivalent Tapeats sandstone sits on basement, marking the first depositional contact between gneissic basement and the classic North American Paleozoic strata documented farther east within the continental interior (Fig. 1).

2.5. SEDV Eastern Transect

The Kingston Range is the eponymous location for the Cryogenian diamictite and is where the most dramatic olistolith exposures are mapped (Macdonald et al., 2013). Similar to the Silurian Hills, the full Pahrump Gp is exposed atop gneissic basement in the Kingston Range, although the Beck Springs Dolomite sits between the Horsethief Springs Fm and Kingston Peak diamictite, rather than the coeval Silurian Hills sandstone in the western SEDV transect (e.g., Smith et al., 2016) (Fig. 2). In the northern exposures of the Kingston Range, Noonday rests progressively the Horsethief Springs Fm, Kingston Peak Fm, and basement marking a major unconformity developed during the Cryogenian, presumably related to rifting (Macdonald et al., 2013; Smith et al., 2016). Ediacaran – early-Cambrian units were measured in the central and western Kingston Range by Stewart (1970) and Summa (1993), respectively. Their sections were nearly equivalent in thickness, although some subtle variation in the variable middle Johnnie carbonates and siliciclastics were noted, despite neither worker splitting the facies along member boundaries, similar to their generalized sections measured at the Salt Spring Hills and Silurian Hills.

Winter’s Pass is marked by the roadway running from the Kingston-Halloran valley to the Pahrump Valley on the CA-NV border (Fig. 1). The road runs through a valley where the km-scale Winter’s Pass thrust juxtaposes mylonitized gneissic basement against portions of the Ediacaran and Paleozoic stratigraphy. The western side of the pass, or upper plate of the thrust (Burchfiel and Davis, 1971), preserves the full Ediacaran stratigraphy deposited directly on basement with no exposed Pahrump Gp. Stewart (1970) measured a full section from the basement to lower-Cambrian units in the northernmost Winter’s Pass Hills where the stratigraphy is most tractable, although little differentiation of the stratigraphy overlying basement in the southern Winter's Pass area has been proposed. The central Winter's Pass Hills are cored by a large block of gneissic basement similar in scale to the basement at the Halloran Hills (Fig. 1). The Winter's Pass basement has not been previously dated and, instead, the uniform Ediacaran unconformity in the north and Ivanpah-related augengneiss domain in the west of the complex have served as the basis for distinguishing between 'Ivanpah' gneiss and syn-kinematic Mesozoic orthogneiss documented to the southeast at the Pachalka thrust at northwest Clark Mountain (Walker et al., 1995) (Fig. 1).

The Mesquite Hills begin south of the road leading over Winter's Pass and continue south to Powerline Road, in the valley north of Clark Mtn. (Fig. 1). The Mesquite Hills are one of the least studied areas in SEDV due to their complicated isoclinally folded stratigraphy, together referred to as the "anastomosing" 'Mesquite thrust' (Burchfiel and Davis, 1971). The ductile structures running through the hills sit structurally in between the parautochthonous stratigraphy of the Winter's Pass block and the middle-Cretaceous Keystone thrust mapped directly against the Ivanpah basement in easternmost SEDV and beyond (e.g., Walker et al., 1995). Burchfiel and Davis (1971) first described the ductile deformation in the Mesquite hills as distinct from the adjacent blocks due to obvious structural relationship with the underlying Keystone plate and the dramatic differences in facies relative to the Winter's Pass stratigraphy immediately to the northwest. The same fold-and-thrust belt deforming Ediacaran – Paleozoic strata continues along strike to northwest Clark Mountain, where the only exposures of the early Ediacaran stratigraphy in the greater Clark Mountain area are exposed. Here, a relatively homogenous orthogneiss has been interpreted as basement uplifted within an easternmost sliver of the Winter's Pass thrust, directly adjacent to undifferentiated early Ediacaran stratigraphy with no Pahrump Gp exposed (Fig. 1).

The Ivanpah Mountains are directly southeast of Clark Mountain and are located at the southern exposure of the Ivanpah basement segment that bounds eastern SEDV (Fig. 1). Similar to the Marble Mountain, the Ivanpahs are the first location in the eastern SEDV transect where proper North American cratonal Cambrian strata has been documented. Here, the Zabriskie-equivalent Tapeats sandstone mapped farther east in the interior of the craton sits atop Ivanpah basement and beneath regional Paleozoic carbonate supersequence. Additionally, the Paleozoic sequence is unconformably overlain by the Jurassic Aztec sandstone, another distinct sedimentary unit with North American cratonal-affinity. The Ivanpah Mountain are deformed by Mesozoic shortening and magmatism, although only the middle-late-Cretaceous thrusting in the 'Keystone' plate extends this far southeast, constrained by dates on the Cretaceous Ivanpah pluton and Delfonte volcanics (Gans, 1974; Walker et al., 1995).

3. METHODS

3.1. Chemostratigraphy

Chemostratigraphy, specifically $\delta^{13}C$ ratios, allows for temporal correlation across differing regional carbonate facies. Here, $\delta^{13}C$ values were used to correlate the various carbonate facies of the Middle and Upper Johnnie Fm across the active rift environment of the Ediacaran SEDV. Stratigraphic sections were measured and carbonate samples were taken at ~1 m intervals within all carbonate-bearing intervals of the Noonday and Johnnie formations. The samples were drilled and powdered at UCSB and carbonate powders were processed using mass-spectrometry at UC Berkeley (UCB). See appendix for UCB Center for Stable Isotope Biogeochemistry $\delta^{13}C$ analytical methods and full list of all $\delta^{13}C$ analyses presented in this study (Table 2).

3.2. U-Pb Zircon Geochronology

U-Pb zircon geochronology was performed using the laser ablation-inductively coupled plasma-mass spectrometry (LA-ICP-MS) system at the University of California, Santa Barbara (UCSB). All samples were crushed and sorted using a jaw-crusher and 500 μm sieve. <500 μm material was then density-sorted using a standard sorting pan until individual zircon could be directly picked under a microscope. For undeformed intrusive samples, ~500 representative grains were selected from relatively homogenous populations. For gneissic basement samples, ~500 grains were selected to represent the range of morphologies and with a preference against metamict grains that were too fragmented and damaged to remain intact during the picking and polishing processes. Grain mounts were polished with increasingly fine grit paper and carbon coated for imaging. All grains were imaged with cathodoluminescent imaging (CL) on a scanning election microscope at UCSB to identify grain morphologies. LA-ICP-MS analyses of the zircon grains were run following established analytical methods (Kylander-Clark et al., 2013; Johnston & Kylander-Clark, 2021). The data was reduced using *Iolite* data reduction software. Reduced radiometric $^{206}Pb/^{238}U$ and $^{207}Pb/^{235}U$ values were plotted using the open-source *IsoplotR* program (Vermeesch, 2018) to calculate ages for each respective zircon population (Table 3).

3.3. Subsidence analysis

Subsidence analyses were produced using the open-source *Backstrip* subsidence modeling software. For each subsidence curve, measured and compiled thicknesses at each field site were tabulated along with relevant information regarding sediment porosity, grain size, water depth at deposition, and the presence of any unconformities or erosive surfaces. Measured thicknesses and facies types were encoded specifically to each locality and, for localities without exposed Paleozoic carbonate sequences, data from the complete Paleozoic section at Clark Mtn. were applied. See appendix for location-specific input values and measured Ediacaran section thicknesses by unit (Table 4).

4. RESULTS

4.1. Western SEDV transect

Salt Spring Hills

In the southern Salt Spring Hills, the entire Pahrump Gp below the Kingston Peak Fm is faulted out by dextral translation along the Death Valley shear zone, against the Avawatz Mtns. Here, an associated system of normal faults displaces the Ediacaran stratigraphy down to the southwest with relatively minimal offset that does not affect the coherence of the exposed strata (Figs. 3, 4). The exposed upper diamictite is >100 m thick with a gradational interval from diamictite to the lowermost Ediacaran units dominated by turbidites. Granitic intrusions are mapped to the west and north, although there is no evidence for the dramatic ductile deformation found elsewhere in SEDV. A brief interval of cover mapped within the most recessive lower Ediacaran units may be controlled by a similar small scale brittle fault, although bedding measurements do not change across this interval. A composite section (SLS2106, '08) was measured through the upper Kingston Peak, Noonday, Johnnie, and lower Stirling formations. Samples for $\delta^{13}C$ isotopic analyses were taken at a ~0.5-1 m resolution where dolomite beds and sufficiently dolomitic calc-arenites were measured (Figs. 3, 4).

The upper ~20 m of the Kingston Peak diamictite is massively bedded and poorly sorted with cm-scale outsized clasts and conglomeratic lenses. In the final ~5-10 m, this arkosic grit grades into similarly composed <1 m thick turbidites with ~10 cm-scale fine sand-to-silt capping each turbidite sequence. Above this ~10 m turbiditic interval, a distinct ~10-20 cm thick pale yellow fine-grained dolo-micrite is exposed within the uppermost arkosic-grit turbidites. This bed is not repeated and the overlying strata grades into a darker, massively bedded gritty sandstone that fines upward for ~15 m, before a ~40 m package of increasingly coarse, decreasingly arkosic, and increasingly dolomitic turbidites. This sequence grades upward into a ~50 m fine-grained sand and siltstone interval that is increasingly recessive and eventually disappears beneath ~10 m of cover below the base of the lower Johnnie Fm. New mapping differentiates the various Ediacaran units and, specifically, the three distinct members of the Johnnie Fm exposed in the south. The lowermost Johnnie 'grit' unit is both the most conspicuous and homogenous unit, with varying siliciclastic and carbonate facies continuing throughout the middle and upper Johnnie Fm above a distinct flooding surface atop the grits (Figs. 3, 4).

Both the lower and middle Johnnie Fm facies are distinct from regional 'type' localities. Here, the Lower Johnnie 'grits' are ~75 m thick, coarse, and exhibit little-to-no bedding. The grit facies vary little throughout the entire unit although they do fine upwards into a weakly-bedded, coarse-grained quartzite before a sharp flooding surface and the conformable deposition of the lowermost Middle Johnnie dolomites (Fig. 4). Differing from its more siliciclastic-dominated regional facies (e.g., Summa, 1993), the Middle Johnnie Fm here is composed of primarily of carbonate, with two distinct ~30 m thick pages of ~1-3 m thick dolomite beds with interbedded fine sands, silts, and gritty calc-arenites. The upper Middle Johnnie siltstone and sandstone coarsens upwards, grading into the conspicuous 'Johnnie oolite' bed that marks the beginning of the upper Johnnie Rainstorm Mb. A sharp flooding surface above the oolite begins a ~50 m interval of coarsening and increasingly calcareous silts and sands, before the erosive basal Stirling Fm unconformity. Carbon isotopic values measured through the middle and upper Johnnie Fm are mostly positive-to-neutral before the deeply negative 'Shuram' excursion (Figs. 2, 4) beginning with the oolite and continuing through the upper Rainstorm Mb calc-arenites. The unconformably overlying

Stirling Fm irregularly cuts down into the upper Rainstorm Mb on a ~5 m-scale with its distinct pebble-to-cobble conglomerate, slivers of which are faulted down against the Johnnie (Figs. 3, 4).

Silurian Hills

The entire Pahrump Gp and Ediacaran – Cambrian sequence is exposed at the Silurian Hills with gneissic basement also exposed in both the east and west (Figs. 5 – 7). While the isoclinal folding and metamorphism within the undifferentiated Riggs carbonate is indeed extreme and 'chaotic' (Kupfer, 1960), the carbonates are heavily brecciated throughout and, importantly, along their contact with the underlying Pahrump Gp and Ediacaran formations. This Riggs surface, when mapped around its brecciated perimeter, outlines a relatively flat, klippe-style geometry between the upper and lower blocks, bound by heavily brecciated contacts indicative of a major brittle deformational event. Furthermore, when restored, normal fault block rotation of each consecutive westward dipping normal fault across the hills, restores a collective Riggs surface with a clearly westward-dipping normal fault plane, equivalent to the similarly massive, westward-directed slide blocks and mega-breccias directly east in Shadow Valley (Friedmann, 1997). The Riggs detachment surface, itself now faulted by higher angle, westward-directed normal faults, variably cuts out the full Mesoproterozoic – Paleozoic stratigraphy in segments across the hills. Blocks of the Riggs carbonates also cut the Silurian Hills granite, which is mapped throughout the hills cutting the extreme ductile deformation in all units (Figs. 6, 7).

Ductile deformation in the southern and eastern hills is most extreme. Identification of the Riggs carbonate as a Kingston-Halloran detachment-derived slide block, eliminates the need to explain deformation in the carbonates and within the underlying Pahrump Gp rocks in the same framework. The coherent Pahrump Gp and Ediacaran – early-Cambrian stratigraphy underlying the Riggs carbonates – the 'lower plate' in reference to its position within the slide block system – exhibits a broad antiformal geometry. This structure is best seen in cross-section on the western side of the hills, where a core of gneissic basement is exposed with a complete overlying stratigraphy to the north and attenuated and incomplete section to the south (Fig. 6). The greatest deformation in the hills is concentrated in the south where greenschist and amphibolite grade deformation is mapped adjacent to the largest exposure of the Silurian Hills granite (Fig. 7). Attenuation of the entire stratigraphy can also be clearly seen in cross-section, with the greatest thinning occurring in the southern hills. Building off of Kupfer's (1960) and Comstock's (1997) mapping of the hills, a newly differentiated Pahrump Gp and Ediacaran – early-Cambrian stratigraphy has been defined here. The Cryogenian –Cambrian sequence is best exposed in the northwestern hills where there is less metamorphism and ductile deformation. In a large fault block adjacent to isoclinally folded Johnnie and Stirling formations, a composite section was measured through the upper Kingston Peak Fm to the lower Stirling Fm (Figs. 6 – 8).

Here, the uppermost ~10 m of the Kingston Peak Fm is massively bedded with large cobble to boulder-sized clasts, grading into a gritty arkosic sandstone in the uppermost meters before sharp contact with a yellow dolo-micrite that immediately begins to grade into a dolo-arenite, then grit. This ~2-3 m thick yellow dolomitic interval – the inferred ~635 Ma Sentinel Peak Mb cap carbonate – is not repeated and the overlying Radcliffe Mb grit immediately grades into an arkosic turbidite sequence with ~0.1-0.5 m thick beds for ~100 m. Similar to the Salt Spring Hills, the full Noonday Fm in the Silurian Hills has a thin, micritic Sentinel Peak cap carbonate and is gradationally overlain by a thick, arkosic, and turbiditic Radcliffe Mb. The overlying lower Johnnie Fm grits are also very similar to exposures in the Salt Spring Hills with massive, poorly sorted, coarse quartz-rich grit and pebble conglomerate grading out of the upper Radcliffe Mb turbidites and silts. The overlying middle Johnnie Fm is thinner here than at the Salt Spring Hills, and a single sequence of slightly positive δ^{13}C values within a banded dolomite-sandstone sequence were sampled between lower and upper siliciclastic sequences. The upper Rainstorm Mb is almost entirely cut out by the basal Stirling unconformity, although the Johnnie oolite and ~10 m of overlying silt and calc-arenite are preserved and record the characteristically negative δ^{13}C values of the Shuram excursion (Figs. 2, 8).

Two Silurian Hills granite samples cross-cut ductile deformation in the eastern Silurian Hills were dated using U-Pb zircon geochronology at UCSB. Distinct youngest zircon populations – excluding inherited cores and failed analyses – yielded concordant magmatic ages for each sample. SLGC2008, sampled from the core of the high-grade southeastern Silurian Hills and originally mapped as basement, yielded a population of youngest grains with a middle-Cretaceous age of 101.42 ± 0.79 Ma with a MSWD of 0.45. SLGC2018, a syn-kinematic granitic dike within the Carrera – Riggs ductile detachment surface, yielded nearly a nearly identical middle-Cretaceous age of 101.94 ± 0.53 with a MSWD of 0.53 (Fig. 11).

Halloran & Silver Lake Hills

Reconnaissance mapping in the central and western Halloran Hills confirmed the mapping of DeWitt (1983), specifically the distribution of heavily metamorphosed and unidentifiable strata in the western hills. The Paleoproterozoic basement at Halloran is less exposed in the western Hills compared to the massive exposures in the south towards Baker and in the southeast at Halloran Pass. Limited exposures of unidentifiable Ediacaran sediments and heavily recrystallized carbonates akin to the Riggs carbonates in the Silurian Hills outcrop in the westernmost Halloran Hills and extend across highway 127 to the hill west of Silver Lake, where certain outcrops are less deformed. Faulted and relatively high-grade Johnnie Fm sediments there are exposed with a continuous section above, beginning with the unconformably overlying Stirling quartzite and continuing over 100 m into the Wood Canyon Fm (Fig. 5, 8). Beginning in cover, these ~50 m of exposed Johnnie Fm begin with ~10 m of siltstone and minor micrite before coarsening and grading into a typical middle Johnnie calc-arenite facies then overlain by ~12 m of heavily recrystallized dolomite with little diagnostic sedimentary structures finishing the section. Critically, δ^{13}C values of this Silver Lake dolomite are extremely negative and correlate with the extremely negative δ^{13}C values in the Rainstorm Mb (Fig. 2), confirming Stewart's (1970) upper Johnnie Rainstorm Mb interpretation. Sedimentary structures and bedding are not preserved in the recrystallized dolomite, although this sequence is very likely the uppermost middle Johnnie and Rainstorm Mb transition with a now unrecognizable ~10 m thick oolite. Similar to the Silurian Hills, the Rainstorm Mb is immediately cut out the by the basal Stirling unconformity above the oolite (Fig. 8).

Old Dad Mountain

The entire Pahrump Gp is absent at Old Dad Mountain and new mapping presented here differentiates the Ediacaran units that unconformably overlying gneissic basement in the northwest (Figs. 9, 10). These Ediacaran exposures are deposited atop gneissic basement and are bound on the east and west by km-scale Neogene – present mega-breccias and landslide deposits associated with the southern Death Valley shear zone in western SEDV (Dunne, 1977). A system of west-dipping normal faults cut the basement and overlying stratigraphy in both the north and south, as well as a well-developed ~NW-SE striking foliation measured in all map units in the northwest. A relatively undeformed, ~WNW-striking quartz-rich granitic dike cuts the foliated basement and was sampled for U-Pb geochronology. Sample SLGC2019 yielded a latest-Cretaceous age of 73.38 ± 0.71 Ma, a minimum age constraint on the ~NW-SE trending foliation at Old Dad (Figs. 9 – 11).

The Middle Johnnie Fm overlies gneissic basement with no lower Johnnie grits. Instead, a ~5 m thick, oxidized paleo-regolith with ~10 m of pebble conglomerate grading into massive, mature sand sits between basement and an overlying massive ~10 m thick dolostone with relatively neutral $\delta^{13}C$ values. Mixed siliciclastic and carbonate facies continue through the middle Johnnie here for ~70 m before deposition of the Johnnie oolite at the base of the upper Rainstorm Mb, marked by distinctly negative $\delta^{13}C$ values. The Rainstorm facies then fine upwards with ~30 m of silt and fine sand before a brief, ~10 m thick interval of the common upper Rainstorm Mb calc-arenites, also recording very negative $\delta^{13}C$ values. Although the Rainstorm Mb silt interval separating the oolite and upper calc-arenites here is thicker than regional equivalents, the uppermost calc-arenites are cut out by the erosive basal Stirling unconformity that undulates along the contact with a relief of ~5-10 m in some places (Figs. 9, 10). The typical Stirling and Wood Canyon late-Ediacaran – early-Cambrian sequence continues above, although both map units are thinner than measured elsewhere (e.g., Stewart, 1970) and the overlying middle-Cambrian upper Wood Canyon, Zabriskie, and Carrara formations are both heavily intruded and cut out by Neogene strike-slip faulting in the northeast. A small sliver of the early-Paleozoic carbonates is exposed in west-central Old Dad, although they are largely covered by normal fault blocks of overlying Permian Bird Springs Fm and not tractable along strike (Fig. 9).

Dunne's (1977) Playground fault surface juxtaposes the Ediacaran – Cambrian Death Valley strata at Old Dad with the younger Paleozoic carbonates – the Good Springs, Sultan, Monte Cristo, and Bird Springs formations – and cuts out sections of the Ediacaran – early-Cambrian stratigraphy across the inferred fault; however, no ductile deformation is obvious along the surface, which does not support Dunne's (1977) thrust interpretation. The relationship between the overlying Paleozoic carbonates and underlying heavily foliated basement Ediacaran sequence is strikingly similar to that observed at the Silurian Hills and reported in Shadow Valley (Friedmann et al., 1995). Some heavily brecciated zones are observed around the base of the carbonates, but they are not as extreme as those observed to the north. Nonetheless, ~10-100 m-scale isoclinal folding does record intense ductile deformation in the Paleozoic carbonate sequence here with chaotic folding and inconsistent fold axes similar to those found at the Silurian Hills and CMTC to the northeast.

Kelso & Providence Mountains

This study differentiates the basal Ediacaran Johnnie Fm unconformably overlying basement in the Kelso Mountains (Fig. 12). Basal Ediacaran exposures are mostly intruded or covered by large carbonate slide blocks, although a small panel of Middle Johnnie unconformably overlying basement with a clear overlying basal Stirling unconformity and transition to diagnostic quartz pebble conglomerate is exposed in the northeast. Sections measured at both the Kelso and Providence mountains are very similar in composition and thin slightly to the southeast. Middle Johnnie tan and brown banded dolostones with interbedded sandstone and calc-arenite conformably overly gneissic basement at both sections. A paleo-regolith similar to Old Dad was developed between gneissic basement and the lowermost Middle Johnnie. Both sections begin with ~3-5 m of pebble conglomerate and poorly sorted sand on basement. Above, the distinct Middle Johnnie Fm facies are identical across both sites and exhibit the same slightly positive $\delta^{13}C$ values with ~25 m of measured thinning within the interbedded dolomite, sandstone, and calc-arenite beds to the southeast, from Kelso to Providence. No transgressive upper Middle Johnnie facies are preserved at either location, nor any of the Rainstorm Mb. Only ~65 m (Kelso) and ~40 m (Providence) of section remains between basement and the basal Stirling unconformity, making it unclear how much Rainstorm Mb may have been deposited here.

4.2. Eastern SEDV transect

Winter's Pass Hills

The northern Winter's Pass Hills expose the full Ediacaran – Cambrian section around the perimeter of the massive uplifted basement block that defines the area (Fig. 15). No Kingston Peak diamictite is found in the Winter's Pass hills, although lower members of the Pahrump Gp, namely the Crystal Springs Fm, have now been identified and mapped in key localities. Areas of the Winter's Pass Hills not covered by Miocene slide blocks of Paleozoic carbonates are more commonly overlain by ridge-forming, often >100 m thick Sentinel Peak Mb reef facies cap carbonate. Some areas in the lower, southwestern Winter's Pass hills, however, expose small pockets of the Crystal Springs diabase and lower Crystal Springs grit, conglomerate, and quartzite facies, interpreted as olistostromes (Fig. 15). Importantly, there are no Pahrump Gp rocks exposed in the Winter's Pass hills, despite the abundance of basement, Crystal Springs Fm, and Beck Springs Fm olistostromes in the adjacent Cryogenian basin exposed immediately to the northwest in the southern Kingston Range.

New mapping around the basal Ediacaran contact in the eastern hills details a ~1-3 m thick, oxidized paleo-regolith developed during pre-Ediacaran basement exposure that underlies a ~30 m Sentinel Peak reef facies cap carbonate. Here, there is no Radcliffe Mb or coarse lower Johnnie Fm exposed and, instead, the uppermost Sentinel Peak grades directly into lower Middle Johnnie calc-arenites and quartzites, with some minor (~0.1-0.5 m) grit and sand lenses within the uppermost 3-5 m of the cap carbonate. These transgressive sands of the lower Middle Johnnie Fm become more carbonate-dominated and the motif of interbedded siliciclastic and carbonate facies continues throughout the Middle Johnnie for ~300 m with ~25 m of the upper Johnnie Rainstorm Mb exposed below the basal Stirling Fm unconformity (Figs. 15, 16). The Winter's Pass section measured in this study shows the same facies and sequence transitions as the section measured by Stewart (1970) in the northwestern Winter's Pass Hills where the thickness of all units expands to nearly double that of the Winter's Pass section (Fig. 16).

New U-Pb geochronology from locations in the uplifted Winter's Pass gneissic basement block confirm its Paleoproterozoic age, with dates ranging from ~1.8-1.9 Ga across distinctly different basement domains (Fig. 19). Both samples were taken from gneissic basement exposures directly adjacent to the pass proper, where the heaviest mylonitization is concentrated and the Winter's Pass block is directly adjacent to the autochthonous Cambrian stratigraphy of the structurally lower Mesquite Hills (Fig. 15). In CL imaging, each sample contains some grains that show core-rim relationships, displaying sharp boundaries between dark and light zircon (Fig. 19). Many grains extracted from the basement samples were metamict, or radiation-damaged, and deteriorated easily during mineral separation grain mounting. The combination of relatively small zircon grains across the populations, as well as fragmentation of weak grains limited options for placement of laser ablation spots on most grains. Consequently, the standard 25 μm wide ablation spot was reduced to 20 μm to match the size of the entire grain. No rims were >20 μm in thickness and could not be independently ablated at the 20 μm spot size without incorporating older core material. Consequently, the data define mixing lines between the Paleoproterozoic cores and Mesozoic rims. We interpret the upper intercept date for each sample to reflect the timing of Paleoproterozoic orthogneiss formation.

Mesquite Hills & Northwest Clark Mountain

The Mesquite Hills are structurally and stratigraphically distinct from the adjacent Winter’s Pass Hills with no gneissic basement exposures and more dramatic, map-scale isoclinal folding of the Ediacaran – Cambrian stratigraphy. In the northern Mesquite Hills, the Winter’s Pass thrust juxtaposes mylonitic basement gneiss against the folded Bonanza King Fm and underlying Cambrian units (Fig. 15). Older units are exposed towards the south, where the lowermost Ediacaran carbonate units appear to unconformably overlie diabase intrusions (Figs. 17, 18). Directly across the Kingston-Halloran detachment system to the southwest, Shadow Mountain is also made at least partially of undifferentiated Crystal Springs Fm siliciclastics, intruded by diabase. No Neoproterozoic units outcrop and the mountain itself is a large slide block entirely surrounded by landslide breccias and volcanics associated with the Miocene Shadow Valley supradetachment basin (Friedmann, 1997). Restoration of estimated westward dipping detachment across the Kingston-Halloran Valley places the Shadow Valley block against the Mesquite Hills (Davis & Friedmann, 2005) where some small diabase intrusions are mapped (Figs. 15, 17).

Section SLS2205 was measured in the southwestern Mesquite Hills where ~125 m of quartzite and grit are in contact with the Crystal Springs diabase and Noonday Fm Sentinel Peak Mb. The diabase contact is hidden under cover between subcrops; the Noonday contact is exposed and deformed as part of local isoclinal folding. Contrary to the positive δ^{13}C values in the Middle Johnnie carbonates, the Sentinel Peak here records negative δ^{13}C values and, in a separate panel, is mapped with the same Middle Johnnie mixed facies measured to the south in Clark Mountain (Fig. 17). While the exact structure of the isoclinal folding in the Sentinel Peak and Middle Johnnie members is not clear, a distinct Mesquite grit facies has been documented here (Fig. 15) that appears to be in sedimentary contact with the Noonday Fm. A detrital zircon population extracted from this unit (SLGC2201) yielded a detrital spectrum with two distinct peaks at ca. 1.4 and 1.7 Ga, respectively (Fig. 17).

New mapping in northwest Clark Mountain details a km-scale recumbent anticline cored by mylonitized gneissic basement and recognition of this broad fold constrains the location of the basal sedimentary unit(s) deposited on basement. Tighter 100 m-scale isoclinal folds continue in a train from the basement-cored anticline to the east, part of the greater zone of deformation at Pachalka characterized by overturned, and repeated late-Ediacaran – Cambrian strata (Fig. 17, 18). However, a small block faulted against the northern edge of the anticline does expose a small outcrop of Crystal Springs diabase unconformably overlain by a grit pebble conglomerate unit. This is the only exposure of the Mesquite grit in northwest Clark Mountain, the rest of which are found to the north in the southern Mesquite Hills. δ^{13}C values measured in the interbedded dolomite and calc-arenite beds in this short section are slightly negative and correlate with the upper Middle Johnnie carbonates measured in the western face of northwest Clark Mountain (Fig. 19). The lowermost Johnnie Fm here is an unconformable conglomerate deposited on basement, although the absence of the lower Middle Johnnie carbonates (neutral to positive δ^{13}C values) and preservation of underlying Crystal Springs Fm records an inferred paleo-topographic high adjacent to a thicker middle Johnnie section (Fig. 17).

Similar to the southern Mesquite Hills, a variably thick ~635 Ma Sentinel Peak Mb outcrops in northwest Clark Mountain, deposited directly on gneissic basement. In some places, the Sentinel Peak is ~25 m thick and built of m-scale stromatolitic dolomites with pronounced domal morphologies and well-preserved microbial laminations. Laterally on a ~100 m-scale, however, these paleo-reefs thin and disappear altogether (Fig. 18). Despite significant surrounding ductile deformation and previous structural interpretations for the missing stratigraphy (Burchfiel and Davis, 1971), a clear pattern of conglomerate infill can be mapped unconformably on basement in between the discrete Sentinel Peak patch reefs. This conglomerate quickly grades up into a coarse, clean quartzite for ~20 m before a steady transgressive sequence of interbedded silts, sands, dolomite, and dolo-arenite continues for >100 m to the basal Stirling unconformity. Similar to the Kelso and Providence mountains, there is no Rainstorm Mb here as that transgressive sequence has been entire cut out by the basal Stirling unconformity (Fig. 18).

A sample of the gneissic basement mapped below the Sentinel Peak patch reefs and Johnnie conglomerate was analyzed using U-Pb geochronology. Most grains extracted were heavily damaged and deteriorated easily during mineral separation and grain mounting. In CL imaging, grains showed obvious core-rim relationships similar to those from Winter's Pass. The combination of relatively small zircon across the population, as well as fragmentation of weak grains constrained options for placement of laser ablation spots on most grains, similar to the basement samples from the Winter's Pass Hills. Consequently, the typical 25 μm-wide ablation spot was reduced to 20 μm to either match the size of the entire grain. No imaged metamorphic rims were thick enough to be ablated at the 20 μm spot size without significant overlapping with the cores. ^{206}Pb/^{238}U and ^{207}Pb/^{235}U ratios plotted from analyses of 71 SLGC2112 grains yielded a discordant relationship with an upper intercept at ~1821 Ma (Fig. 19).

5. DISCUSSION

5.1. Western SEDV transect

The near-identical early-Ediacaran sections at the Silurian and Salt Spring hills record in-filling of a Cryogenian basin formed before ca. 635 Ma with a thick Radcliffe Mb developed there and documented nowhere else to the south (Fig. 13). The upper ~20 m Kingston Peak Fm facies at both sites grades from grit-to-pebble conglomerate turbidites directly into the Radcliffe Mb turbidites. The zone between the final Kingston Peak diamictite beds and the Radcliffe feldspathic grits contains a 10-20 cm thick micritic dolomite bed interpreted to be an extremely thin deep-water Noonday Sentinel Peak Mb that formed briefly between the earliest-Ediacaran debris flows during deglaciation. The Radcliffe Mb grits become less feldspathic up-section, eventually grading into a relatively more homogenous quartz-rich grit to coarse sand unit bedded in 1-3 m intervals, defined here as the local Lower Johnnie Fm, or Johnnie grits. Some minor calcareous cements and coarse calc-arenites are exposed within this transitional portion of the section; however, the facies are predominantly coarse, immature siliciclastics that infill the remaining accommodation space after rapid post-glacial Noonday deposition. This implies that these quartz rich grits and sands record the final stages of post-glacial transgression associated with the Radcliffe Mb.

In the Old Dad Mountains, the entire Pahrump Gp stratigraphy is absent with Ediacaran units deposited unconformably on basement. This unconformable relationship is critical to the definition of the Neoproterozoic rift boundary in the western transect and, combined with the well-preserved paleo-regolith and overlying transgressive sands (Fig. 10), indicates an exposed topographic high that was subaerially exposed during the earliest-Ediacaran, directly south of the Silurian-Salt Spring early-Ediacaran basin. The only indication of sedimentation influenced by tectonic processes in the SEDV western transect is at Silurian and Salt Springs where these earliest-Ediacaran units overlie the Cryogenian and older Pahrump Gp stratigraphy in a pre-635 Ma basin bound immediately to the south at the Halloran Hills (Figs. 5). At Salt Spring and Silurian, the feldspathic, arkosic Radcliffe grits and turbidites, along with overlying lower Johnnie grits and sands, appear to fill remaining space in the Tonian – Cryogenian basin, before onlapping of all overlying units beyond this boundary. The progressive onlapping and tapering of the Middle Johnnie Fm and younger strata to the southeast is subtle and, given the unconformities that bound each map unit, indicate repeated transgressions and erosion over a 10 myr-timescale from Old Dad Mountains to the southeast (Fig. 13).

5.2. Eastern SEDV transect

The tectonostratigraphic reconstruction of all sections measured in eastern SEDV (Figs. 1, 21) shows a clear absence of the Cryogenian and earliest-Ediacaran stratigraphy atop the rift boundary. Three new U-Pb ages on the Paleoproterozoic gneissic basement in the eastern transect of the SEDV confirm the presence of uplifted basement in easternmost SEDV in the Winter's Pass Hills and Clark Mountain (Fig. 19). The reduced data from LA-ICP-MS analyses of the basement zircon plot discordantly with clear Paleoproterozoic intercepts and no clear lower Mesozoic intercepts. CL images show core-rim relationships in some of the basement grains, although the rims are thin (<20 μm) and the majority of each grain is composed of the older core. While there is technically the possibility of these samples representing some Mesozoic intrusion that incorporated large Paleoproterozoic cores, this is a far less parsimonious interpretation given the clear sedimentary contacts between the Noonday and Johnnie formations atop gneissic basement, including distinct paleoregoliths that sit between these respective Ediacaran units and the basement at both Winter's Pass and NW Clark Mountain, identical to what is now documented at Old Dad Mountain (Figs. 13, 20).

The rift boundary transition in the eastern transect – between the Kingston Range and Winter's Pass Hills – exposes a much thicker Noonday Sentinel Peak Mb with ~10-100 m-scale reef facies cap carbonate deposited everywhere. While there is a well-developed Radcliffe Mb at Kingston (Summa, 1993; Stewart, 1971), it is more mature relative to the western sections (Fig. 13) and there are no overlying lower Johnnie grits. Instead, the Radcliffe Mb pinches out abruptly at Winter's Pass and the Noonday sequence is directly overlain by the mixed facies Middle Johnnie, as demonstrated by relatively neutral-to-slightly negative δ^{13}C values (Fig. 20). A clear boundary between the inferred Cryogenian basin and adjacent gneissic basement high delineates the rift boundary here, just as in the western transect across the Kingston-Halloran detachment system. A progressive onlapping of the middle-Johnnie and younger stratigraphy to the southeast reflects the same onlapping pattern as seen in the west. Importantly, these progressive onlapping relationships are also bound by significant unconformities, indicative of repeated transgressive and erosive events on a 10 myr-timescale, extending to the Ivanpah Mtns. where the first cratonal Tapeats-equivalent stratigraphy is preserved (Figs. 1, 13, 20, 24).

5.3. Implications for timing of SEDV 'rift-to-drift' transition

These onlapping Ediacaran transgressive sequences are interpreted to be driven by sea level rise, fall, and subsequent erosion. Subsidence plots generated in *Backstrip* for the western transect do not exhibit any sign of an Ediacaran exponential thermal decay curve that would be expected for onlapping in a newly rifted-passive margin tectonic setting. Instead, the ~100 m-scale stratigraphic thicknesses measured in the Ediacaran units record remarkably little sedimentation for a duration of >100 Myr (Figs. 13, 20). While some pre-existing Ediacaran stratigraphy has clearly been eroded during the incision of each unconformable overlying unit – primarily along the basal Middle Johnnie, Stirling and Wood Canyon formation basal contacts – there is still very little evidence for substantial sedimentation for the early to middle Ediacaran. As depicted in tectonic subsidence plots (Figs. 14, 21), each Ediacaran transgressive sequence is represented by a relatively minor linear phase of subsidence, separated by stepwise episodes of apparent non-subsidence. While this lack of subsidence in this interval may be a byproduct of significant erosion between transgressive intervals, there is no evidence for the kind of rapid subsidence predicted within a thermally subsiding passive margin throughout deposition of each unit.

Witkosky & Wernicke (2018) acknowledge some limitations of their extrapolation-based model, which assumes continuous subsidence and sedimentation from ca. 635 Ma until the Cambrian. The model is limited to a type-section in the Spring Mountains, which is stated to represent the entire regional Ediacaran stratigraphy as far south as the Nopah Range, but does not extend beyond the Cryogenian basin and onto the craton proper. This limitation to the model is critical because the authors factor in the compaction of underlying Pahrump sediments as a component of Ediacaran subsidence, in order to avoid a predicted overestimate of tectonic subsidence. Since their model does not take into account other well-documented Johnnie outcrops progressively and unconformably deposited on basement to the southeast in SEDV, a variable "lithostratigraphic substrate" is not factored into this suggested type-subsidence for the Johnnie Fm. Consequently, this thermal subsidence extrapolation over-estimates subsidence in space and time across the SEDV hinge zone.

A simpler explanation born out of the data presented here is that full rifting occurred in the Tonian – Cryogenian and progressive onlapping occurred throughout the Ediacaran with any coeval subsidence occurring farther to the northwest where irregular blocks of the North American craton and adjacent sub-basins were rifted away from the rift boundary, such as in the Panamint Range (Nelson et al., 2020). During the Cryogenian Snowball Earth events, repeated sea level fall and isostatic loading of the crust due to glaciation would have limited sedimentation in the basin adjacent to the new North American margin in SEDV. Additionally, sediment starvation along the newly formed and ice-covered SEDV rift would have resulted in rapid post-635 Ma deposition, following glacial erosion. With the additional driver of coeval isostatic rebound, existing topography would have been enhanced and the remnant Tonian – Cryogenian basin would have been preferentially filled on a ~10 myr-timescale (Figs. 13, 20). In the subsidence model presented here, the Kingston Peak Fm is interpreted as Sturtian with a Marinoan erosive surface recording no clear tectonic subsidence born out of measured stratigraphy (Figs. 14, 21). Evidence for this absence of Marinoan sedimentation is recorded in the rapid and concentrated earliest-Ediacaran sedimentation at the Salt Spring and Silurian Hills where a >150 m and >300 m thick Noonday Fm overlies Kingston Peak diamictite with a feldspathic, immature, and turbidite-dominated facies. Furthermore, the overlying lower Johnnie grit beds record the completion of sedimentation in this confined Tonian – Cryogenian basin and, similar to the local Noonday facies, are not found elsewhere in the early-Ediacaran SEDV strata (Figs. 13, 20).

Following local concentration of this early-Ediacaran sedimentation, a sequence of three major transgressive-erosive cycles is documented through middle-Ediacaran – middle-Cambrian in the basal Stirling, Wood Canyon, and Zabriskie formations, respectively (Figs.

13, 20, 23). From the Noonday – Johnnie grit section at the Silurian Hills, the Middle and Upper (Rainstorm Mb) progressively onlaps towards the southeast for a distance of ~50 km in the present (with basin-and-range extension). The overlying early-Cambrian units extend farther, up to ~30 km farther southeast, before the Zabriskie quartzite-equivalent Tapeats sandstone, documented across the North American Southwest, caps the sequence. It was not until the late-Cambrian Carrara and Bonanza King Formations that non-siliciclastic facies first blanketed the American Southwest and the first clear evidence for thermal subsidence (Levy and Christie-Blick, 1991) and, importantly, the absence of major exposure surfaces becomes apparent in measured sections (Figs. 13, 20) and subsidence calculations (Figs. 14, 21).

5.4. Implications for the inversion of Neoproterozoic stratigraphy within the CMTC

With reconstruction of the SEDV rift boundary across the west-dipping Miocene Kingston-Halloran detachment system (Fig. 22), new and existing geochronology can be used to refine the age model for the inversion of the hinge zone within the CMTC. Two ~101 Ma granites at the Silurian Hills – roughly coeval with the Delfonte volcanics in the Ivanpah Mountains (Walker et al., 1995) – provide a minimum age constraint on the ductile deformation of the Ediacaran stratigraphy there and prohibit placement of the Silurian Hills on the late-Cretaceous Keystone plate (Fig. 11). Earliest-Cretaceous ductile deformation at the Pachalka thrust in central Clark Mountains, east of the inferred Cryogenian basin, constrains deformation within the CMTC where Ediacaran units sit unconformably on basement. Consequently, shortening of the inferred Ediacaran hinge zone – both within and to the southeast of the Tonian – Cryogenian basin – must have been coeval during the early-Cretaceous. These new constraints on the timing and spatial distribution of hinge zone inversion provide a simpler model for the CMTC. Previous workers were right to distinguish between Winter's Pass, Mesquite, and Pachalka thrusts based on their differing stratigraphy (Burchfiel & Davis, 1971; Walker et al., 1995), but these new data indicate a much simpler model where Early-Cretaceous shortening in the Cordilleran hinterland was localized along the rift boundary in a much narrower segment of the crust than implied by the original miogeocline model (Fig. 23). Importantly, this constraint demonstrates the para-autochthonous nature of the rift-shoulder stratigraphy described herein and eliminates the need to explain the variability in the Neoproterozoic facies with an allochthonous thrust sheet derived farther off board to the northwest with a much greater displacement. Consequently, the throw on the inferred early-Cretaceous Winter's Pass-Mesquite thrust system along the rift boundary is significantly less than previously thought in the decollement-style allochthon model, although the exact displacement is still obscured by the extensive Miocene extension in the corridor (Fig. 23).

6. CONCLUSION

6.1. Reconstruction of the SEDV Neoproterozoic geology

Low-angle, westward dipping normal faulting has separated the inferred rift boundary into two segments on either side of the Kingston-Halloran detachment system during the Miocene. Restoration of this distended crust places the Silurian Hills ~SSW of the Winter's Pass Hills and southern Kingston Range (Fig. 22). The ~WNW facing Neoproterozoic strata implied by this restoration broadly agrees with the consensus ~NW facing direction for this time period and is corroborated through the Ediacaran with the progressive tapering of the entire Ediacaran – early-Cambrian sequence to the ~SE documented in this study (Figs. 13, 20) and others (e.g., Fedo and Cooper, 2001).

Some of the heaviest ductile deformation in SEDV is exposed along the inferred Tonian – Neoproterozoic boundary fault(s) where both the Silurian Hills and Winter's Pass Hills exposed isoclinally folded and mylonitized strata from the Mesoproterozoic Crystal Springs Formation – Cambrian sequence. This concentration of deformation along the rift boundary indicates that shortening within the CMTC was concentrated around the areas of Tonian-Cryogenian basin formation (Fig. 23). The Ediacaran tectonostratigraphic reconstruction presented here strongly suggest a much more localized zone of Mesozoic shortening directly against and above the Paleoproterozoic Ivanpah basement in the eastern SEDV corridor. Even without reconstruction of the Miocene Kingston-Halloran detachment system and Death Valley shear zone (Fig. 22), the total displacement within the greater CMTC – from the Silurian Hills to northwest Clark Mountain – cannot be as great as previously estimated in a decollement-style inversion of a regional miogeocline. In their original decollement model for the CMTC, Burchfiel & Davis (1971) estimated a total throw of 65-80 km between the

Keystone, Mesquite, and Winter's Pass thrusts. The new para-autochthon inversion model presented here both refines the basin framework and consequently constrains the total throw within the CMTC, particularly the Mesquite and Winter's Pass thrust, to a much shorter distance. Discounting for the Mesoproterozoic Crystal Springs Fm which is not included here in subsidence calculations for the Tonian – Cryogenian basin formation event, the entire Neoproterozoic – Middle Cambrian sequence is measured to be 3.50 km at the Silurian Hills and 4.182 km at the Kingston Range (Table 4). Assuming a simple ~60 ° ~NW dipping brittle fault plane representative of the Tonian – Cryogenian rift boundary in SEDV, the throw of the inverted para-autochthon would have been ~2.02 km at the Silurian Hills and ~2.41 km at the Kingston Range. This estimated distance excludes thicknesses from the Paleozoic carbonates deposited after the Carrara and Bonanza King formations in the Cambrian (Fig. 2), given the extent of deposition at this time far beyond the SEDV Neoproterozoic para-autochthonous zone (Figs. 1, 23).

6.2. Tonian – Cryogenian rifting

The parautochthonous zone, defined by the SEDV Tonian – Cryogenian rift-boundary stratigraphy (Fig. 23), is inverted within the middle structural plate of the CMTC, or the Mesquite thrust (e.g., Burchfiel & Davis, 1971). Onlapping of thick reef-facies Noonday and a transgressive Middle Johnnie Fm onto basement between NW Clark Mountain and the Silurian Hills, bounds the parautochthon to the southeast (Figs. 13, 20). Unconformable onlapping of a similar reef facies Noonday Fm and overlying Middle Johnnie Fm on both basement and the Mesoproterozoic Crystal Springs Fm at the Saddle Peak Hills, adjacent to the full Pahrump Gp exposures at the Salt Spring and Silurian, defines the northwestern parautochthon boundary (Fig. 1).

The parautochthonous stratigraphy is defined primarily by three distinct differences from the surrounding geology: (1) the presence of the Tonian Beck Springs dolomite-equivalent Silurian Hills sandstone at the Salt Spring and Silurian Hills (e.g., Smith et al., 2016); (2) both a thin or absent earliest-Ediacaran Sentinel Peak cap carbonate and an immature, particularly thick Radcliffe Mb; (3) and the similarly immature and thick (~100 m) Lower Johnnie grits. Together, these regionally distinct facies spanning the Tonian – early-Ediacaran record the filling of a localized, trough-like basin; however, evidence for active basin formation and subsidence through this entire time is missing and better explained by glacial erosion and isostasy driven topography. Clear rift-related sedimentation persisted well into the Cryogenian and is documented at both the Silurian Hills and Kingston Range; however, the varied, transgressive facies of the Noonday Fm extend much farther south. While the Noonday Fm and lowermost Johnnie grits do fill the remaining accommodation space in the SEDV Tonian – Cryogenian basin, these units exhibiting different facies are documented well beyond this basin (i.e., Noonday reef facies in the Mesquite Hills and at Clark Mountain). Therefore, there is no direct evidence for continued crustal extension and rift-related faulting into the Ediacaran. Instead, it appears that post-glacial Noonday deposition at ca. 635 Ma was simply enhanced along the inferred rift boundary as renewed post-glacial sedimentation caught up with filling the starved basin created during Tonian – Cryogenian rift-related faulting (Figs. 13, 20). Furthermore, extension of the Ediacaran facies well beyond the basin to the southeast and bracketed by major erosive unconformities at every stratigraphic boundary do not require tectonic subsidence to accommodate the thicknesses measured and reported across SEDV.

Instead, field relationships, temporal correlations, and subsidence constraints across the study area indicate repeated transgressive-erosive events lasting from at least ~635 Ma – Middle-Cambrian time with no clear evidence for active subsidence, either tectonic or passive (thermal) for this duration. The absence of any clear signal of an exponential, thermal subsidence in Ediacaran SEDV may be due to the presence of additional Neoproterozoic basement highs to the northwest in the Panamint Range (Nelson et al., 2020), although the concentration of subsidence there to the northwest of SEDV is speculative and there may simply be no regional thermal subsidence until the late-Cambrian during Carrara and Bonanza King deposition (e.g., Levy and Christie-Blick, 1991) (Figs. 14, 21).

6.3. Early-Ediacaran – Middle-Cambrian transgressive sequences

Previous attempts at subsidence models for the Mojave region and greater Southwest North America have been hindered by a combination of incomplete or mis-interpreted stratigraphy and inaccurate geochronology (e.g., Levy & Christie-Blick; Fedo & Cooper; Witkosky & Wernicke, 2018). New globally correlated Ediacaran geochronology and chemostratigraphy now provides a much tighter temporal framework for the Cryogenian – Cambrian (Nelson et al., 2020; Rooney et al., 2020; Yang et al., 2021) (Fig. 2), which provides the foundation for a more temporally-accurate regional subsidence model. Key field relationships between the Kingston Peak, Noonday, and Johnnie formations observed across SEDV clarify the broader context of various local sections used for existing subsidence models (Figs. 13, 14, 20, 21). New tectonostratigraphic correlations across SEDV presented here show no evidence for continued Ediacaran rifting (Armin and Mayer, 1983; Summa, 1993; Fedo and Cooper, 2001) and support the model of full rifting and continental separation before the end of the Cryogenian. This interpretation agrees with Witkosky and Wernicke (2018) insofar as rift-related subsidence had ceased by ca. 635 Ma, although it does not agree with the immediate transition to a thermally subsiding tectonic environment immediately after deglaciation at this time. Rather, mapped Ediacaran unconformable relationships and subsidence calculations from measurements indicate repeated transgressive-erosive cycles atop the SEDV Pahrump Gp stratigraphy for >100 myr. Importantly, the tapering Johnnie Fm onlaps to the southeast on a ~10 myr-timescale with unconformable relationships above and below. These relationships indicate repeated transgressive-regressive sequences atop the craton which do not manifest in a clear subsidence signal (Figs. 14, 22), nor is much stratigraphic thickness developed for such a long duration of time, before deposition of the kms-thick Paleozoic carbonate supersequence (e.g., Levy and Christie-Blick, 1991).

7. References

Affinati, S.C., Hoisch, T.D., Wells, M.L., and Vervoort, J.D., 2020, Pressure-temperature-time paths from the Funeral Mountains, California, reveal Jurassic retroarc underthrusting during early Sevier orogenesis: GSA Bulletin, v. 132, p. 1047–1065.

Armin, R.A., and Mayer, L., 1983, Subsidence analysis of the Cordilleran miogeocline: implications for timing of late Proterozoic rifting and amount of extension (USA): Geology, v. 11, p. 702–705.

Bergmann, K.D., Zentmyer, R.A., and Fischer, W.W., 2011, The stratigraphic expression of a large negative carbon isotope excursion from the ediacaran Johnnie Formation, Death Valley: Precambrian Research, v. 188, p. 45–56.

Burchfiel, B.C. and Davis, G. A., 1971, Clark Mountain Thrust Complex in the Cordillera of Southeastern California: Geologic Summary and Field Trip Guide.

Burchfield, B.C., and Davis, G.A., 1975, Nature and controls of Cordilleran orogenesis, western United States: Extension of an earlier synthesis: American Journal of Science, v. 275-A, p. 363–396.

Busby, C.J., Schermer, E.R., and Mattinson, J.M., 2002, Extensional arc setting and ages of Middle Jurassic eolianites, Cowhole Mountains (eastern Mojave Desert block, California): Geological Evolution of the Mojave Desert and Southwestern Basin and Range, Geological Society of America, Memoir 195.

Clapham, M. E. and Corsetti, F. A., 2005, Deep valley incision in the terminal Neoproterozoic (Ediacaran) Johnnie Formation, eastern California, USA: Tectonically or glacially driven?: Precambrian Research, v. 141, 3-4, p. 154-164.

Colpron, M., Logan, J.M., and Mortensen, J.K., 2002, U-Pb zircon age constraint for late Neoproterozoic rifting and initiation of the lower Paleozoic passive margin of western Laurentia: Canadian Journal of Earth Sciences, v. 39, p. 133–143.

Comstock, J.E., 1997, Vertical Axis Rotation in the Silurian Hills: A Cenozoic Overprint on the Mesozoic U.S. Cordilleran Magmatic Arc, Master’s thesis: University of New Orleans.

Davis, G.A., and Friedmann, S.J., 2005, Large-scale gravity sliding in the Miocene Shadow Valley supradetachment basin, Eastern Mojave Desert, California: Earth-Science Reviews, v. 73, p. 149–176.

Davis, G.A., 1993, Pluton pinning of an active Miocene detachment fault system, eastern Mojave Desert, California: Geology, v. 21, p. 627–630.

DeCelles, P.G., 2004, Late Jurassic to Eocene evolution of the Cordilleran thrust belt and foreland basin system, western U.S.A: American Journal of Science, v. 304, p. 105–168.

Dehler, C., Gehrels, G., Porter, S., Heizler, M., Karlstrom, K., Cox, G., Crossey, L., and Timmons, M., 2017, Synthesis of the 780-740 Ma Chuar, Uinta Mountain, and Pahrump (ChUMP) groups, western USA: Implications for Laurentia-wide cratonic marine basins: Bulletin of the Geological Society of America, v. 129, p. 607–624.

Dewitt, E., Armstrong, R.L., Sutter, J.F., and Zartman, R.E., 1984, U-Th-Pb, Rb-Sr, and Ar-Ar mineral and whole-rock isotopic systematics in a metamorphosed granitic terrane, southeastern California: Geological Society of America Bulletin, v. 95, p. 723–739.

Dunne, G.C., 1977, Geology and structural evolution of Old Dad Mountain, Mojave Desert, California: Bulletin of the Geological Society of America, v. 88, p. 737–748.

Dunne, G.C., and Walker, J.D., 2004, Structure and evolution of the East Sierran thrust system, east central California: Tectonics, v. 23.

Eisbacher, G. H., 1983, Book Reviews: Geology, 11 (6), p. 367.

Eyster, A., Weiss, B. P., Karlstrom, K. E., and Macdonald, F. A., 2020, Paleomagnetism of the Chuar Group and evaluation of the late Tonian Laurentian apparent polar wander path with implications for the makeup and breakup of Rodinia: Geological Society of America Bulletin 132 (3-4), 710-738.

Fedo, C.M., and Cooper, J.D., 2001, Sedimentology and sequence stratigraphy of Neoproterozoic and Cambrian units across a craton-margin hinge zone, southeastern California, and implications for the early evolution of the Cordilleran margin: Sedimentary Geology, v. 141–142, p. 501–522.

Friedmann, S.J., 1997, Rock-avalanche elements of the Shadow Valley basin, eastern Mojave Desert, California: Processes and problems: Journal of Sedimentary Research, v. 67, p. 792–804.

Giallorenzo, M.A., Wells, M.L., Yonkee, W.A., Stockli, D.F., and Wernicke, B.P., 2018, Timing of exhumation, Wheeler Pass thrust sheet, southern Nevada and California: Late Jurassic to middle Cretaceous evolution of the southern Sevier fold-and-thrust belt: Bulletin of the Geological Society of America, v. 130, p. 558–579.

Harlan, S.S., Heaman, L., LeCheminant, A.N., and Premo, W.R., 2003, Gunbarrel mafic magmatic event: A key 780 Ma time marker for Rodinia plate reconstructions: Geology, v. 31, p. 1053–1056.

Heaman, L.M. and Grotzinger, J. P, 1992, 1.08 Ga diabase sills in the Pahrump Group, California; implications for development of the Cordilleran Miogeocline: Geology, 20, 637–640.

Hodges, K. V., McKenna, L.W., Stock, J., Knapp, J., Page, L., Sternlof, K., Silverberg, D., Wüst, G., and Walker, J.D., 1989, Evolution of extensional basins and basin and range topography west of Death Valley, California: Tectonics, v. 8, p. 453–467.

Hoffman, P.F., 1991, Did the breakout of Laurentia turn Gondwanaland inside-out?:Science, v. 252, p. 1409–1412.

Hoffman, P. F., 2017, Sedimentary depocenters on Snowball Earth: Case studies from the Sturtian Chuos Formation in northern Namibia, 2017: Geosphere, 13 (3), 811-837.

Hoffman, P. F., 2022, Global erosion on Snowball Earth: testing for bias in flux balance, geographic setting, and tectonic regime: Canadian Journal of Sciences, Just In, 06.

Hoisch, T.D., Wells, M.L., Beyene, M.A., Styger, S., and Vervoort, J.D., 2014, Jurassic Barrovian metamorphism in a western U.S. Cordilleran metamorphic core complex, Funeral Mountains, California: Geology, v. 42, p. 399–402, doi:10.1130/G35352.1.

Ingersoll, R.V., and Schweickert, R.A., 1986, A plate-tectonic model for Late Jurassic ophiolite genesis, Nevadan orogeny and forearc initiation, Northern California: Tectonics, v. 5, p. 901–912.

Isakson, V.H., Schmidtz, M. D., Dehler, C. M., Macdonald, F. A., and Yonkee, W. A., 2022, A robust age model for the Cryogenian Pocatello Formation of southeastern Idaho (northwestern USA) from tandem in situe and isotope dilution U-Pb dating of volcanic tuffs and epiclastic detrital zircons: Geosphere, 18 (2): 825-849.

Kupfer, D.H., 1960, Faulting and Chaos, Silurian Hills: Bulletin of the Geological Society of America, v. 71, p. 181–214.

Kylander-Clark, A.R.C., Hacker, B.R., and Cottle, J.M., 2013, Laser-ablation split-stream ICP petrochronology: Chemical Geology, v. 345, p. 99–112.

Levy, M., and Christie-Blick, N., 1991, Tectonic subsidence of the early Paleozoic passive continental margin in eastern California and southern Nevada: Geological Society of America Bulletin, v. 103, p. 1590–1606.

Lund, K., 2008, Geometry of the Neoproterozoic and Paleozoic rift margin of western Laurentia: Implications for mineral deposit settings: Geosphere, 4 (2), 429-444.

Macdonald, F.A., Prave, A.R., Petterson, R., Smith, E.F., Pruss, S.B., Oates, K., Waechter, F., Trotzuk, D., and Fallick, A.E., 2013, The Laurentian record of Neoproterozoic glaciation, tectonism, and eukaryotic evolution in Death Valley, California: Bulletin of the Geological Society of America, v. 125, p. 1203–1223.

Mahon, R.C., Dehler, C.M., Link, P.K., Karlstrom, K.E., and Gehrels, G.E., 2014a, Geochronologic and stratigraphic constraints on the Mesoproterozoic and

NeoProterozoic Pahrump Group, Death Valley, California: A record of the assembly, stability, and breakup of Rodinia: Geological Society of America Bulletin, v. 126, p. 652–664.

Maud, R. L., 1983, Stratigraphy, petrography and depositional environments of the carbonate-terrigenous member of the Crystal Spring Formation, Death Valley, California, Ph.D. dissertation: University Park, Pennsylvania, Pennsylvania State University.

Miller, J.M.G., 1985, Glacial and syntectonic sedimentation; the Upper Proterozoic Kingston Peak Formation, southern Panamint Range, eastern California: Geological Society of America Bulletin, v. 96, p. 1537–1553.

Mulder, J.A., Karlstrom, K.E., Fletcher, K., Heizler, M.T., Timmons, J.M., Crossey, L.J., Gehrels, G.E., and Pecha, M., 2017, The syn-orogenic sedimentary record of the Grenville Orogeny in southwest Laurentia: Precambrian Research, v. 294, p. 33–52.

Nelson, L.L., Ahm, A.S.C., Macdonald, F.A., Higgins, J.A., and Smith, E.F., 2021, Fingerprinting local controls on the Neoproterozoic carbon cycle with the isotopic record of Cryogenian carbonates in the Panamint Range, California: Earth and Planetary Science Letters, v. 566, p. 116956.

Nelson, L., Smith, E., Hodgin, E., Crowley, J., Schmitz, M., and Macdonald, F., 2020, Geochronological constraints on Neoproterozoic rifting and onset of the Marinoan glaciation from the Kingston Peak Formation in Death Valley, California (USA): Geology, v. 48, p. 1–5.

Partin, C. and Sadler, P., 2016, Slow net sediment accumulation sets snowball Earth apart from all younger glacial episodes: Geology, v. 44, p. 33-42.

Petterson, R., Prave, A.R., Wernicke, B.P., and Fallick, A.E., 2011, The Neoproterozoic Noonday Formation, Death Valley region, California: Geological Society of America Bulletin, v. 123, p. 1317–1336.

Prave, A.R., 1999, Two diamictites, two cap carbonates, two δ13C excursions, two rifts: The Neoproterozoic Kingston Peak Formation, Death Valley, California: Geology, v. 27, no. 4, p. 339-342.

Schweickert, R.A., Bogen, N.L., Girty, G.H., Hanson, R.E., and Merguerian, C., 1985, Timing and structural expression of the Nevadan orogeny, Sierra Nevada, California: Discussion: Bulletin of the Geological Society of America, v. 96, p. 1346–1347.

Smith, E.F., MacDonald, F.A., Crowley, J.L., Hodgin, E.B., and Schrag, D.P., 2016, Tectonostratigraphic evolution of the c. 780-730 Ma Beck Spring Dolomite: Basin formation in the core of Rodinia: Geological Society Special Publication, v. 424, p. 213–239.

Snow, J.K., 1992, Large-magnitude Permian shortening and continental-margin tectonics in the southern Cordillera: Geological Society of America Bulletin, v. 104, p. 80-105.

Snow, J.K., and Wernicke, B.P., 2000, Cenozoic tectonism in the central basin and range: Magnitude, rate, and distribution of upper crustal strain: American Journal of Science, v. 300, p. 659–719.

Spencer, J.E., 1990, Geologic map of southern Avawatz Mountains, Northeastern Mojave Desert Region, San Bernardino County, California, USGS.

Summa, K.L., 1993, Sedimentologic, Stratigraphic, and Tectonic Controls of a Mixed Carbonate-Siliciclastic Succession: Neoproterozoic Johnnie Formation, Southeast California: Massachusetts Institute of Technology Ph.D. Dissertation.

Stewart, J.H., 1970, Upper Precambrian and Lower Cambrian Strata in the Southern Great Basin, California and Nevada: US Geological Survey Professional Paper 620.

Stevens, C.H., Stone, P., Dunne, G.C., Greene, D.C., Walker, J.D., and Swanson, B.J., 1997, Paleozoic and Mesozoic evolution of east-central California: International Geology Review, v. 39, p. 788–829.

Tobisch, O.T., Paterson, S.R., Longiaru, S., and Bhattacharyya, T., 1987, Extent of the Nevadan orogeny, central Sierra Nevada, California (USA): Geology, v. 15, p. 132–135.

Wells, M.L., and Hoisch, T.D., 2008, The role of mantle delamination in widespread Late Cretaceous extension and magmatism in the Cordilleran orogen, western United States: Bulletin of the Geological Society of America, v. 120, p. 515–530.

Wernicke, B., Axen, G.J., and Snow, J.K., 1990, Basin and range extensional tectonics at the latitude of Las Vegas, Nevada: Special Paper of the Geological Society of America, v. 253, p. 243–262.

Wernicke, B., and Snow, J.K., 1998, Cenozoic tectonism in the central basin and range: Motion of the sierran-great valley block: International Geology Review, v. 40, p. 403–410.

Whitmeyer, S.J., and Karlstrom, K.E., 2007, Tectonic model for the Proterozoic growth of North America: Geosphere, v. 3, p. 220–259.

Witkosky, R., and Wernicke, B.P., 2018, Subsidence history of the Ediacaran Johnnie Formation and related strata of southwest Laurentia: Implications for the age and duration of the Shuram isotopic excursion and animal evolution: Geosphere, v. 14, p. 2245–2276.

Wooden, J.L., and Miller, D.M., 1990, Chronologic and isotopic framework for early Proterozoic crustal evolution in the eastern Mojave Desert region, SE California: Journal of Geophysical Research, v. 95, p. 20,133–20,146.

Wolf, M.B., and Saleeby, J.B., 1992, Jurassic Cordilleran dike swarm-shear zones: implications for the Nevadan orogeny and North American plate motion: Geology, v. 20, p. 745–748.

Yang, C., Rooney, A.D., Condon, D.J., Li, X.H., Grazhdankin, D. V., Bowyer, F.T., Hu, C., Macdonald, F.A., and Zhu, M., 2021, The tempo of Ediacaran evolution: Science Advances, v. 7, p. 1–11.

Yonkee, W.A., and Weil, A.B., 2015, Tectonic evolution of the Sevier and Laramide belts within the North American Cordillera orogenic system: Earth-Science Reviews, v. 150, p. 531–593.

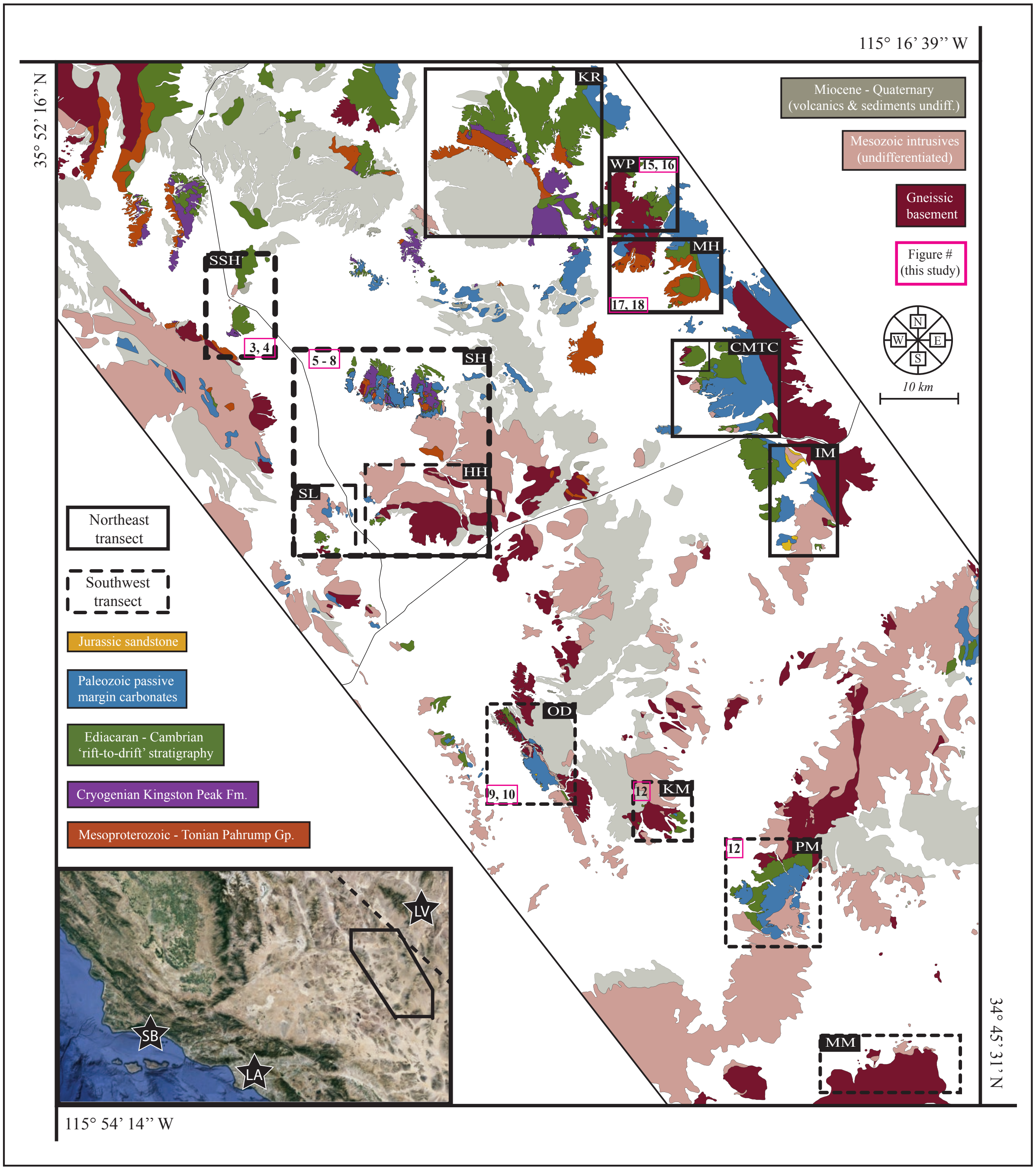

Figure 1. Tectonostratigraphic overview geologic map of Southeastern Death Valley (SEDV). Numbers in boxes correspond to thesis figure numbers. Dashed line is CA-NV state border. SSH: South Salt Spring Hills; SH: Silurian Hills; HH: Halloran Hills; SL: Silver Lake Hills; OD: Old Dad Mountain.; KM: Kelso Mountains; PM: Providence Mountains; MM: Marble Mountains; KR: Kingston Range; WP: Winter’s Pass Hills; MH: Mesquite Hills; CMTC: Clark Mountain & Clark Mountain thrust complex; IM: Ivanpah Mountains. QGIS polygons synthesized from this study and previous workers: Miller et al. (2003); Stone et al. (2017); Dunne (1983); Walker & Davis (1995); Davis & Friedmann (2005); DeWitt et al. (1984); Smith et al. (2016). Imagery modified from Google Earth.

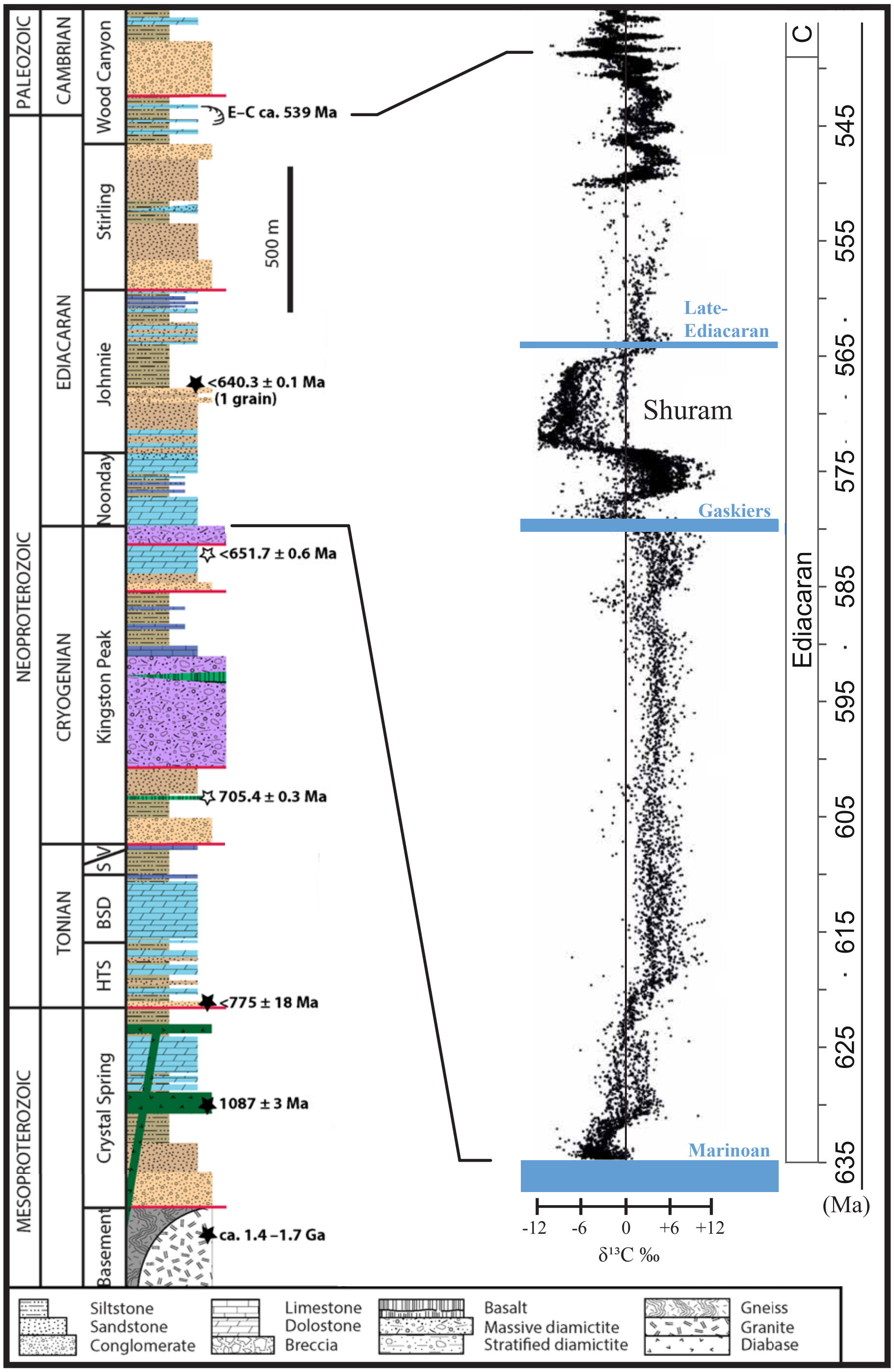

Figure 2. SEDV regional stratigraphy, U-Pb geochronologic constraints, and compilation of global δC^{13} data from Ediacaran sections. Stratigraphic section and geochronology modified from Nelson et al. (2020). Isotopic curve modified from Yang et al. (2021).

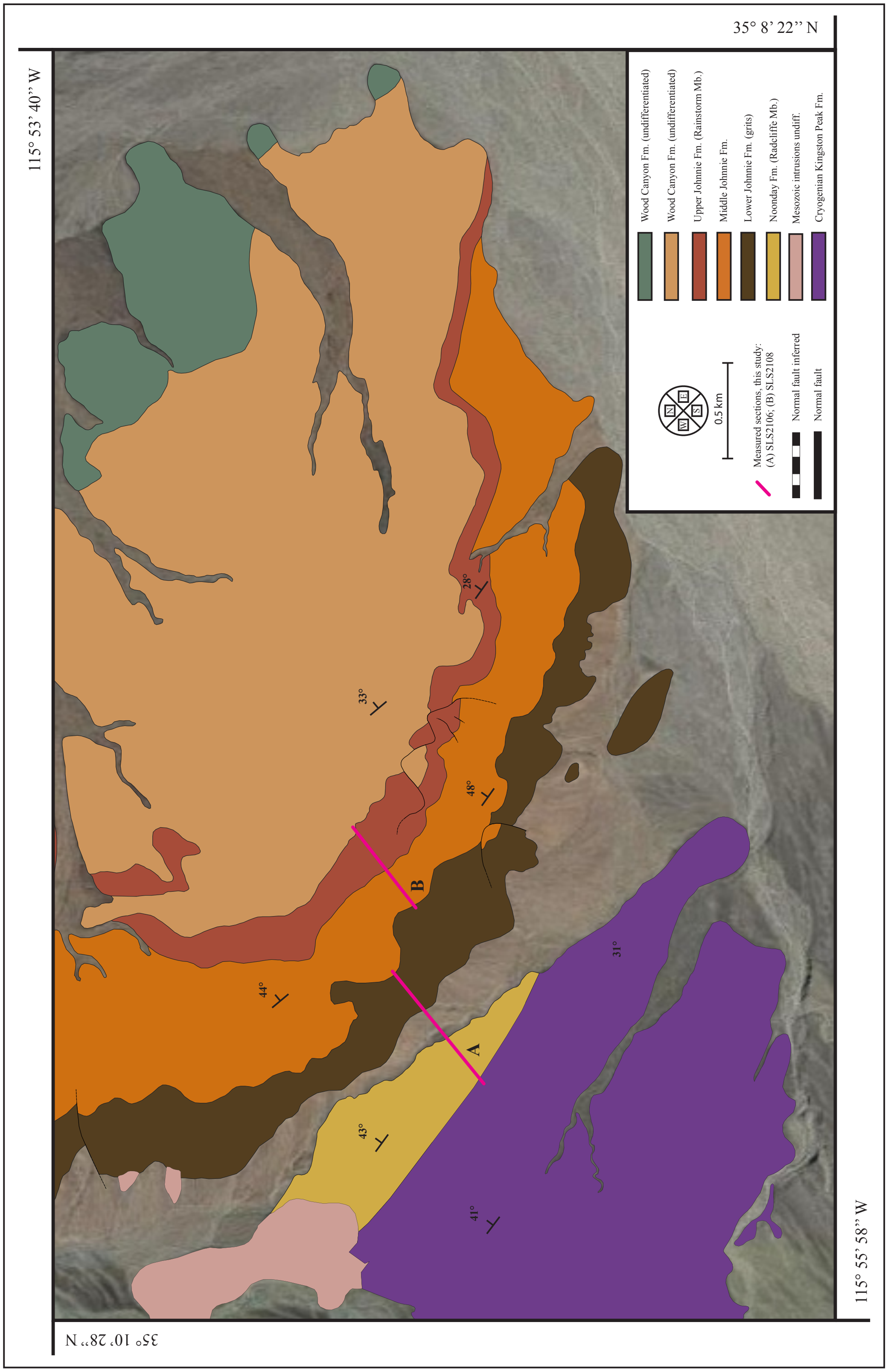

Figure 3. Geologic map of the Southern Salt Spring Hills. Mapping from this study and modified from Google Earth and QGIS.

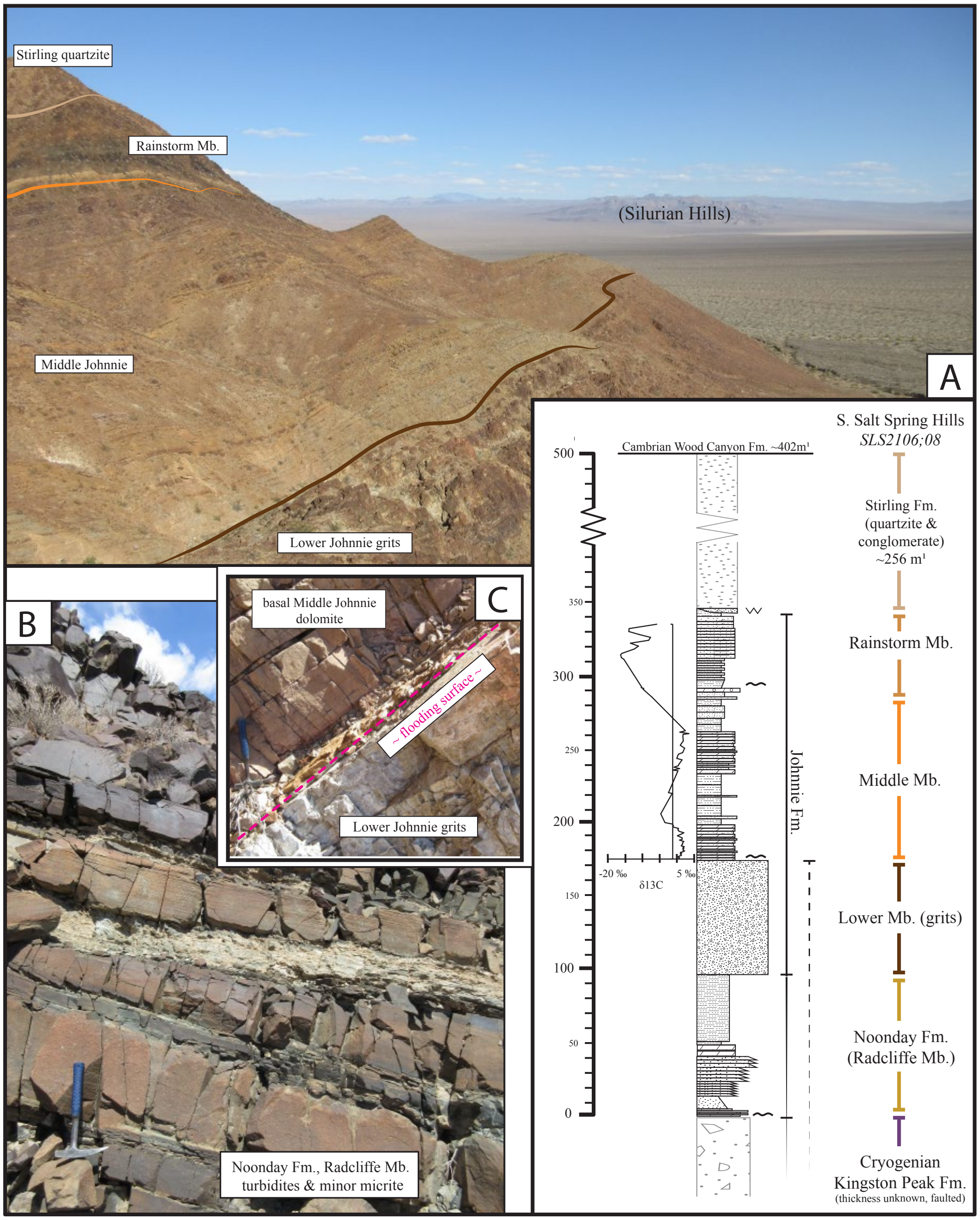

Figure 4. Measured Ediacaran stratigraphy at the South Salt Spring Hills. A: Overview of the measured middle and upper Johnnie Fm. Note the Johnnie oolite bed at the base of the Rainstorm Mb. B: Turbidites grading up from the uppermost Kingston Peak Fm. and into the feldspathic grits of the lower Noonday Fm. Radcliffe Mb. C: Sharp flooding surface at the contact between the upper Lower Johnnie grits and quartzite and lowermost Middle Johnnie dolostone beds. Photographs and δC^{13} analyses from this study.

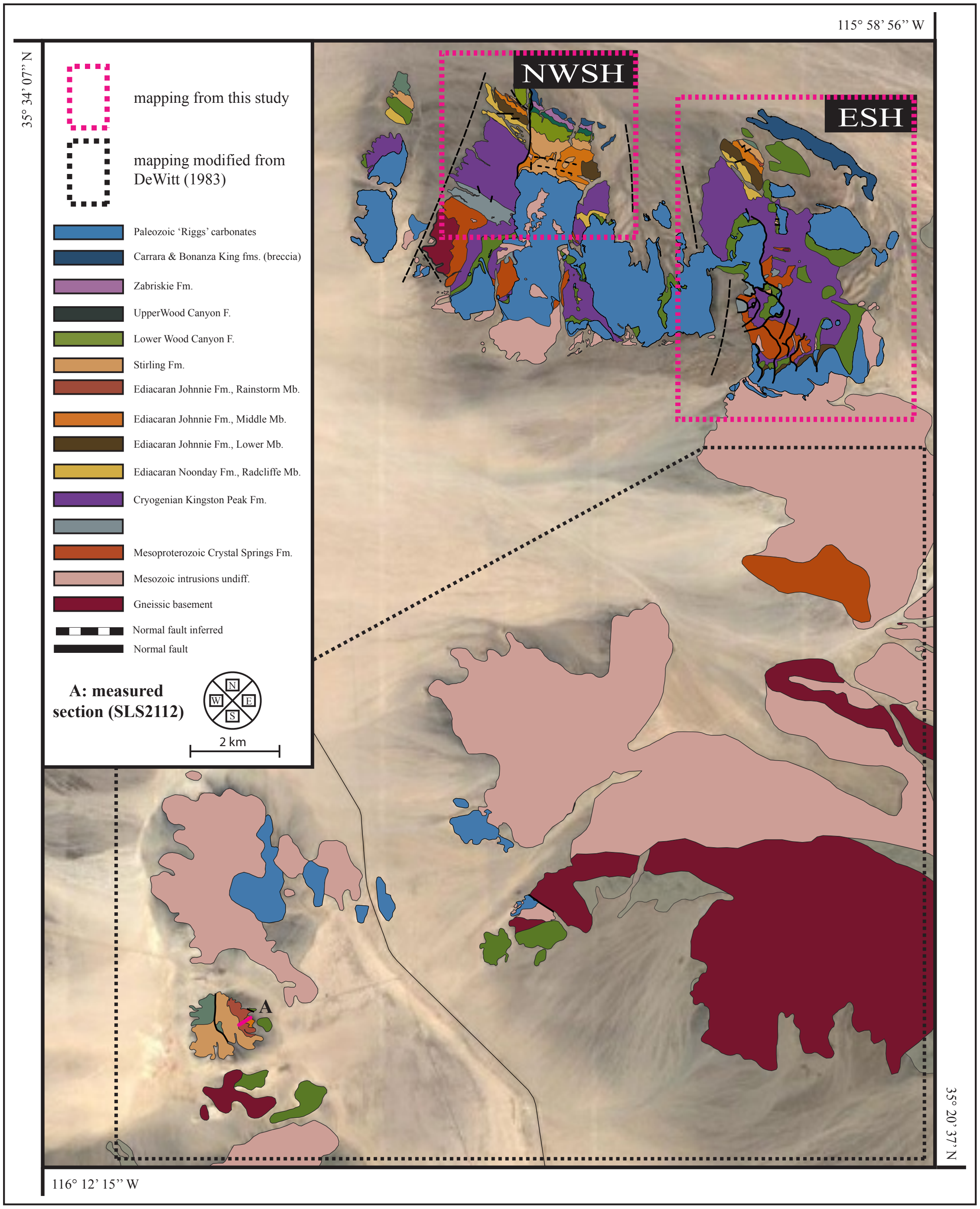

Figure 5. Overview geologic map of the Silurian, Halloran, and Silver Lake Hills. Section measured at Silver Lake shown in pink. Field sites mapped in the Silurian Hills are outlined (Figs. 6, 7). Mapping from this study and modified from Google Earth and QGIS.

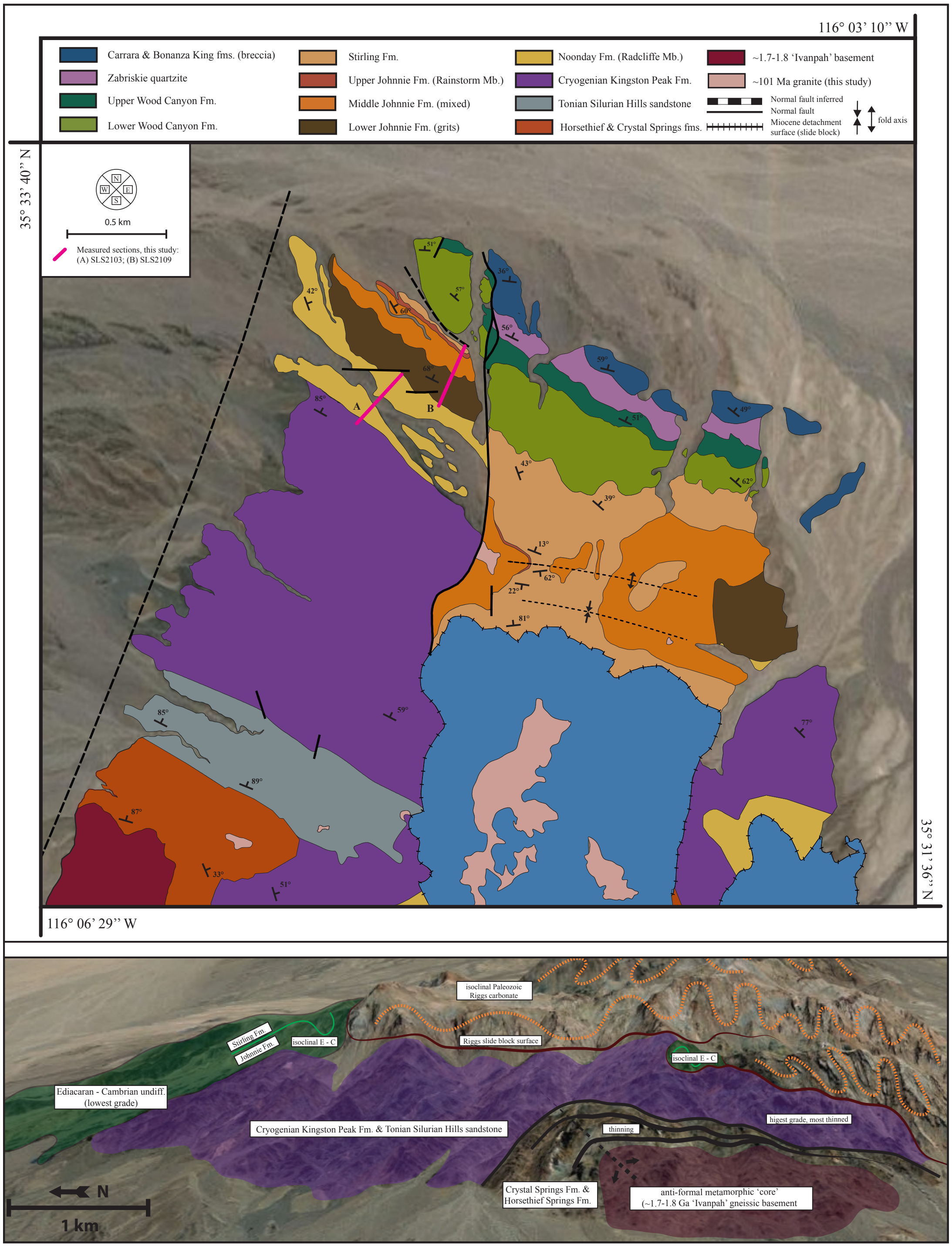

Figure 6. Geologic map of the northwestern Silurian Hills. Lower panel depicts an east-facing perspective of the basic structural relationships between the metamorphic and stratigraphic domains in the western Silurian Hills. High-grade metamorphism is concentrated in the south (right side of image) where the Crystal Springs and Horsethief Springs formations are most thinned. Undifferentiated Riggs carbonates are faulted against the Kingston Peak Fm. and portions of entire Ediacaran sequence around the Silurian Hills. Mapping from this study and modified from Google Earth and QGIS.

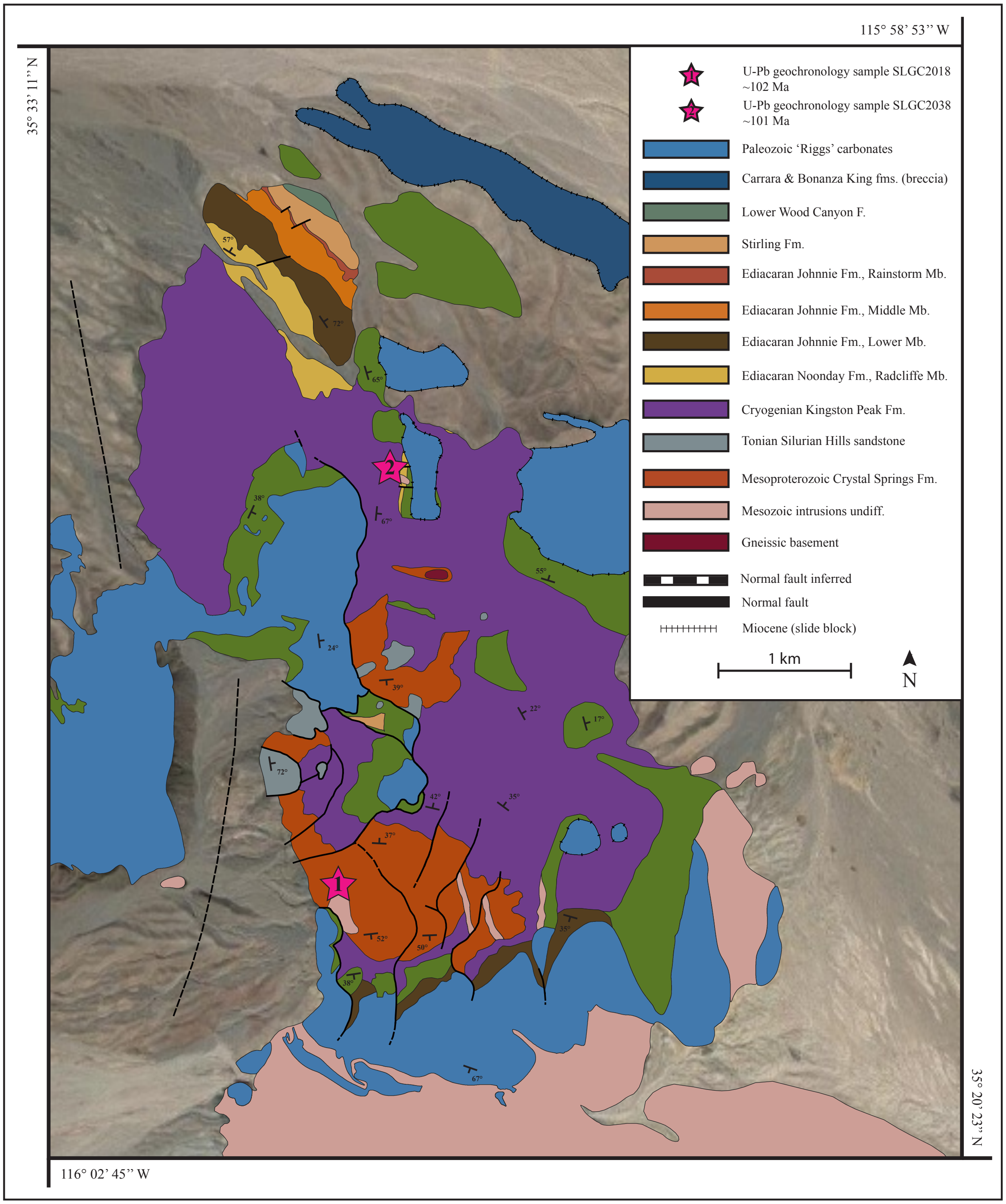

Figure 7. Geologic map of the eastern Silurian Hills. See Fig. 11 for U-Pb geochronology on sampled granites. See Comstock (1997) for detailed mapping of metamorphic domains. Mapping from this study and modified from Google Earth and QGIS.

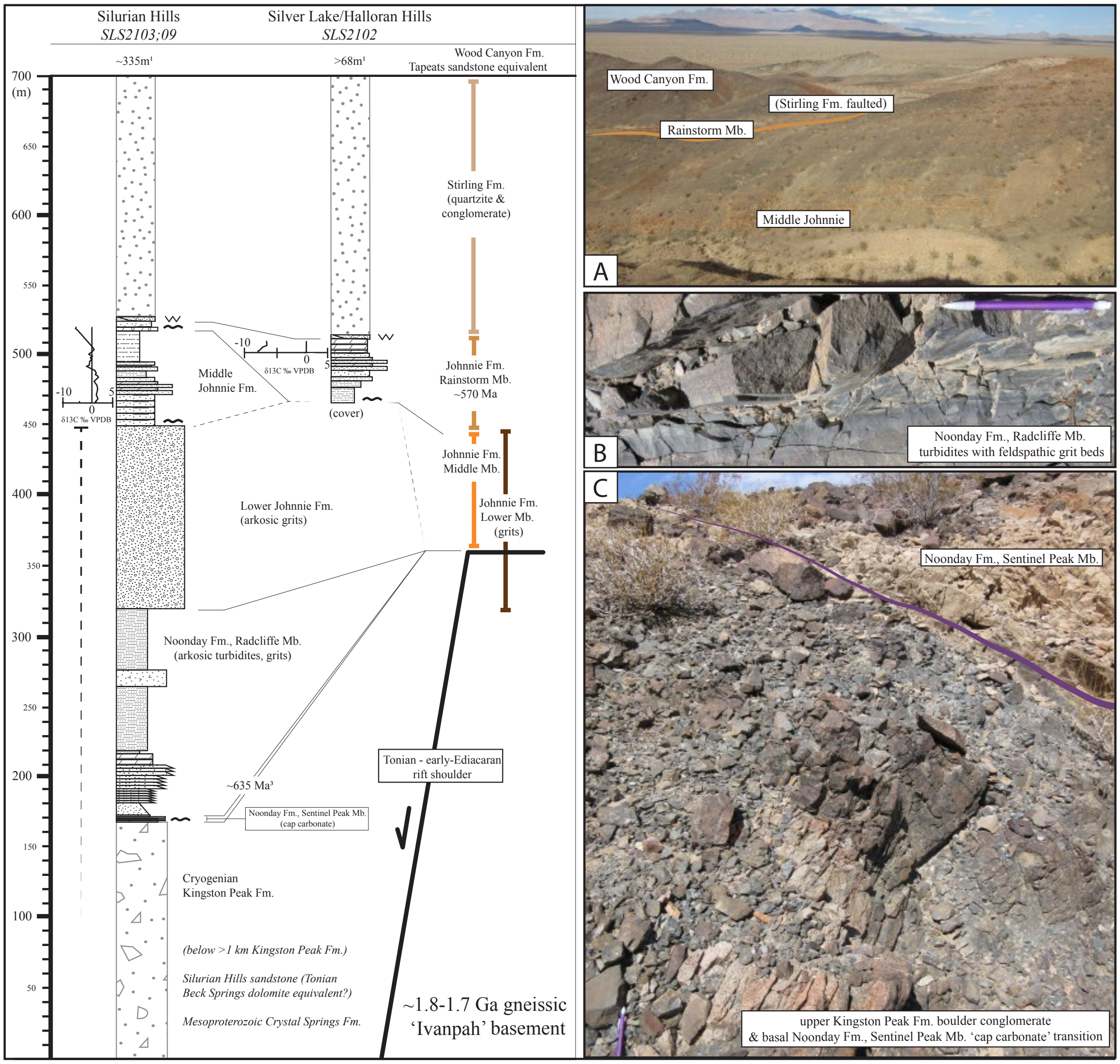

Figure 8. Measured Ediacaran stratigraphy at northwestern Silurian Hills and Silver Lake Hills. A: Measured members of the Johnnie Fm. The Stirling Fm unconformably overlies the Rainstorm Mb and is cut out up-section and faulted against the Wood Canyon Fm. B: A turbidite within the Noonday Fm. lower Radcliffe Mb. with <cm-scale feldspathic grits within each coarse bed. C: Uppermost Kingston Peak diamictite in the Northwest Silurian Hills; boulder conglomerate grades directly into feldspathic turbidites with irregular, <0.5m thick Noonday Fm Sentinel Peak Mb cap carbonate. Photographs and δC^{13} analyses from this study.

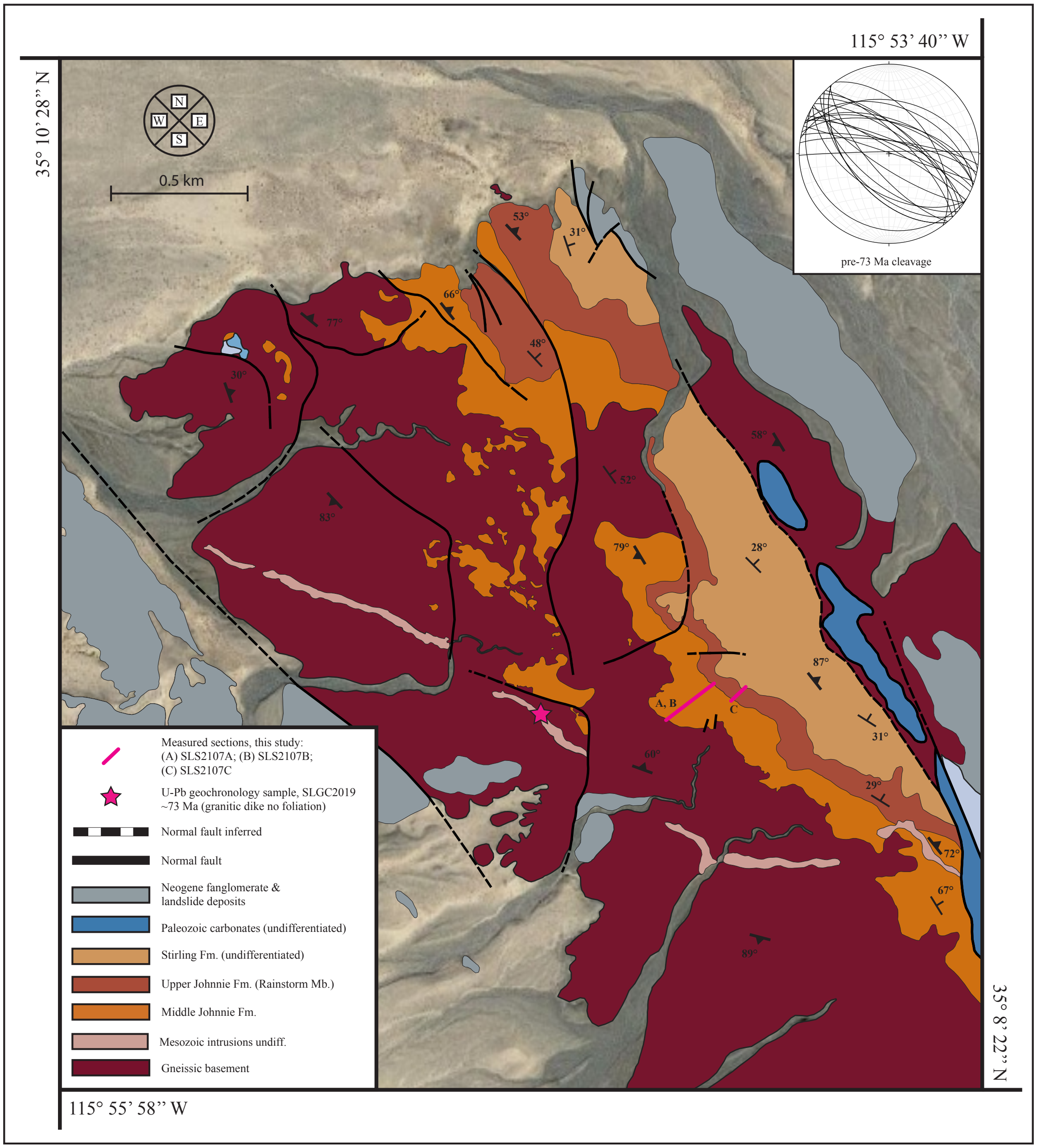

Figure 9. Geologic map of Northern Old Dad Mountain. Ediacaran section is defined from the basal Middle Johnnie Fm contact with gneissic basement through the Stirling Fm before the remaining Ediacaran – early-Cambrian strat is faulted and not exposed. Reconnaissance mapping guided by Dunne (1983) and imagery modified from Google Earth and QGIS.

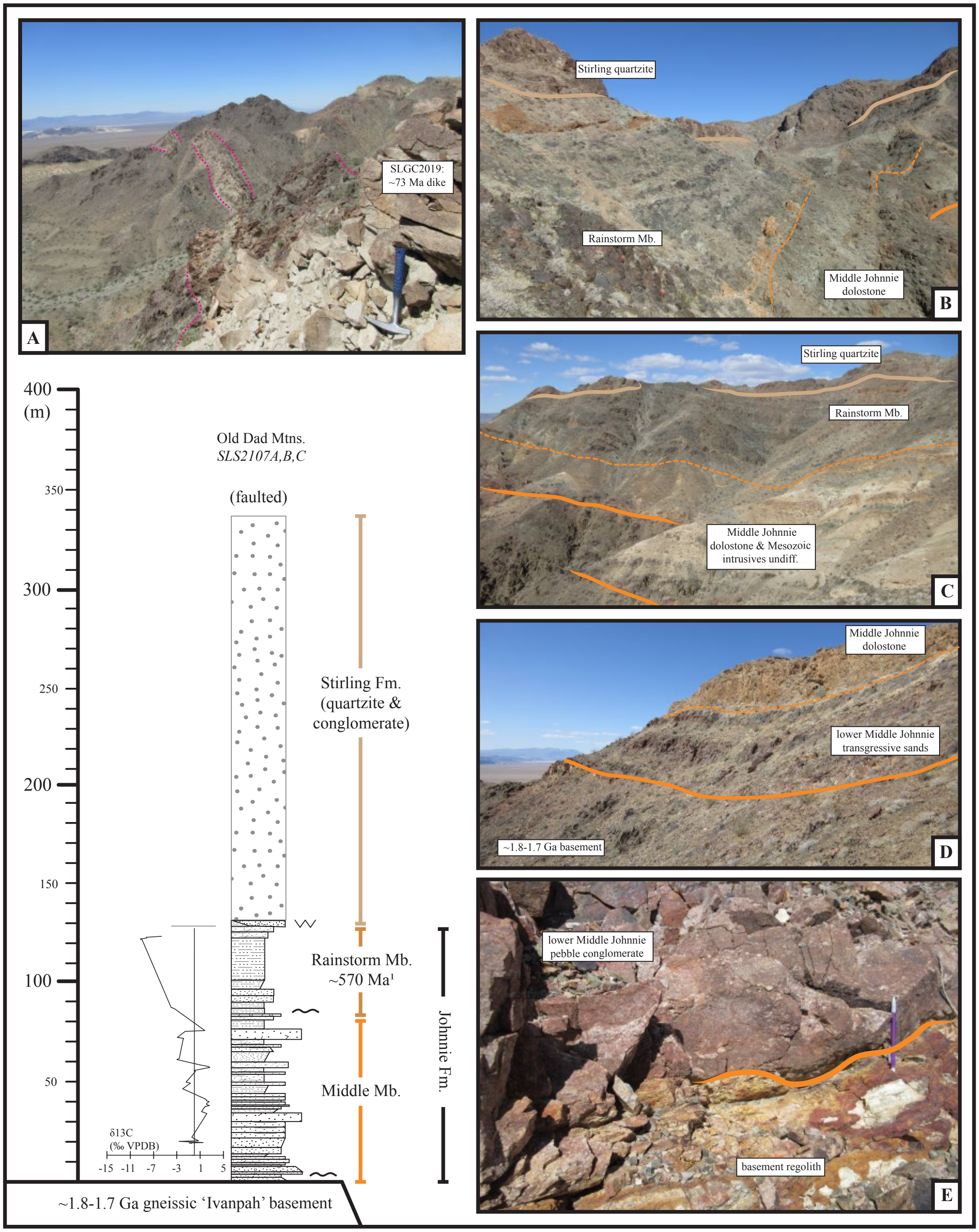

Figure 10. Measured Ediacaran stratigraphy at Northern Old Dad Mountain. A: Granitic dike intruding foliated gneissic basement, U-Pb date at ~73 Ma is minimum age constraint on foliation (Fig. 11). B: Johnnie Fm and lower Stirling Fm unconformity exposed on west-facing slope. C: Complete measured Johnnie Fm section with basal gneissic basement depositional contact and overlying Stirling Fm unconformity. D: Basal quartz-pebble conglomerate and quartzite contact with a ~5m thick oxidized paleo-regolith measured above contact with gneissic Paleoproterozoic basement. Photographs from this study.

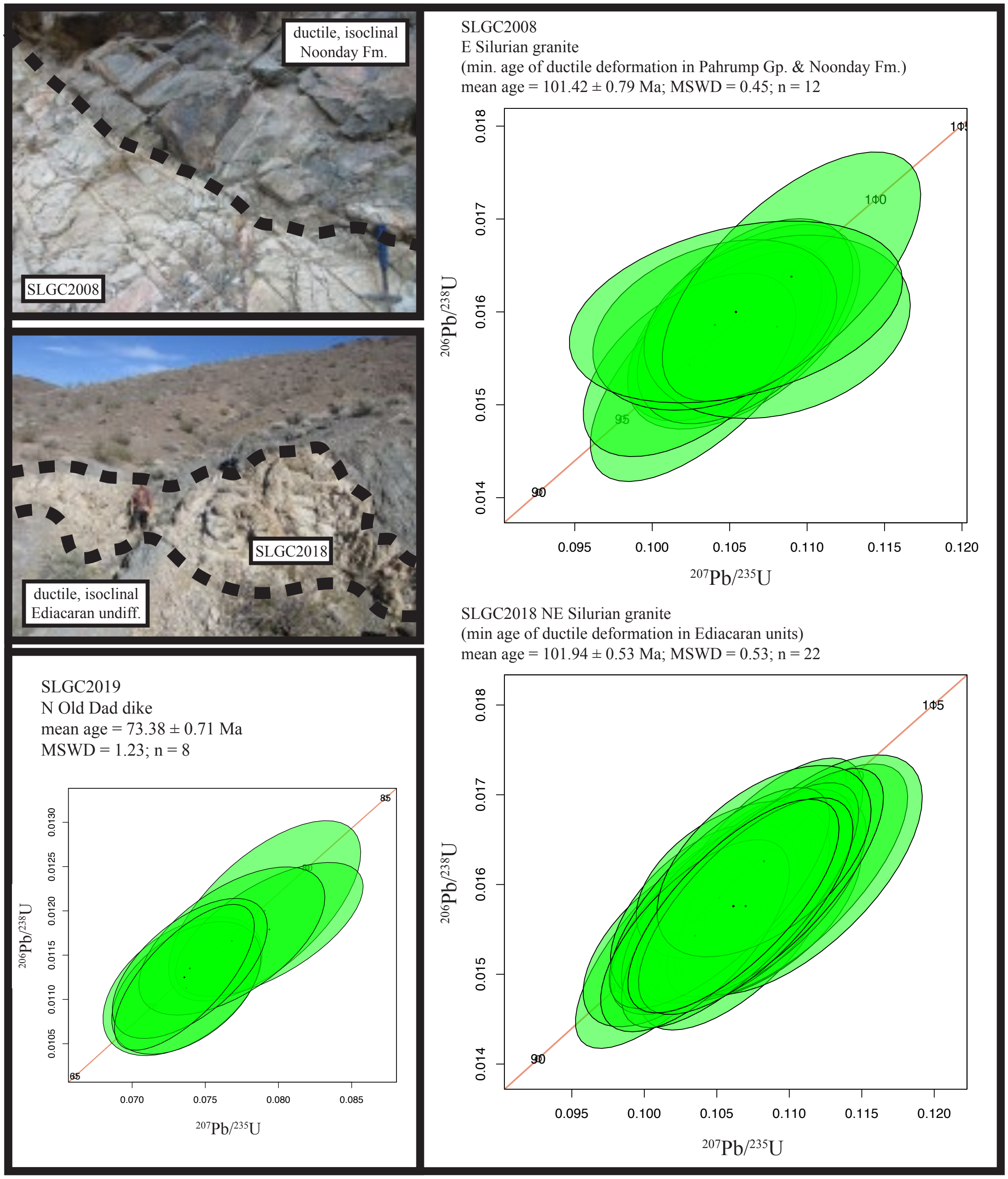

Figure 11. U-Pb zircon geochronology analyses from the Silurian Hills and Old Dad Mountain. Both Silurian Hills granite ages are minimum age constraints on ductile deformation at each site where each undeformed sample cuts mylonitized Neoproterozoic stratigraphy. Calculated with 2σ uncertainties. See Table 3 for U-Pb LA-ICP-MS data.

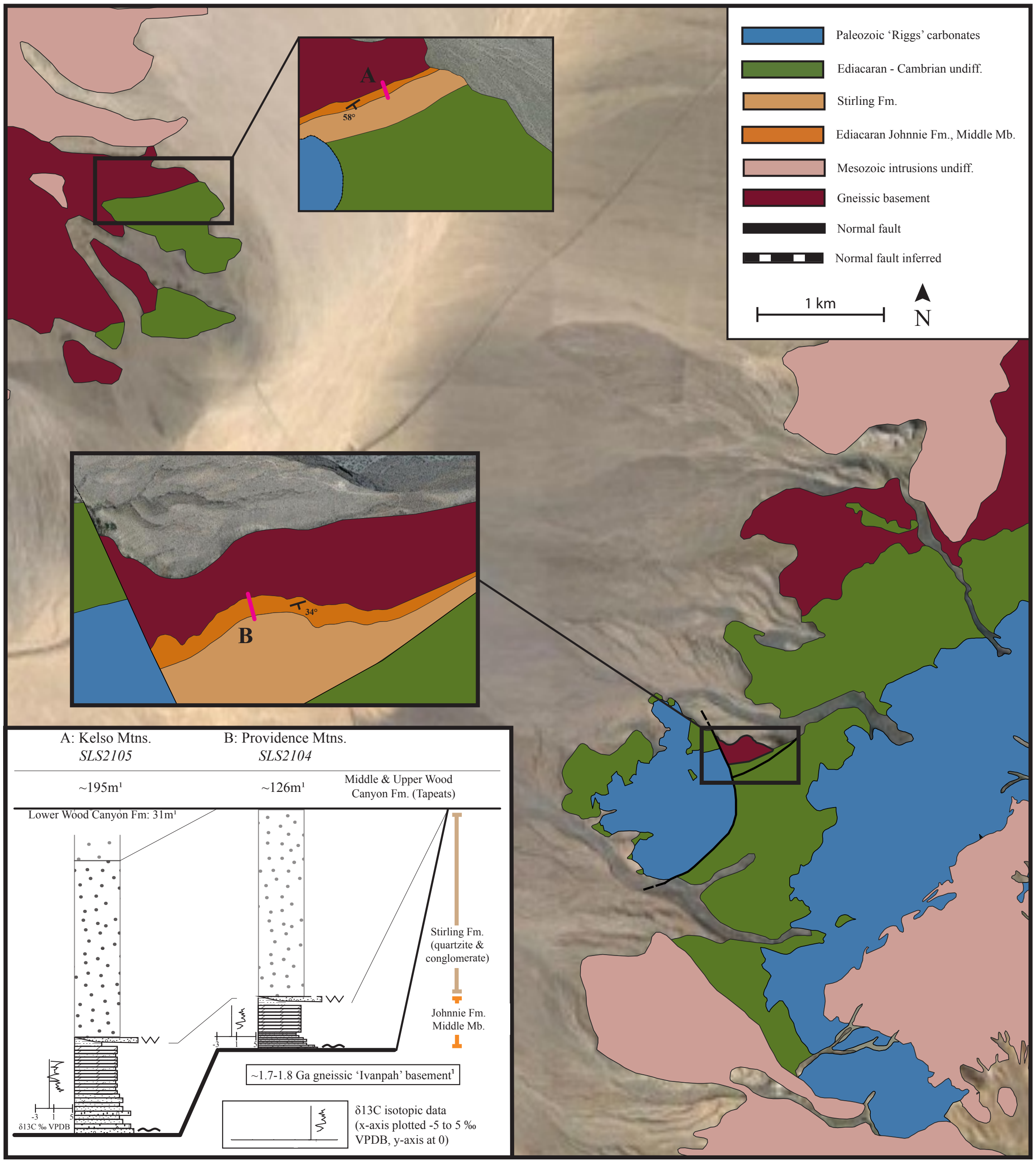

Figure 12. Overview geologic map of the southeast Kelso and western Providence Mountains with locations of measured sections. Central and southern Providence mapping synthesized from Stone et al. (2017). Imagery from Google Earth and QGIS.

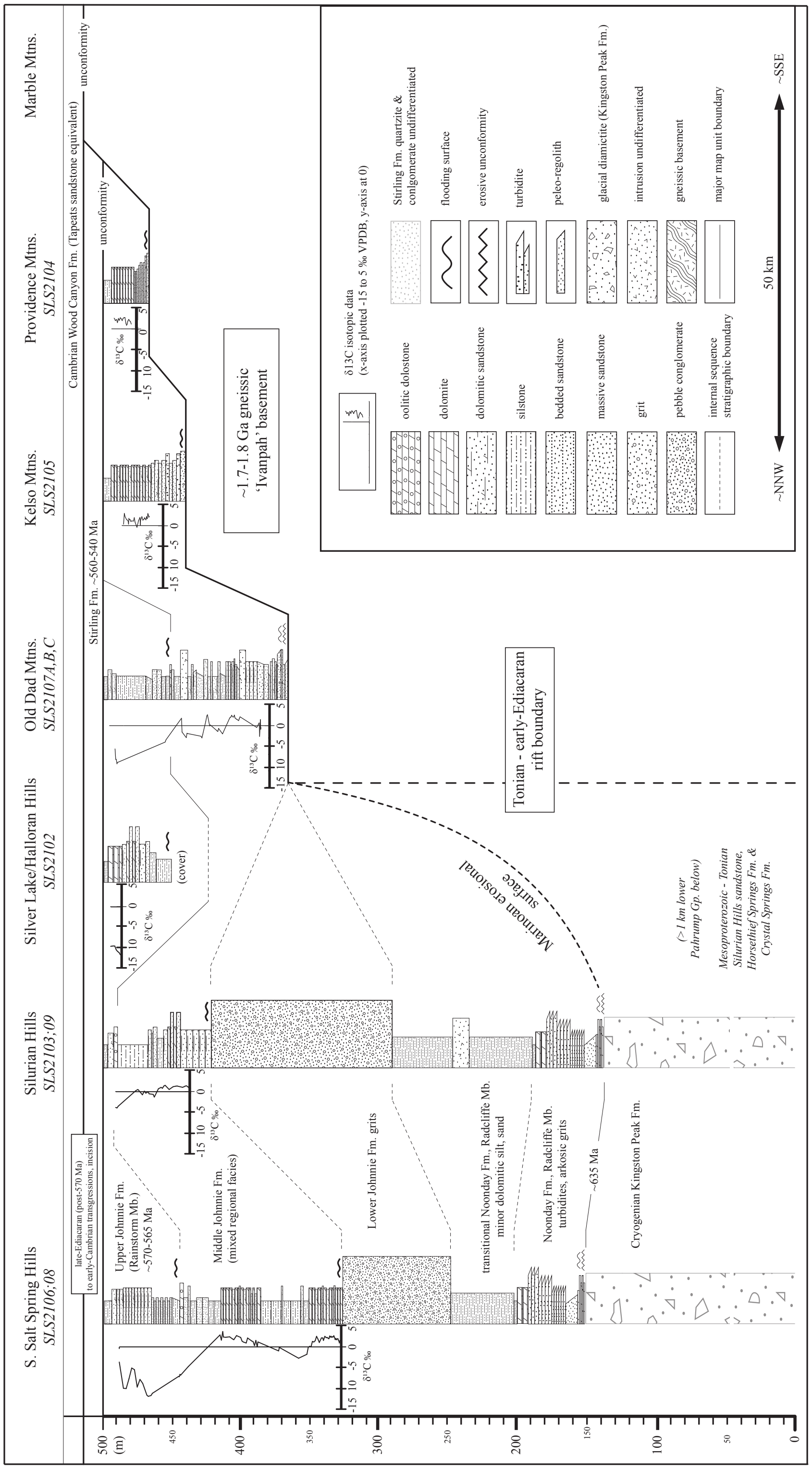

Figure 13. Tectonostratigraphic transect of the western SEDV corridor. Measured Ediacaran sections are deposited unconformably above inferred Marinoan erosional surfaces atop the Kingston Peak Fm and Paleoproterozoic basement. Note that this model depicts the SEDV Kingston Peak diamictite as Sturtian in age. Additionally, note the progressive, southeastward tapering of the Ediacaran sedimentary wedge and deep incision of the erosive unconformity at the base of the Stirling Fm.

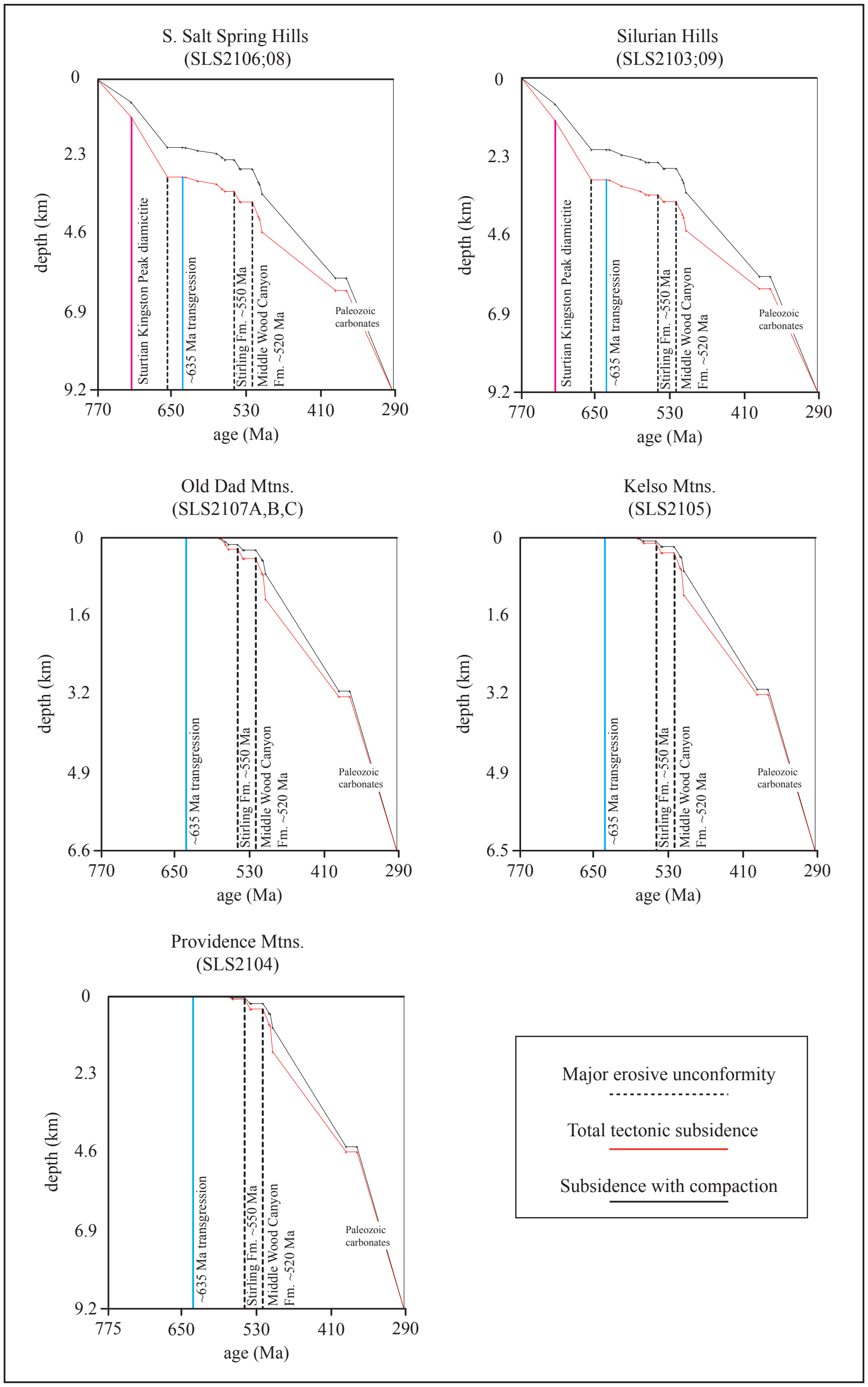

Figure 14. Schematic subsidence plot depicting key episodes of tectonic subsidence and transgressive-erosive sequences from measured Ediacaran sections encoded and plotted in *Backstrip*. Here, the record of Cryogenian glaciation in SEDV is attributed to the Sturtian glaciation at ~720 Ma and an unconformity is depicted during Marinoan time. ~635 Ma post-glacial transgression begins the Ediacaran onlapping transgressive-erosive sequences recorded at the bases of the Stirling and Wood Canyon formations. Paleozoic carbonate supersequence is lumped in thickness following the late-Cambrian Carrara and Bonanza King formations, which mark the consensus transition to a passive, thermally-subsiding margin in the Paleozoic (Levy and Christie-Blick, 1991).

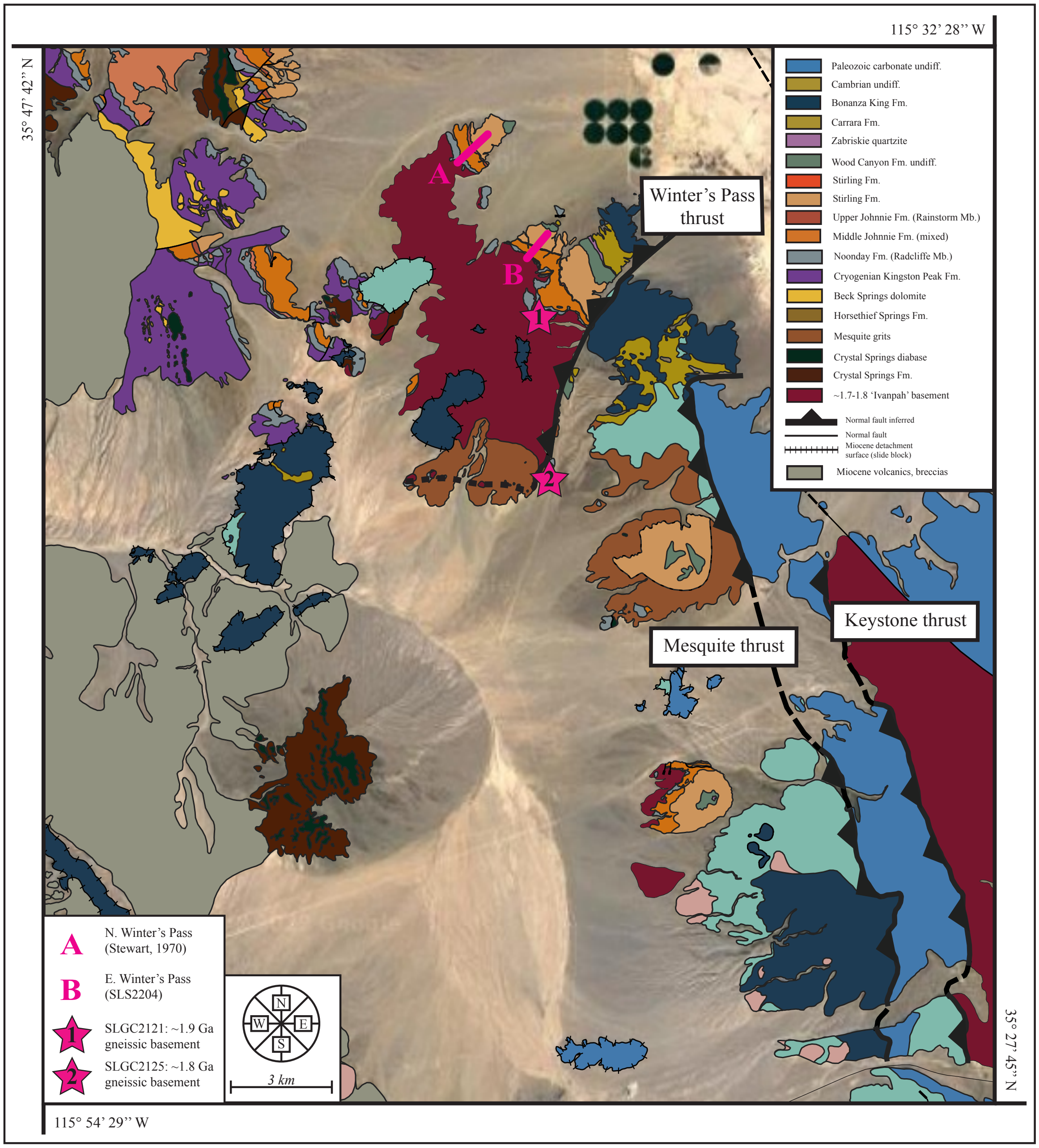

Figure 15. Overview geologic map of the eastern SEDV transect. See Figure 19 for U-Pb geochronology analyses and Figure 20 for measured sections. Note the extension of the dashed Winter’s Pass thrust to the west across the southernmost Winter’s Pass Hills where small outcrops of Noonday Fm Sentinel Peak Mb and gneissic basement are imbricated within a mylonitized, low-angle thrust complex behind the main SSW-NNE trending thrust.

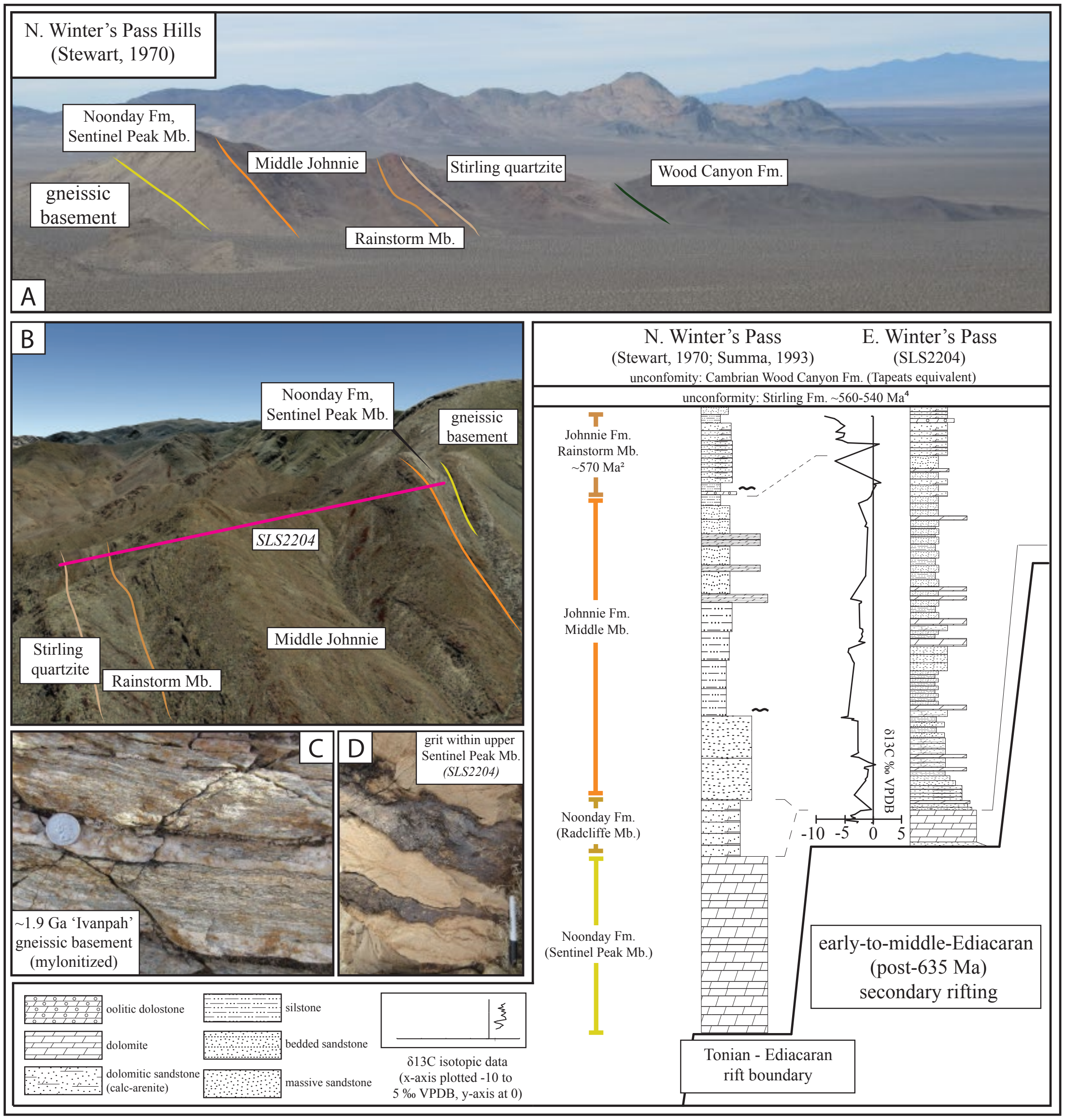

Figure 16. Measured sections from the Winter's Pass Hills. North Winter's Pass section modified from Stewart (1970) and some facies modified from Summa (1993). A: Overview of Stewart's (1970) section with key map units delineated. Modified from Google Earth. B: Measured section (this study) and location of δC^{13} samples depicted. C: Mylonitized gneissic basement ~1m below the unconformable depositional contact with the basal Noonday Fm Sentinel Peak Mb cap carbonate. D: ~10cm-scale sand and quartzite grit within the upper Noonday Fm beds. Photographs from this study.

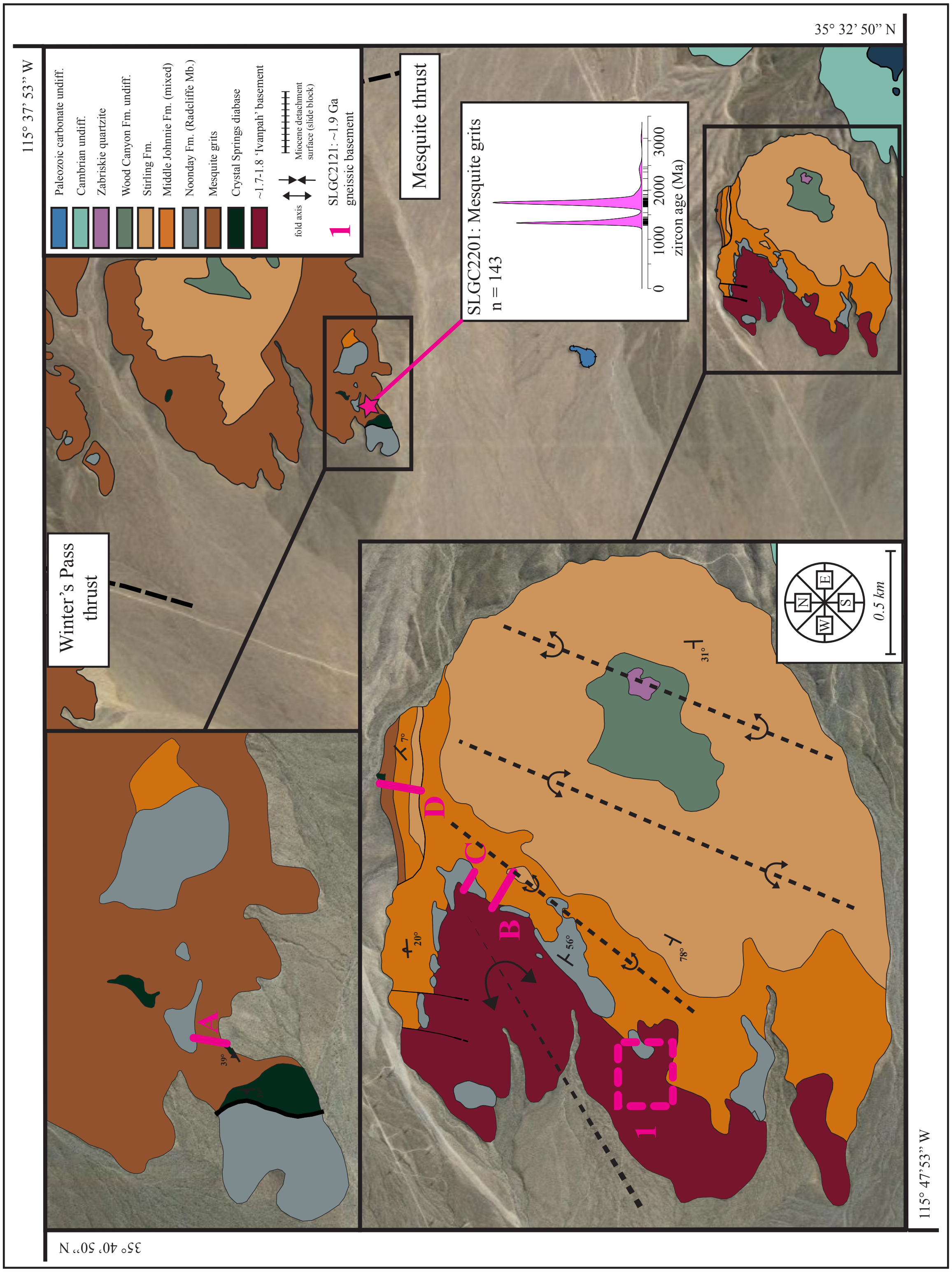

Figure 17. Geologic map of the southern Mesquite Hills and northwest Clark Mountain. See Figure 18 for additional perspective on the overturned Noonday and Johnnie formations here. U-Pb detrital zircon geochronology data shown for Mesquite quartzite grits (see discussion for interpretation).

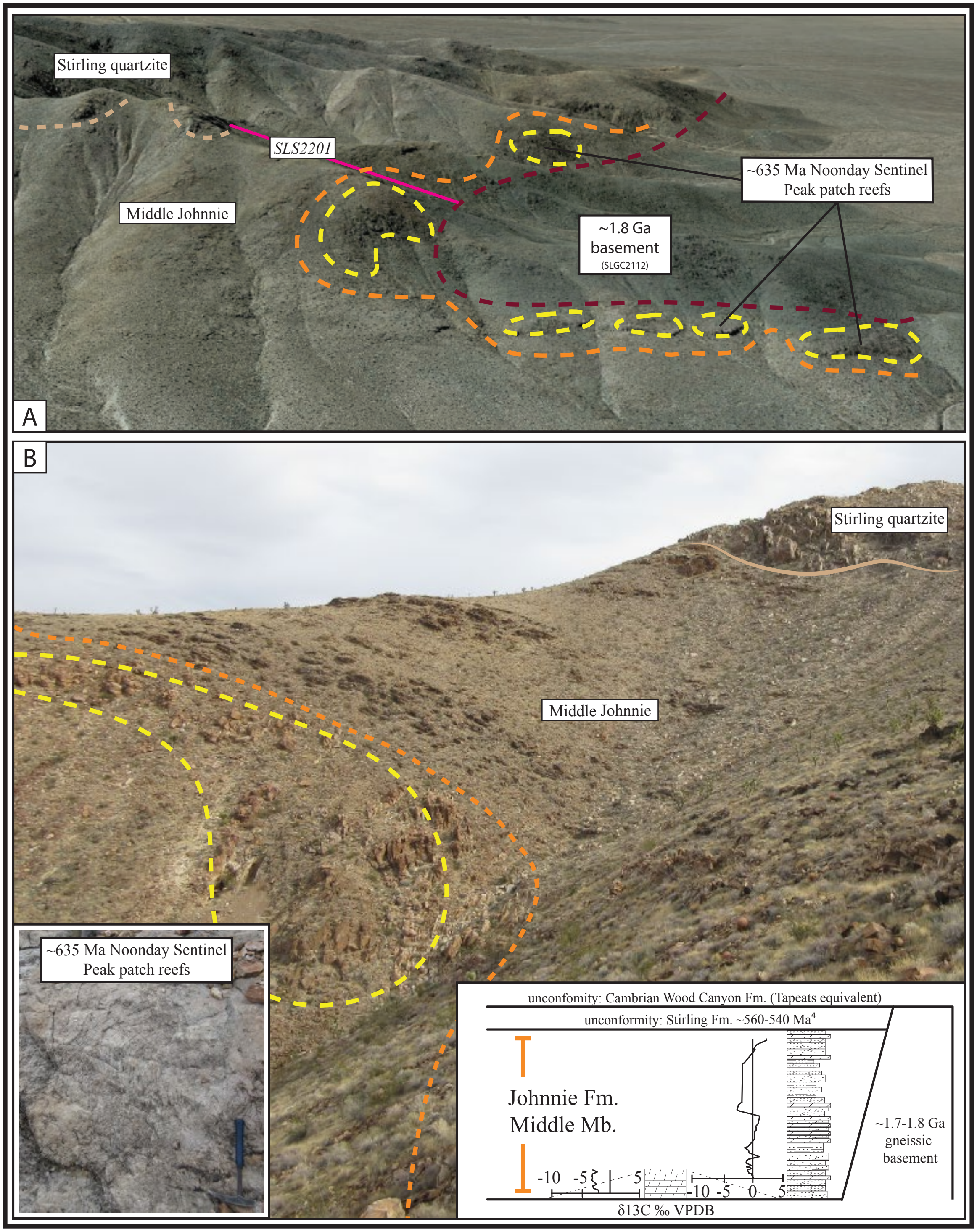

Figure 18. Measured stratigraphy and mapped isoclinal folding of the basal Ediacaran at northwest Clark Mountain. A: Southward-facing oblique view of km-scale isoclinally folded gneissic basement with unconformably overlying Noonday Fm Sentinel Peak Mb cap carbonate reefs laterally discontinuous and surrounded by lower Middle Johnnie Fm quartzite and conglomerate. B: Detailed view of Noonday Fm outcrop surrounded by Middle Johnnie siliciclastic facies; top of section and Stirling Fm unconformity in the upper right.

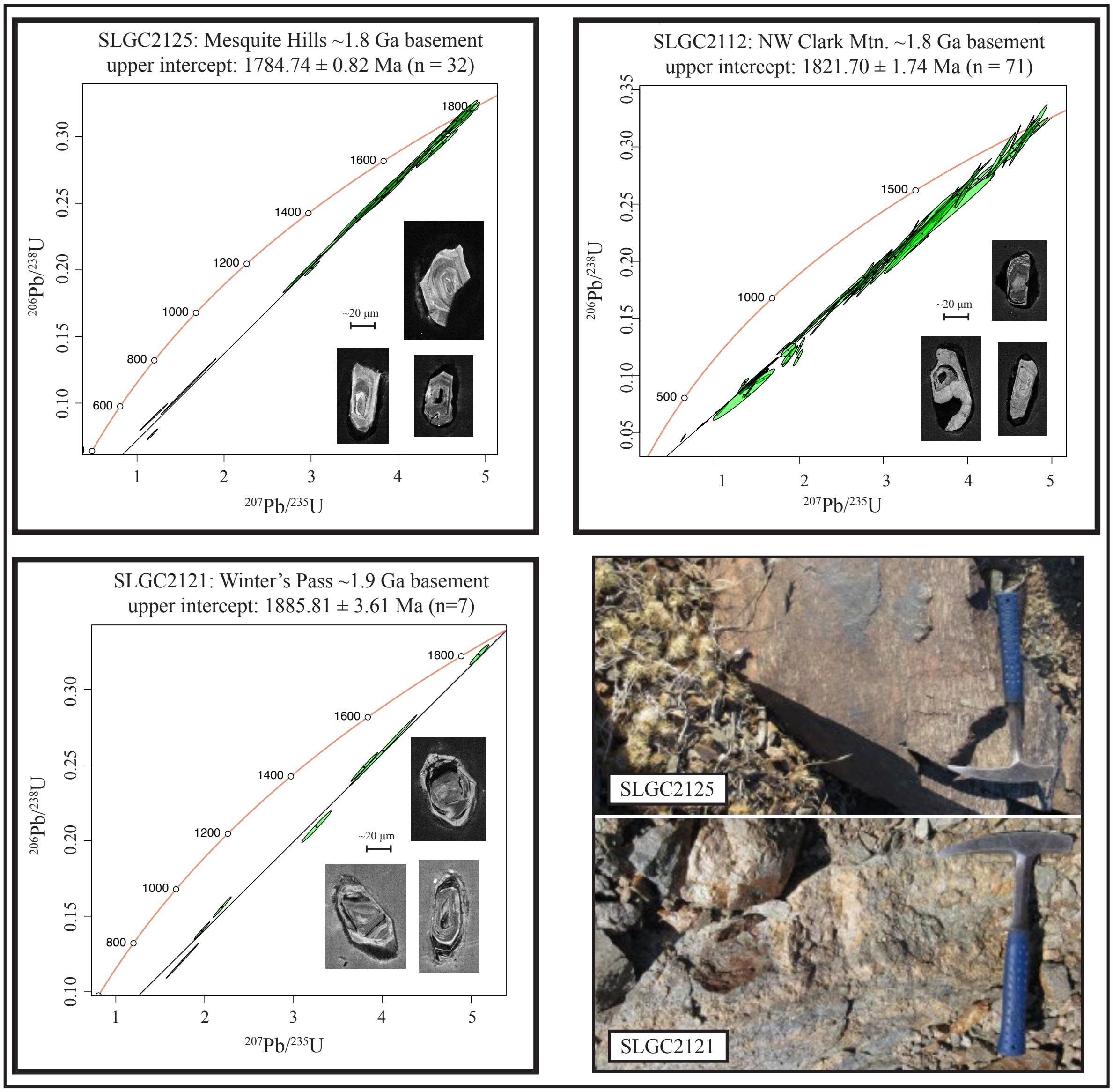

Figure 19. U-Pb zircon geochronology analyses from gneissic 'Ivanpah' basement in the Winter's Pass Hills, Mesquite Hills, and northwest Clark Mountain. Analyses from this study, performed at UCSB. Calculated with 2σ uncertainties. See methods section for analysis details and Table 3 for U-Pb LA-ICP-MS data.

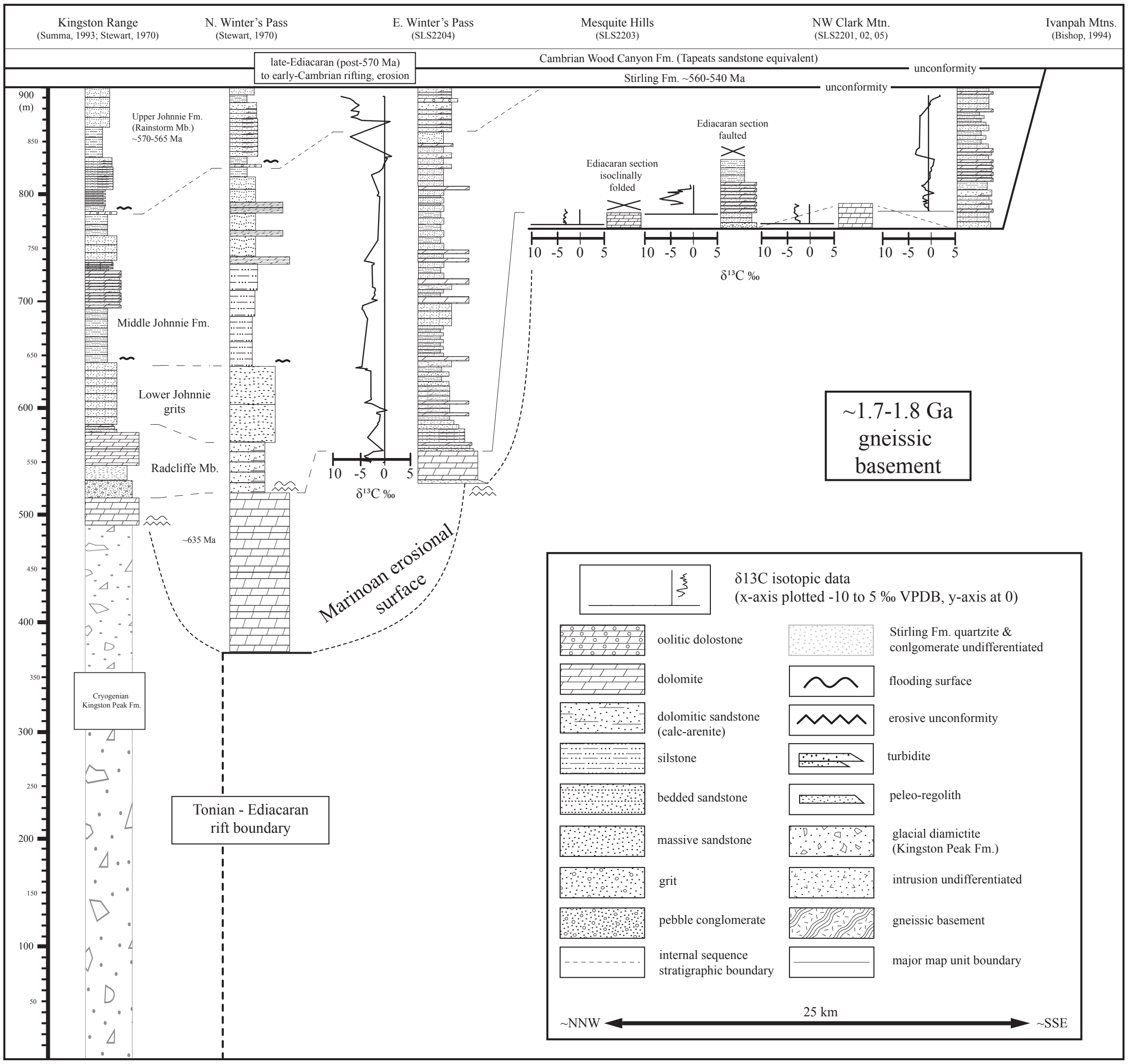

Figure 20. Tectonostratigraphic reconstruction of the SEDV eastern corridor. Measured sections are shown above inferred Marinoan erosional surface and deposited atop confirmed Paleoproterozoic basement (Fig. 19) and the Kingston Peak diamictite. Note the progressive, southeastward tapering of the Ediacaran sedimentary wedge and deep incision of the erosive unconformity at the base of the Stirling Fm.

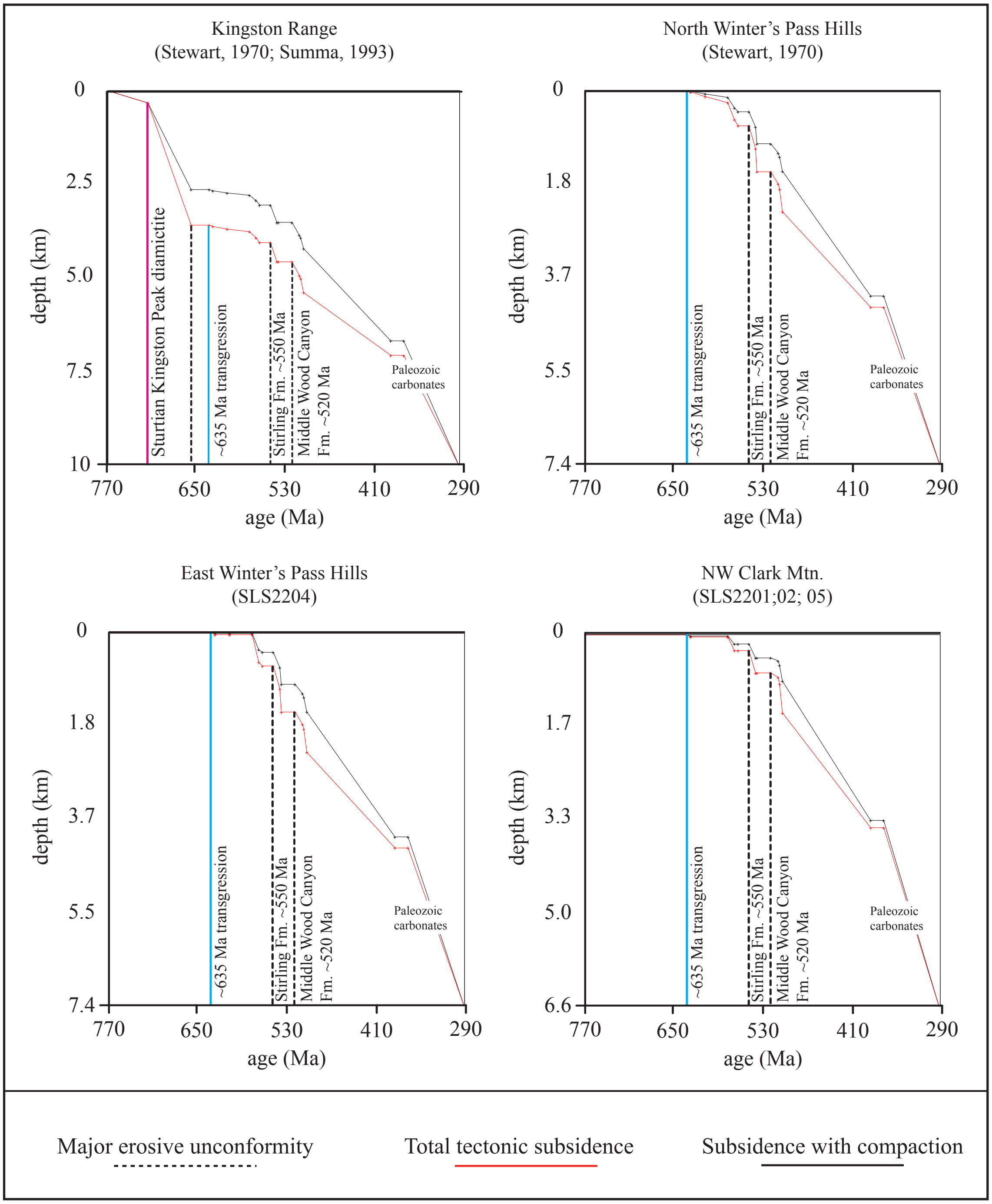

Figure 21. Schematic subsidence plot depicting key episodes of tectonic subsidence and transgressive-erosive sequences from measured Ediacaran sections encoded and plotted in *Backstrip*. Here, the record of Cryogenian glaciation in SEDV is attributed to the Sturtian glaciation at ~720 Ma and an unconformity is depicted during Marinoan time. ~635 Ma post-glacial transgression begins the Ediacaran onlapping transgressive-erosive sequences. Paleozoic carbonate supersequence formations are lumped in thickness following the late-Cambrian Carrara and Bonanza King formations, which mark the consensus beginning of a passive, thermally-subsiding margin in the Paleozoic (Levy and Christie-Blick, 1991).

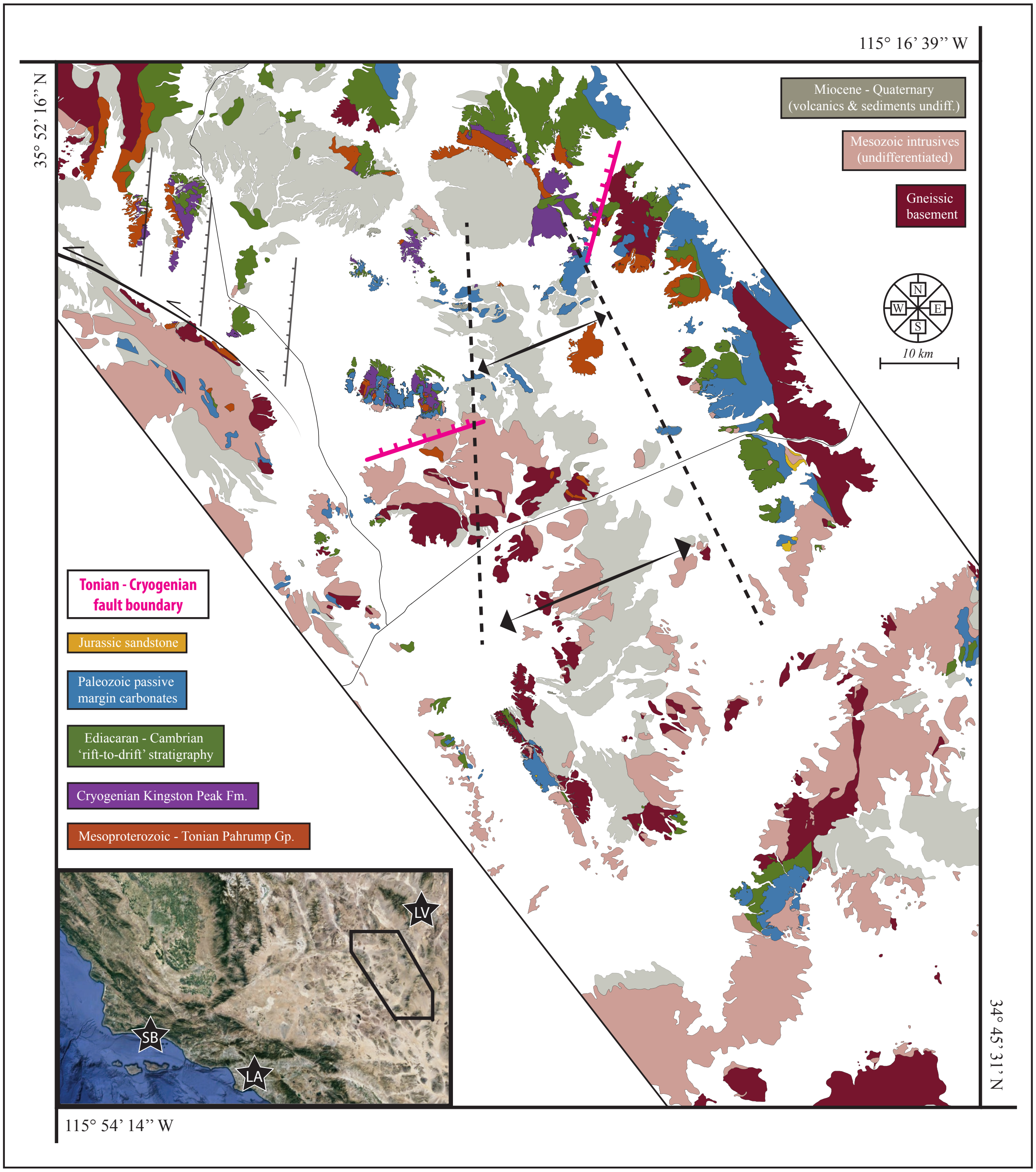

Figure 22. Reconstruction of the Miocene Kingston-Halloran crustal detachment system and Cima volcanic field. Segments of the inferred Tonian-Cryogenian basin boundary shown in pink and now separated by Miocene slide blocks in Shadow Valley, composed primarily Paleozoic carbonates (Friedmann, 1991). Modified from Google Earth and QGIS.

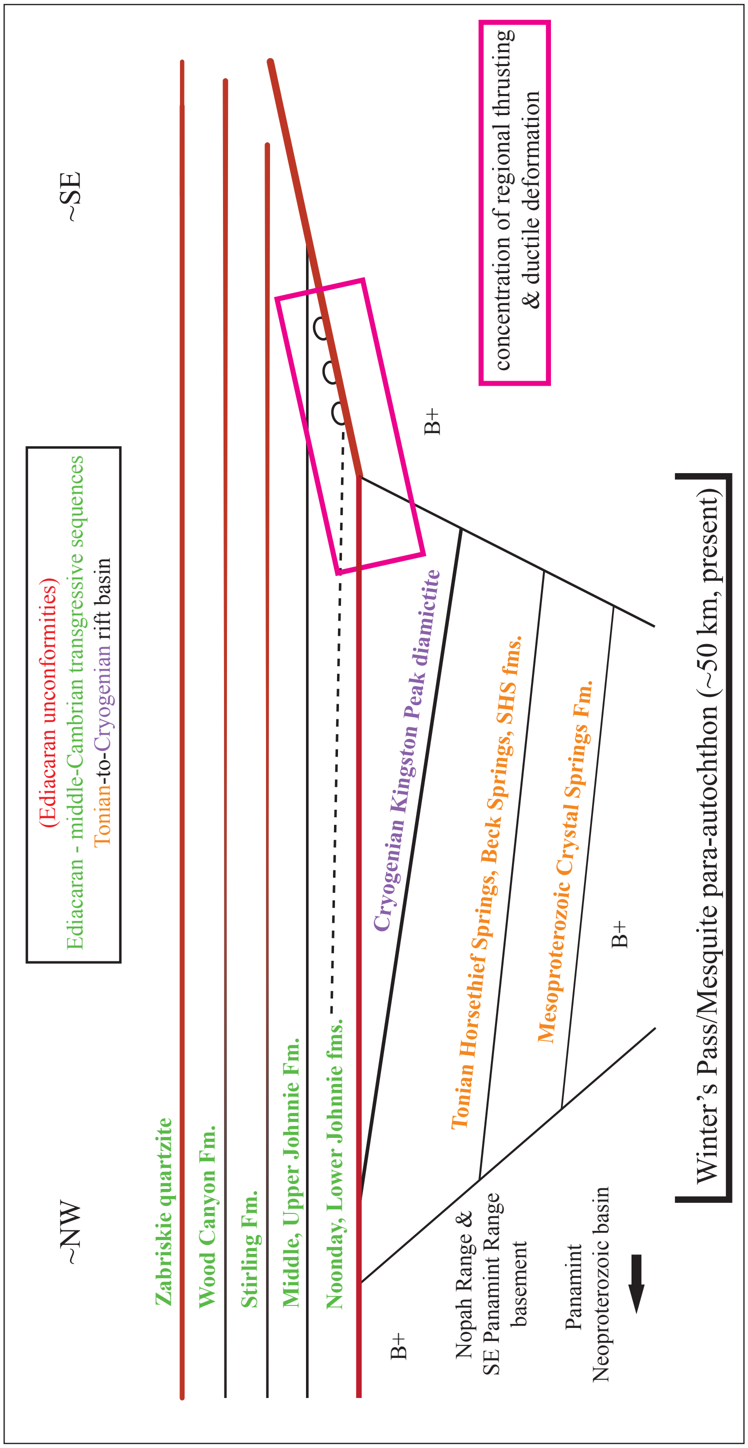

Figure 23. Schematic Tonian – Neoproterozoic basin reconstruction and para-autochthon boundary. Note the basement high bounding the northwestern edge of the basin, which in turn bounds a second Neoproterozoic basin preserved farther northwest in the Panamint Mountains (Nelson et al., 2020). Concentration of Mesozoic deformation highlighted along the southeastern boundary, or rift boundary, of the Neoproterozoic basin. Ductile deformation constrained to pre-100 Ma in this study (Fig. 11) is concentrated at field sites located adjacent to inferred Tonian—Cryogenian structural boundary, shown in pink: (1) Silurian Hills; (2) Winter's Pass Hills; and (3) Northwest Clark Mountain.

Appendix

Table 1.

Location	Data type	Coordinates
South Salt Spring Hills	measured section SLS2106 & C-O isotope samples	35°35'15.23"N, 116°16'40.34"W
	measured section SLS2108 & C-O isotope samples	35°35'11.60"N, 116°16'8.93"W
Silurian Hills	measured section SLS2103 & C-O isotope samples	35°32'56.21"N, 116° 5'36.56"W
	measured section SLS2109 & C-O isotope samples	35°32'55.50"N, 116° 5'14.04"W
	U-Pb geochronology sample SLGC2008	35°30'22.00"N, 116° 1'43.69"W
	U-Pb geochronology sample SLGC2018	35°31'42.94"N, 116° 1'16.84"W
Silver Lake Hills	measured section SLS2102 & C-O isotope samples	35°21'44.03"N, 116° 9'29.05"W
Old Dad Mountain	measured section SLS2107A & C-O isotope samples	35° 9'19.20"N, 115°54'32.19"W
	measured section SLS2107B & C-O isotope samples	35° 9'23.48"N, 115°54'29.44"W
	measured section SLS2107C & C-O isotope samples	35° 9'20.75"N, 115°54'21.61"W
	U-Pb geochronology sample SLGC2019	35° 9'21.41"N, 115°54'53.36"W
Kelso Mountains	measured section SLS2105 & C-O isotope samples	35° 3'24.98"N, 115°40'48.30"W
Providence Mountains	measured section SLS2104 & C-O isotope samples	34°58'21.77"N, 115°34'38.28"W
Winter's Pass	measured section SLS2204 & C-O isotope samples	35°43'45.21"N, 115°43'7.37"W
	U-Pb geochronology sample SLGC2121	35°42'51.54"N, 115°43'3.12"W
Mesquite Hills	measured section SLS2203 & C-O isotope samples	35°36'57.94"N, 115°41'7.57"W
	U-Pb geochronology sample SLGC2125	35°39'29.24"N, 115°42'49.33"W
Clark Mountain	measured section SLS2201 & C-O isotope samples	35°33'52.59"N, 115°39'41.87"W
	measured section SLS2202 & C-O isotope samples	35°33'50.31"N, 115°39'44.39"W
	measured section SLS2205 & C-O isotope samples	35°34'12.99"N, 115°39'15.10"W
	U-Pb geochronology sample SLGC2112	35°33'28.63"N, 115°40'3.67"W

Table 1. Coordinates of measured sections, associated C and O isotope samples, and U-Pb geochronology samples. UC Berkeley Center for Stable Isotope Biogeochemistry (CSIB) procedure: The amount of bulk powder samples containing about 10 to 100 microgram calcite or aragonite were reacted with "100%" H_3PO_4 at 90^{o} C for 10 mins to generate CO_2 gas for both carbon and oxygen isotope analyses ($\delta^{13}C$ and $\delta^{18}O$) using a GV IsoPrime mass spectrometer with Dual-Inlet and MultiCarb systems in the Center for Stable Isotope Biogeochemistry (CSIB) at Department of Integrative Biology, University of California at Berkeley. Several replicates of one international standard NBS19, and two lab standards $CaCO_3$-I & II were measured along with samples for each run. The overall external analytical precision is about ±0.05‰ for $\delta^{13}C$ and about ±0.07‰ for $\delta^{18}O$

Table 2.

Analysis 1			
No	Sample	d^{13}C	d^{18}O
		(‰ VPDB)	(‰ VPDB)
1	NBS-19 1	2.13	-2.22
2	NBS-19 2	2.05	-2.19
3	NBS-19 3	2.01	-2.36
4	CaCO3 I 1	-40.22	-21.50
5	CaCO3 I 2	-40.29	-21.46
6	CaCO3 I 3	-40.22	-21.36
7	CaCO3 II 1	-2.74	-12.60
8	CaCO3 II 2	-2.56	-12.42
9	SLS2101A - 5.1	0.80	-4.87
10	SLS2101A - 6.1	0.86	-3.75
11	SLS2101A - 7	1.70	-4.31
12	SLS2101A - 7.8	1.63	-5.41
13	SLS2101A - 8.6	1.48	-4.27
14	SLS2101A - 9.3	0.88	-4.87
15	SLS2101A - 17	1.39	-5.74
16	SLS2101A - 23.3	2.41	-5.28
17	SLS2101A - 24	2.17	-6.51
18	SLS2101A - 24.5	2.87	-4.47
19	SLS2101A - 26.5	2.97	-6.48
20	SLS2101A - 27.5	4.04	-6.99
21	SLS2101A - 28.5	3.72	-6.57
22	SLS2101A - 29.1	3.24	-6.94
23	SLS2101A - 29.5	3.58	-4.66
24	SLS2101A - 31.8	4.31	-4.94
25	SLS2101A - 33.9	3.16	-9.75
26	SLS2101A - 35	3.76	-6.21
27	SLS2101A - 36	2.68	-8.03
28	SLS2101A - 38.5	3.31	-5.62
29	SLS2101A - 39	2.95	-6.50
30	SLS2101A - 41.9	3.39	-5.50
31	SLS2101A - 48.3	0.40	-7.12
32	SLS2101A - 49	-2.41	-8.73
33	SLS2101B - 0	-4.05	-8.04
34	SLS2101B - 0.8	-4.28	-8.27
35	SLS2101B - 1.6	-5.17	-8.43
36	SLS2101B - 2.2	-4.12	-8.97
37	SLS2101B - 24	-10.14	-8.03
38	SLS2101B - 27	-9.21	-9.14
39	SLS2101B - 30	-8.44	-8.56
40	SLS2101B - 40	-9.16	-9.39
41	SLS2101B - 45	-10.57	-9.30
42	SLS2101B - 48	-9.72	-9.54
43	SLS2101B - 51	-9.01	-8.43
44	SLS2101B - 54	-9.62	-9.12

45	SLS2101B - 55	-9.79	-9.59
46	SLS2101B - 58	-9.46	-10.32
47	SLS2101B - 61	-7.81	-10.79
48	SLS2101B - 62.5	-9.62	-8.67
49	SLS2101B - 64	-9.07	-8.54
50	SLS2101B - 68	-8.71	-8.32
51	SLS2101B - 71	-6.66	-5.43
52	SLS2102 - 0	-11.51	-8.85
53	SLS2102 - 1.5	-11.70	-7.28
54	SLS2102 - 3	-11.15	-7.55
55	SLS2102 - 4.5	-10.89	-9.54
56	SLS2102 - 6	-10.49	-11.17
57	SLS2102 - 7.5	-9.58	-13.13
58	SLS2102 - 9	-9.55	-9.44
59	CaCO3II 3	-2.67	-12.59
60	CaCO3II 4	-2.63	-12.45
Analysis 2			
No	Sample	$d^{13}C$	$d^{18}O$
		(‰ VPDB)	(‰ VPDB)
1	NBS-19 1	2.16	-2.24
2	NBS-19 2	1.99	-2.28
3	NBS-19 3	1.99	-2.18
4	CaCO3 I 1	-40.12	-21.33
5	CaCO3 I 2	-40.26	-21.49
6	CaCO3 I 3	-40.36	-21.43
7	CaCO3 II 1	-2.59	-12.53
8	CaCO3 II 2	-2.68	-12.61
9	SLS2102 - 10.5	-9.60	-5.86
10	SLS2102 - 12	-9.64	-8.95
11	SLS2103A - 0.3	-5.20	-16.10
12	SLS2103A - 0.7	-4.91	-12.69
13	SLS2103A - 1.5	-4.11	-15.87
14	SLS2103A - 2.2	-4.15	-16.86
15	SLS2103A - 3	-4.00	-16.36
16	SLS2103A - 4	-3.98	-16.09
17	SLS2103B - 3.1	-1.31	-15.49
18	SLS2103B - 3.9	-0.66	-14.89
19	SLS2103B - 7	-0.51	-12.42
20	SLS2103B - 7.5	-0.16	-11.61
21	SLS2103B - 8	0.02	-11.81
22	SLS2103B - 8.5	-0.20	-11.36
23	SLS2103B - 9.5	-0.35	-11.45
24	SLS2103B - 10.5	0.14	-9.89
25	SLS2103B - 12	-0.75	-9.43
26	SLS2103B - 15	0.43	-9.97
27	SLS2103B - 15.5	0.52	-7.24

28	SLS2103B - 17	0.23	-7.81
29	SLS2103B - 30	-3.51	-9.18
30	SLS2103B - 31	-3.95	-8.90
31	SLS2103B - 32	-3.84	-8.51
32	SLS2104 - 5.2	1.15	-7.50
33	SLS2104 - 5.9	1.82	-6.42
34	SLS2104 - 6.5	1.92	-6.59
35	SLS2104 - 7.2	2.32	-5.56
36	SLS2104 - 8	1.89	-6.49
37	SLS2104 - 8.5	1.13	-10.47
38	SLS2104 - 9	0.86	-10.47
39	SLS2104 - 9.5	1.37	-9.08
40	SLS2104 - 10.3	2.78	-6.54
41	SLS2104 - 11	2.73	-6.56
42	SLS2104 - 11.8	2.57	-7.61
43	SLS2104 - 12.5	2.01	-7.95
44	SLS2104 - 13.4	2.54	-6.70
45	SLS2104 - 14	2.72	-6.59
46	SLS2104 - 14.8	2.05	-6.46
47	SLS2104 - 15.5	2.56	-6.33
48	SLS2104 - 16.3	1.51	-7.32
49	SLS2104 - 17	2.31	-5.45
50	SLS2104 - 18	2.01	-6.00
51	SLS2104 - 18.5	2.42	-4.41
52	SLS2104 - 19	2.62	-4.99
53	SLS2105 - 18.2	2.40	-6.71
54	SLS2105 - 19	2.15	-7.88
55	SLS2105 - 19.5	2.65	-7.34
56	SLS2105 - 20.3	3.12	-6.29
57	SLS2105 - 21	1.76	-9.10
58	SLS2105 - 21.8	1.94	-10.37
59	CaCO3II 3	-2.74	-12.42
60	CaCO3II 4	-2.50	-12.68
Analysis 3			
No	Sample	d^{13}C	d^{18}O
		(‰ VPDB)	(‰ VPDB)
1	NBS-19 1	2.06	-2.08
2	NBS-19 2	1.98	-2.24
3	NBS-19 3	2.00	-2.26
4	CaCO3 I 1	-40.11	-21.29
5	CaCO3 I 2	-40.34	-21.47
6	CaCO3 I 3	-40.30	-21.35
7	CaCO3 II 1	-2.59	-12.61
8	CaCO3 II 2	-2.59	-12.69
9	SLS2105 - 22	2.32	-6.72
10	SLS2105 - 22.8	1.46	-7.95

11	SLS2105 - 23.8	1.75	-7.87
12	SLS2105 - 24.5	2.03	-7.29
13	SLS2105 - 25.3	1.67	-8.60
14	SLS2105 - 26	1.55	-7.02
15	SLS2105 - 26.8	1.39	-9.68
16	SLS2105 - 28	2.32	-9.52
17	SLS2105 - 29	1.81	-11.43
18	SLS2105 - 29.8	1.35	-10.07
19	SLS2105 - 30	0.13	-11.77
20	SLS2105 - 30.5	2.12	-8.44
21	SLS2105 - 32.5	1.25	-9.29
22	SLS2105 - 34.5	-0.43	-11.91
23	SLS2105 - 37	0.90	-10.31
24	SLS2105 - 38	2.07	-6.97
25	SLS2105 - 39	1.17	-8.46
26	SLS2105 - 41.5	1.21	-8.65
27	SLS2105 - 42.5	1.06	-7.77
28	SLS2105 - 43.5	1.58	-7.33
29	SLS2105 - 44.5	1.52	-10.08
30	SLS2105 - 45	1.88	-9.61
31	SLS2105 - 45.5	0.36	-11.80
32	SLS2105 - 46	1.13	-9.34
33	SLS2105 - 47	1.43	-6.53
34	SLS2105 - 48	1.52	-6.46
35	SLS2105 - 50	2.29	-6.62
36	SLS2105 - 51	3.14	-6.93
37	SLS2105 - 52	0.35	-7.20
38	SLS2106 - 0	1.18	-9.91
39	SLS2106 - 0.5	1.46	-9.79
40	SLS2106 - 1	1.55	-8.39
41	SLS2106 - 1.5	1.20	-8.72
42	SLS2106 - 2	1.48	-8.23
43	SLS2106 - 2.5	1.99	-8.07
44	SLS2106 - 3	1.97	-8.89
45	SLS2106 - 3.5	1.73	-8.44
46	SLS2106 - 4	2.06	-8.65
47	SLS2106 - 4.5	1.78	-8.24
48	SLS2106 - 5	2.32	-7.93
49	SLS2106 - 5.5	2.73	-7.39
50	SLS2106 - 6	2.40	-8.27
51	SLS2106 - 6.5	2.49	-8.32
52	SLS2106 - 7	2.32	-8.24
53	SLS2106 - 7.5	2.60	-7.82
54	SLS2106 - 8	2.37	-8.18
55	SLS2106 - 8.5	2.65	-7.91
56	SLS2106 - 9	2.00	-9.41
57	SLS2106 - 9.5	2.04	-9.63

58	SLS2106 - 10	2.25	-7.92
59	CaCO3II 3	-2.62	-12.51
60	CaCO3II 4	-2.51	-12.70
Analysis 4			
No	Sample	d^{13}C	d^{18}O
		(‰ VPDB)	(‰ VPDB)
1	NBS-19 1	2.04	-2.32
2	NBS-19 2	2.08	-2.08
3	NBS-19 3	1.98	-2.15
4	CaCO3 I 1	-40.27	-21.31
5	CaCO3 I 2	-40.16	-21.29
6	CaCO3 I 3	-40.32	-21.48
7	CaCO3 II 1	-2.66	-12.74
8	CaCO3 II 2	-2.56	-12.59
9	SLS2106 - 10.5	2.29	-8.71
10	SLS2106 - 11	2.24	-8.28
11	SLS2106 - 12	2.58	-7.72
12	SLS2106 - 13	1.58	-9.23
13	SLS2106 - 13.5	2.18	-9.57
14	SLS2106 - 14.5	2.18	-9.00
15	SLS2106 - 16	1.08	-10.89
16	SLS2106 - 17	1.90	-9.76
17	SLS2106 - 18	2.58	-7.34
18	SLS2106 - 19	1.50	-7.28
19	SLS2106 - 20	1.19	-8.24
20	SLS2106 - 21	1.33	-6.81
21	SLS2106 - 22	0.03	-7.99
22	SLS2106 - 23	0.15	-7.62
23	SLS2106 - 24	-0.08	-7.89
24	SLS2106 - 25	-1.80	-8.17
25	SLS2106 - 31	-2.76	-6.87
26	SLS2106 - 45	-0.13	-8.26
27	SLS2106 - 45.5	-0.98	-8.61
28	SLS2106 - 60.5	1.21	-7.76
29	SLS2106 - 61	-0.02	-7.05
30	SLS2106 - 62	1.58	-5.53
31	SLS2106 - 63	0.32	-6.66
32	SLS2106 - 64	1.28	-9.43
33	SLS2106 - 65	1.44	-9.41
34	SLS2106 - 68	2.17	-8.00
35	SLS2106 - 69	0.95	-8.36
36	SLS2106 - 71	1.18	-8.38
37	SLS2106 - 72	1.40	-8.48
38	SLS2106 - 73	2.30	-8.10
39	SLS2106 - 76	2.75	-9.58
40	SLS2106 - 78	1.75	-10.94

41	SLS2106 - 79	1.96	-7.97
42	SLS2106 - 81	2.45	-8.42
43	SLS2106 - 83	2.38	-9.58
44	SLS2106 - 84	2.35	-9.22
45	SLS2106 - 85.5	2.40	-7.94
46	SLS2106 - 86	3.74	-8.00
47	SLS2106 - 87	1.65	-9.40
48	SLS2106 - 87.5	2.36	-7.87
49	SLS2106 - 88	2.91	-7.69
50	SLS2106 - 111	-4.80	-11.08
51	SLS2106 - 116.5	-6.88	-7.26
52	SLS2106 - 117	-6.70	-7.37
53	SLS2106 - 117.5	-7.27	-7.17
54	SLS2106 - 118	-7.19	-6.81
55	SLS2106 - 137	-11.31	-10.11
56	SLS2106 - 138	-11.85	-10.04
57	SLS2106 - 140	-12.05	-9.56
58	SLS2106 - 141	-11.76	-11.66
59	CaCO3II 3	-2.68	-12.74
60	CaCO3II 4	-2.55	-12.59
Analysis 5			
No	Sample	d^{13}C	d^{18}O
		(‰ VPDB)	(‰ VPDB)
1	NBS-19 1	2.13	-2.22
2	NBS-19 2	2.05	-2.23
3	NBS-19 3	2.00	-2.27
4	CaCO3 I 1	-40.15	-21.43
5	CaCO3 I 2	-40.22	-21.35
6	CaCO3 I 3	-40.37	-21.50
7	CaCO3 II 1	-2.73	-12.63
8	CaCO3 II 2	-2.56	-12.45
9	SLS2106 - 144	-8.90	-9.43
10	SLS2106 - 146	-7.92	-8.26
11	SLS2106 - 148	-9.79	-9.51
12	SLS2106 - 150	-5.55	-10.77
13	SLS2106 - 152	-5.14	-9.60
14	SLS2106 - 154	-7.81	-10.25
15	SLS2106 - 156	-10.15	-9.10
16	SLS2106 - 158	-10.09	-10.05
17	SLS2106 - 161	-3.69	-10.75
18	SLS2107A - 6.1	-0.46	-12.76
19	SLS2107A - 6.3	-0.89	-15.06
20	SLS2107A - 6.5	1.49	-12.84
21	SLS2107A - 7.1	-2.63	-17.77
22	SLS2107A - 7.4	0.70	-14.57
23	SLS2107A - 9.2	-0.44	-16.76

24	SLS2107A - 21.4	2.16	-9.32
25	SLS2107A - 21.9	1.69	-9.07
26	SLS2107A - 22.4	1.23	-10.01
27	SLS2107A - 23	1.39	-8.39
28	SLS2107A - 23.5	1.49	-7.61
29	SLS2107A - 24	1.58	-7.70
30	SLS2107A - 24.5	1.75	-8.03
31	SLS2107A - 25	1.85	-8.29
32	SLS2107A - 25.5	2.59	-7.60
33	SLS2107A - 26	2.12	-8.74
34	SLS2107A - 26.5	2.10	-9.05
35	SLS2107A - 27	2.28	-9.45
36	SLS2107A - 27.5	2.53	-8.80
37	SLS2107A - 28	2.09	-10.10
38	SLS2107A - 28.5	2.04	-10.86
39	SLS2107A - 29	1.79	-11.30
40	SLS2107B - 5.1	-2.00	-11.96
41	SLS2107B - 5.3	-1.92	-10.71
42	SLS2107B - 8	-0.67	-7.92
43	SLS2107B - 8.5	-1.41	-6.84
44	SLS2107B - 8.9	-1.35	-6.87
45	SLS2107B - 9.3	-1.20	-8.49
46	SLS2107B - 14	0.17	-9.26
47	SLS2107B - 14.5	-0.05	-10.89
48	SLS2107B - 16.1	2.66	-10.27
49	SLS2107B - 16.6	2.35	-8.43
50	SLS2107B - 17.3	1.08	-9.67
51	SLS2107B - 19.6	-2.24	-11.16
52	SLS2107B - 20.1	-2.99	-10.18
53	SLS2107B - 20.8	-2.58	-9.03
54	SLS2107B - 30.6	-1.92	-9.12
55	SLS2107B - 31	-1.85	-7.52
56	SLS2107B - 31.5	-2.93	-9.38
57	SLS2107B - 34.6	-1.56	-15.27
58	SLS2107B - 35	1.81	-10.98
59	CaCO3II 3	-2.61	-12.52
60	CaCO3II 4	-2.68	-12.57
Analysis 6			
No	Sample	d^{13}C	d^{18}O
		(‰ VPDB)	(‰ VPDB)
1	NBS-19 1	1.96	-2.25
2	NBS-19 2	2.03	-2.23
3	NBS-19 3	2.16	-2.13
4	CaCO3 I 1	-40.13	-21.29
5	CaCO3 I 2	-40.31	-21.42
6	CaCO3 I 3	-40.31	-21.44

7	CaCO3 II 1	-2.72	-12.73
8	CaCO3 II 2	-2.55	-12.53
9	SLS2107C - 11.3	-3.45	-12.13
10	SLS2107C - 11.6	-3.73	-10.94
11	SLS2107C - 11.9	-4.00	-13.34
12	SLS2107C - 46.6	-8.97	-5.19
13	SLS2107C - 47	-9.30	-5.01
14	SLS2107C - 47.5	-8.21	-5.89
15	SLS2107C - 47.9	-8.22	-4.58
16	SLS2107C - 48.4	-5.65	-13.76
17	SLS2108 - 0	-5.47	-14.82
18	SLS2108 - 2	-5.67	-14.28
19	SLS2108 - 4	-5.56	-14.36
20	SLS2108 - 6	-6.09	-14.39
21	SLS2108 - 8	-5.69	-14.64
22	SLS2108 - 17	-5.51	-13.71
23	SLS2109 - 0	0.83	-10.85
24	SLS2109 - 1	0.85	-10.00
25	SLS2109 - 2	1.20	-10.17
26	SLS2109 - 3	1.43	-10.65
27	SLS2109 - 4	1.36	-10.79
28	SLS2109 - 5	1.19	-11.56
29	SLS2109 - 6	1.07	-11.93
30	SLS2109 - 10	1.38	-10.42
31	SLS2109 - 11	1.35	-10.53
32	SLS2109 - 13	1.22	-11.81
33	SLS2109 - 16	0.54	-9.78
34	SLS2109 - 19	1.56	-9.63
35	SLS2109 - 20	1.37	-9.30
36	SLS2109 - 21	0.84	-9.85
37	SLS2109 - 22	1.05	-10.37
38	SLS2109 - 24	0.73	-11.01
39	SLS2110 - 21	-0.99	-7.09
40	SLS2110 - 22	-0.92	-6.98
41	SLS2110 - 23	-1.46	-7.66
42	SLS2110 - 24	-1.39	-7.30
43	SLS2110 - 35	-0.19	-8.32
44	SLS2110 - 36	-0.87	-8.39
45	SLS2110 - 73	-3.92	-4.32
46	SLS2110 - 74	-3.96	-4.67
47	SLS2110 - 75	-4.36	-4.36
48	CaCO3II 3	-2.65	-12.69
49	CaCO3II 4	-2.61	-12.56
Analysis 7			
No	Sample	$d^{13}C$	$d^{18}O$
		(‰ VPDB)	(‰ VPDB)

1	NBS-19 1	2.02	-2.15
2	NBS-19 2	2.10	-2.23
3	NBS-19 3	2.15	-2.05
4	CaCO3 I 1	-40.33	-21.51
5	CaCO3 I 2	-40.18	-21.35
6	CaCO3 I 3	-40.22	-21.33
7	CaCO3 II 1	-2.69	-12.59
8	CaCO3 II 2	-2.66	-12.61
9	SLS2201 - 14.5	-0.19	-10.69
10	SLS2201 - 15	0.09	-9.87
11	SLS2201 - 15.5	0.07	-10.17
12	SLS2201 - 18.5	-0.26	-11.67
13	SLS2201 - 19	-0.61	-12.14
14	SLS2201 - 21.5	-0.89	-12.66
15	SLS2201 - 22.5	-0.27	-11.55
16	SLS2201 - 23.5	-0.48	-11.26
17	SLS2201 - 24	-1.04	-10.90
18	SLS2201 - 25	-0.20	-10.36
19	SLS2201 - 27	-1.09	-11.58
20	SLS2201 - 29	-1.02	-12.50
21	SLS2201 - 30	-0.66	-11.69
22	SLS2201 - 32	1.05	-7.91
23	SLS2201 - 35	-0.59	-10.14
24	SLS2201 - 37	-0.69	-11.69
25	SLS2201 - 39	-1.32	-8.41
26	SLS2201 - 40	-0.78	-11.24
27	SLS2201 - 46	0.31	-13.00
28	SLS2201 - 52	0.29	-12.98
29	SLS2201 - 53	0.56	-12.12
30	SLS2201 - 54.5	0.57	-11.97
31	SLS2201 - 56	0.50	-12.04
32	SLS2201 - 58	0.87	-11.95
33	SLS2201 - 64	1.14	-10.61
34	SLS2201 - 68	-2.16	-11.13
35	SLS2201 - 69	-2.58	-11.24
36	SLS2201 - 73	-2.33	-11.85
37	SLS2201 - 74	-2.11	-10.75
38	SLS2201 - 75	-1.78	-8.89
39	SLS2201 - 105	-1.67	-10.00
40	SLS2201 - 105.5	-1.70	-10.57
41	SLS2201 - 106	-1.41	-8.96
42	SLS2201 - 116.5	0.38	-10.99
43	SLS2201 - 117	0.17	-11.48
44	SLS2201 - 120	0.55	-12.00
45	SLS2201 - 121	0.86	-12.49
46	SLS2201 - 123	1.82	-10.56
47	SLS2201 - 124	2.28	-11.86

48	SLS2201 - 125	2.21	-10.82
49	SLS2202 - 1	-1.97	-8.39
50	SLS2202 - 3	-1.91	-8.06
51	SLS2202 - 5	-2.82	-8.40
52	SLS2202 - 7	-2.90	-9.19
53	SLS2202 - 9	-2.33	-7.82
54	SLS2202 - 11	-2.69	-8.69
55	SLS2202 - 13	-3.11	-8.57
56	SLS2202 - 15	-2.96	-7.07
57	SLS2202 - 17	-3.03	-8.00
58	SLS2202 - 19	-2.99	-10.76
59	CaCO3II 3	-2.71	-12.66
60	CaCO3II 4	-2.65	-12.56
Analysis 8			
No	Sample	$d^{13}C$	$d^{18}O$
		(‰ VPDB)	(‰ VPDB)
1	NBS-19 1	2.05	-2.10
2	NBS-19 2	2.13	-2.29
3	NBS-19 3	2.12	-2.15
4	CaCO3 I 1	-40.20	-21.37
5	CaCO3 I 2	-40.28	-21.29
6	CaCO3 I 3	-40.24	-21.40
7	CaCO3 II 1	-2.70	-12.62
8	CaCO3 II 2	-2.68	-12.72
9	SLS2202 - 21	-2.19	-6.88
10	SLS2202 - 23	-2.92	-10.90
11	SLS2203 - 136	-2.98	-17.50
12	SLS2203 - 137	-2.84	-11.78
13	SLS2203 - 138	-2.77	-11.01
14	SLS2203 - 139	-3.34	-11.47
15	SLS2203 - 140	-2.96	-12.91
16	SLS2203 - 141	-3.17	-12.23
17	SLS2203 - 143	-3.34	-12.23
18	SLS2203 - 145	-2.84	-10.09
19	SLS2203 - 147	-3.24	-10.74
20	SLS2203 - 149	-3.09	-10.56
21	SLS2203 - 151	na	na
22	SLS2203 - 153	-2.90	-8.36
23	SLS2203 - 155	-2.97	-9.37
24	SLS2204 - -3	-2.83	-7.72
25	SLS2204 - -2	-2.65	-7.33
26	SLS2204 - -1	-4.66	-9.56
27	SLS2204 - 1	-3.17	-8.90
28	SLS2204 - 2	-3.74	-6.58
29	SLS2204 - 3	-3.92	-7.54
30	SLS2204 - 4	-3.20	-8.23

31	SLS2204 - 7	-2.19	-6.48
32	SLS2204 - 8	-0.31	-5.12
33	SLS2204 - 20	-3.31	-6.47
34	SLS2204 - 32	-1.29	-7.97
35	SLS2204 - 33	-1.38	-7.95
36	SLS2204 - 35	-1.04	-8.29
37	SLS2204 - 41	-0.86	-6.16
38	SLS2204 - 42	-1.55	-8.43
39	SLS2204 - 43	-1.49	-10.24
40	SLS2204 - 44	-0.43	-7.66
41	SLS2204 - 45	0.41	-7.58
42	SLS2204 - 47	-0.82	-8.56
43	SLS2204 - 51	-2.52	-9.94
44	SLS2204 - 52	-3.86	-10.38
45	SLS2204 - 54	-2.93	-9.77
46	SLS2204 - 55	-2.58	-8.44
47	SLS2204 - 57	-2.67	-10.82
48	SLS2204 - 81	-2.68	-9.31
49	SLS2204 - 82	-3.73	-10.28
50	SLS2204 - 83	-3.40	-9.17
51	SLS2204 - 84	-5.57	-12.74
52	SLS2204 - 85	-4.42	-9.13
53	SLS2204 - 129	-3.32	-11.93
54	SLS2204 - 130	-3.46	-12.75
55	SLS2204 - 131	-3.59	-14.92
56	SLS2204 - 136	-4.05	-11.02
57	SLS2204 - 138	-4.40	-10.60
58	SLS2204 - 140	-4.29	-12.72
59	CaCO3II 3	-2.81	-12.67
60	CaCO3II 4	-2.58	-12.70
Analysis 9			
No	Sample	d^{13}C	d^{18}O
		(‰ VPDB)	(‰ VPDB)
1	NBS-19 1	2.06	-2.18
2	NBS-19 2	2.14	-2.10
3	NBS-19 3	2.15	-1.99
4	CaCO3 I 1	-40.21	-21.35
5	CaCO3 I 2	-40.19	-21.13
6	CaCO3 I 3	-40.32	-21.22
7	CaCO3 II 1	-2.73	-12.98
8	CaCO3 II 2	-2.69	-12.79
9	SLS2204 - 141	-4.27	-11.21
10	SLS2204 - 146	-1.46	-9.91
11	SLS2204 - 147	-2.50	-10.41
12	SLS2204 - 148	-2.29	-9.88
13	SLS2204 - 151	-1.88	-8.69

14	SLS2204 - 153	-2.03	-7.03
15	SLS2204 - 155	-1.81	-7.53
16	SLS2204 - 157	-1.86	-6.98
17	SLS2204 - 158	-2.35	-7.15
18	SLS2204 - 178	-2.45	-5.16
19	SLS2204 - 179	-2.08	-7.05
20	SLS2204 - 180	-2.08	-6.71
21	SLS2204 - 181	-2.87	-6.37
22	SLS2204 - 182	-3.94	-6.80
23	SLS2204 - 201	-1.33	-7.10
24	SLS2204 - 241	-0.96	-7.10
25	SLS2204 - 242	-1.44	-8.03
26	SLS2204 - 244	-1.19	-6.59
27	SLS2204 - 245	-1.17	-6.19
28	SLS2204 - 246	-1.28	-5.67
29	SLS2204 - 261	-2.56	-11.29
30	SLS2204 - 264	-1.03	-10.60
31	SLS2204 - 267	-0.38	-7.54
32	SLS2204 - 271	-0.13	-5.77
33	SLS2204 - 276	0.50	-8.03
34	SLS2204 - 277	0.01	-7.80
35	SLS2204 - 278	1.33	-5.07
36	SLS2204 - 296	-6.68	-10.84
37	SLS2204 - 310	1.04	-3.59
38	SLS2204 - 311	-4.45	-8.07
39	SLS2204 - 312	-4.97	-9.17
40	SLS2204 - 313	-5.44	-8.95
41	SLS2204 - 314	-6.51	-9.38
42	SLS2204 - 316	-5.23	-7.67
43	SLS2204 - 319	-4.99	-5.23
44	SLS2204 - 320	-6.52	-8.75
45	SLS2204 - 325	-4.98	-7.68
46	SLS2204 - 327	-5.67	-6.77
47	SLS2204 - 329	-6.09	-9.56
48	SLS2204 - 331	-6.78	-8.50
49	SLS2204 - 333	-8.48	-9.22
50	SLS2205 - 13	-4.65	-7.64
51	SLS2205 - 15	-2.18	-5.10
52	SLS2205 - 18	-3.69	-7.56
53	SLS2205 - 20	-6.27	-13.46
54	SLS2205 - 21	-6.87	-12.48
55	SLS2205 - 24	-5.08	-10.17
56	SLS2205 - 26	na	na
57	SLS2205 - 29	na	na
58	SLS2205 - 30	-4.19	-8.18
59	CaCO3II 3	-2.83	-12.81
60	CaCO3II 4	-2.59	-12.96

Analysis 10

No	Sample	$d^{13}C$	$d^{18}O$
		(‰ VPDB)	(‰ VPDB)
1	NBS19 1	2.05	-2.05
2	NBS19 2	1.98	-2.28
3	NBS19 3	1.94	-2.25
4	CaCO3I 1	-40.25	-21.37
5	CaCO3I 2	-40.24	-21.35
6	CaCO3I 3	-40.28	-21.39
7	CaCO3II 1	-2.59	-12.66
8	CaCO3II 2	-2.53	-12.65
9	SLS2205 - 26	-2.99	-7.76
10	SLS2205 - 29	-5.21	-8.32
11	SLS2205 - 31	-2.28	-10.67
12	SLS2205 - 33	-3.18	-7.43
13	SLS2205 - 35	-0.52	-6.99
14	SLS2205 - 40	-0.67	-8.23
15	SLS2203 - 151	-2.56	-8.84
16	CaCO3II 3	-2.56	-12.63
17	CaCO3II 4	-2.57	-12.67

Table 2. C and O isotopic data. Samples prepared at UCSB and analyses performed at UCB. See methods section for details of analyses. Measured stratigraphic height of each sample is listed immediately following section name in second column.

Table 3.

Analysis: SLGC2112	$^{206}Pb/^{238}U$	error (2σ)	$^{207}Pb/^{235}U$	error (2σ)	rho
SLGC2112_S_20um_1	0.213285736	0.007463466	3.390956977	0.11700588	0.997554205
SLGC2112_S_20um_2	0.176098609	0.041276497	2.628156383	0.630249627	0.999915031
SLGC2112_S_20um_3	0.272160171	0.00936712	4.124302088	0.13811873	0.989357203
SLGC2112_S_20um_4	0.094643955	0.002540435	1.35775181	0.03473623	0.91210765
SLGC2112_S_20um_5	0.212742089	0.008547345	3.214287321	0.11910201	0.991111419
SLGC2112_S_20um_6	0.088704958	0.003425068	1.32754999	0.045032563	0.829513731
SLGC2112_S_20um_7	0.292067259	0.004884082	4.511056319	0.082767427	0.943835816
SLGC2112_S_20um_8	0.309750043	0.006121223	4.693986293	0.094432441	0.963365026
SLGC2112_S_20um_9	0.123753805	0.004407196	1.811294078	0.064228091	0.98943532
SLGC2112_S_20um_10	0.14342278	0.011584167	2.139826148	0.162400868	0.997333581
SLGC2112_S_20um_11	0.094915942	0.008152354	1.467096756	0.125390563	0.998180038
SLGC2112_S_20um_12	0.318619909	0.005729294	4.850350267	0.08541006	0.971034304
SLGC2112_S_20um_13	0.18802206	0.00401531	2.850346639	0.062402323	0.955682247
SLGC2112_S_20um_14	0.171733065	0.003076428	2.551310103	0.044035934	0.938198067
SLGC2112_S_20um_15	0.181385018	0.008618183	2.781367745	0.129752557	0.994911003
SLGC2112_S_20um_16	0.17518097	0.02707774	2.587763365	0.405668518	0.999497672
SLGC2112_S_20um_17	0.057292972	0.003298743	0.852834725	0.054572098	0.995199398
SLGC2112_S_20um_18	0.104522472	0.008953897	1.570538858	0.131300179	0.997687608
SLGC2112_S_20um_19	0.102654171	0.003269522	1.562127526	0.058474647	0.981068644
SLGC2112_S_20um_20	0.097367582	0.003334652	1.574714142	0.069547364	0.956559524
SLGC2112_S_20um_21	0.092599242	0.003193861	1.389808419	0.05373981	0.98413259
SLGC2112_S_20um_22	0.313064955	0.005290488	4.736065559	0.083764818	0.981370385
SLGC2112_S_20um_23	0.111697531	0.00351578	1.682565431	0.051858543	0.991428001
SLGC2112_S_20um_24	0.176114593	0.004510619	2.721504078	0.063094715	0.966861578
SLGC2112_S_20um_25	0.173795547	0.015156831	2.620200614	0.218319735	0.995591943
SLGC2112_S_20um_26	0.067794033	0.001143902	1.013123774	0.01622521	0.970123203
SLGC2112_S_20um_27	0.122322187	0.004791337	1.870124873	0.068179991	0.78597464
SLGC2112_S_20um_28	0.09245788	0.003292961	1.448489011	0.042375043	0.969609521
SLGC2112_S_20um_29	0.087917722	0.003751125	1.346764591	0.044454363	0.983430016
SLGC2112_S_20um_30	0.09655224	0.010005331	1.444783165	0.147340305	0.998319463
SLGC2112_S_20um_31	0.143609233	0.01643982	2.138422255	0.249835705	0.998779149
SLGC2112_S_20um_32	0.239020818	0.006339551	3.610239725	0.098098748	0.961742183
SLGC2112_S_20um_33	0.098368815	0.00624979	1.522347886	0.095230756	0.997389108
SLGC2112_S_20um_34	0.25646108	0.011458926	3.818673333	0.17052776	0.99720031
SLGC2112_S_20um_35	0.082809207	0.001807731	1.368926431	0.039399059	0.860323259
SLGC2112_S_20um_36	0.098136966	0.009450252	1.483904473	0.141904385	0.999058219
SLGC2112_M_25um_1	0.239323562	0.019378334	3.618923296	0.256895458	0.952792293
SLGC2112_M_25um_2	0.288636322	0.014922098	4.381661604	0.095289486	0.997702219
SLGC2112_M_25um_3	0.219659857	0.018786779	3.275240202	0.234747794	0.998432511
SLGC2112_M_25um_4	0.045578258	0.002818419	0.621342681	0.024304921	0.990409587
SLGC2112_M_25um_5	0.315508428	0.017325567	4.763558926	0.147277492	0.986777197
SLGC2112_M_25um_6	0.29226949	0.01685164	4.392110929	0.145383806	0.992941804
SLGC2112_M_25um_7	0.185508679	0.013555332	2.869517593	0.15652275	0.997320639
SLGC2112_M_25um_8	0.07079447	0.004925656	1.086251403	0.061227816	0.986781956
SLGC2112_M_25um_9	0.125870399	0.006457603	2.013433852	0.044352226	0.974100576
SLGC2112_M_25um_10	0.11701779	0.00754031	1.892146562	0.073608012	0.971008629
SLGC2112_M_25um_11	0.188178447	0.018427238	2.813204246	0.239804876	0.998673394
SLGC2112_M_25um_12	0.185812661	0.010769882	2.771266555	0.094290142	0.98990149
SLGC2112_M_25um_13	0.266281415	0.015724887	3.998606359	0.133276086	0.99797287
SLGC2112_M_25um_14	0.237842718	0.031969635	3.683916478	0.520792037	0.991103627
SLGC2112_M_25um_15	0.180209652	0.014871194	2.754094313	0.18948672	0.999326706
SLGC2112_M_25um_16	0.226033574	0.014091692	3.390407466	0.14724755	0.998107536
SLGC2112_M_25um_17	0.149123652	0.011277595	2.289402115	0.129331975	0.99827004
SLGC2112_M_25um_18	0.307942864	0.015983864	4.663586737	0.102355807	0.995986927
SLGC2112_M_25um_19	0.199023159	0.012201892	3.929557457	0.239609405	0.931333524
SLGC2112_M_25um_20	0.22168672	0.011804752	3.315192829	0.085659505	0.997969104
SLGC2112_M_25um_21	0.303458089	0.01635025	4.643002927	0.122829873	0.995731305
SLGC2112_M_25um_22	0.300538707	0.01542456	4.523289492	0.089101964	0.998073341
SLGC2112_M_25um_23	0.263988259	0.01439698	3.98914165	0.114404276	0.981923487
SLGC2112_M_25um_24	0.298809718	0.021560244	4.53912432	0.258002904	0.996355051
SLGC2112_M_25um_25	0.083541365	0.018374419	1.34166696	0.298810565	0.97696734
SLGC2112_M_25um_26	0.0883148	0.005423263	1.418386468	0.055731253	0.994268898

SLGC2112_M_25um_27	0.214074911	0.019723497	3.318211818	0.235232843	0.998086384
SLGC2112_M_25um_28	0.096671621	0.007480144	1.481739249	0.091937232	0.999221846
SLGC2112_M_25um_29	0.19075615	0.015088828	2.879808191	0.186226109	0.998185729
SLGC2112_M_25um_30	0.24714681	0.014496802	3.741462798	0.123046877	0.996606975
SLGC2112_M_25um_31	0.255566161	0.028037503	3.819529492	0.379516801	0.999503836
SLGC2112_M_25um_32	0.11574831	0.005983171	1.986317657	0.046416495	0.956063932
SLGC2112_M_25um_33	0.117471305	0.006549523	1.882342501	0.073440062	0.936679177
SLGC2112_M_25um_34	0.258278868	0.019968481	3.882397026	0.244575459	0.997649738
SLGC2112_M_25um_35	0.203916483	0.019918885	3.137618483	0.245526732	0.997682467
Analysis: SLGC2121	^{206}Pb/^{238}U	error (2σ)	^{207}Pb/^{235}U	error (2σ)	rho
SLGC2121_S_20um_1	0.155999032	0.005620581	2.196761753	0.083557497	0.990484958
SLGC2121_S_20um_2	0.140452998	0.004755308	1.96791874	0.071871976	0.992314511
SLGC2121_S_20um_3	0.322987744	0.005485354	5.087330642	0.086801512	0.97172911
SLGC2121_S_20um_4	0.120688924	0.009589626	1.752136532	0.151076572	0.998969497
SLGC2121_S_20um_5	0.259486228	0.019418079	4.00655908	0.312331178	0.998889983
SLGC2121_S_20um_6	0.209227603	0.008552503	3.257020972	0.135734505	0.987639776
SLGC2121_S_20um_7	0.241413731	0.013183459	4.630772633	0.48380491	0.854163881
Analysis: SLGC2125	^{206}Pb/^{238}U	error (2σ)	^{207}Pb/^{235}U	error (2σ)	rho
SLGC2125_S_20um_1	0.318209456	0.006288144	4.822122041	0.095824605	0.967767123
SLGC2125_S_20um_2	0.289059008	0.009220413	4.390141148	0.145644227	0.983229049
SLGC2125_S_20um_3	0.076495678	0.003325232	1.174550385	0.049981447	0.986783678
SLGC2125_S_20um_4	0.254651683	0.010012855	3.808495096	0.154444277	0.996174848
SLGC2125_S_20um_5	0.271001008	0.010974828	4.074541853	0.170391999	0.99638179
SLGC2125_S_20um_6	0.311082836	0.007292082	4.729824871	0.116820219	0.981848994
SLGC2125_S_20um_7	0.287119685	0.00860444	4.382415623	0.14288025	0.992157425
SLGC2125_S_20um_8	0.257873204	0.008927055	3.891079583	0.142371596	0.996245001
SLGC2125_S_20um_9	0.316307379	0.005708737	4.736003804	0.094859891	0.983070567
SLGC2125_S_20um_10	0.277416224	0.014967655	4.134135276	0.231849903	0.996007052
SLGC2125_S_20um_11	0.25926343	0.021229075	3.84951769	0.334555303	0.998353888
SLGC2125_S_20um_12	0.318792143	0.007114097	4.778503075	0.1116663	0.978783126
SLGC2125_S_20um_13	0.314132952	0.007432494	4.694503762	0.115470915	0.981978657
SLGC2125_S_20um_14	0.309563131	0.005294918	4.658727519	0.092911583	0.977357765
SLGC2125_S_20um_15	0.305448567	0.005493391	4.608846803	0.087126949	0.991345373
SLGC2125_S_20um_16	0.312890296	0.005926554	4.731421779	0.090639008	0.967466243
SLGC2125_S_20um_17	0.231166036	0.034232436	3.422660576	0.528951504	0.999669645
SLGC2125_S_20um_18	0.303147611	0.007603146	4.55239951	0.11564094	0.984736723
SLGC2125_S_20um_19	0.301422413	0.005102128	4.495805504	0.07808117	0.987480167
SLGC2125_S_20um_20	0.112478173	0.017043398	1.591477577	0.257775341	0.999699927
SLGC2125_S_20um_21	0.196903914	0.011616888	2.897024903	0.179759361	0.996952771
SLGC2125_S_20um_22	0.25312072	0.008255792	3.797467333	0.126534247	0.991554074
SLGC2125_S_20um_23	0.201067912	0.004545039	3.012402072	0.069331467	0.988097811
SLGC2125_S_20um_24	0.265953675	0.024941601	3.982696987	0.379998241	0.999270823
SLGC2125_S_20um_25	0.296744871	0.006887879	4.432753099	0.109787229	0.97963056
SLGC2125_S_20um_26	0.261025946	0.006812459	3.868688043	0.106239912	0.9772217
SLGC2125_S_20um_27	0.266997052	0.010179029	3.994327278	0.153915895	0.994651582
SLGC2125_S_20um_28	0.295167526	0.008356365	4.520434184	0.135165741	0.991901561
SLGC2125_S_20um_29	0.238678106	0.013405898	3.516649471	0.201702966	0.996070408
SLGC2125_S_20um_30	0.300792776	0.0089527	4.50426546	0.13922759	0.991819223
SLGC2125_S_20um_31	0.311769076	0.006724984	4.673107028	0.104793247	0.984365225
SLGC2125_S_20um_32	0.089566739	0.008398565	1.191914836	0.132755736	0.998641015
Analysis: SLGC2008	^{206}Pb/^{238}U	error (2σ)	^{207}Pb/^{235}U	error (2σ)	rho
SLGC2008_M_1	63.37136	1.56828765	0.04827	0.001152778	0.451332417
SLGC2008_M_2	60.93845	1.781762541	0.0549	0.001485128	0.393997821
SLGC2008_M_3	63.13131	1.794664054	0.04851	0.001343945	0.466431311
SLGC2008_M_4	62.34414	1.629732628	0.0528	0.001598479	0.391784253
SLGC2008_M_5	64.89293	2.126444204	0.04872	0.001235741	0.509452819
SLGC2008_M_6	62.89308	1.784487908	0.04837	0.001328143	0.537606167
SLGC2008_M_7	64.80881	1.694886247	0.04816	0.001245734	0.444499213
SLGC2008_M_8	63.13131	1.608421384	0.0495	0.001797248	0.49138254

SLGC2008_M_9	63.0517	1.490770326	0.0476	0.001531765	0.418262967
SLGC2008_M_10	12.87001	0.335590797	0.08248	0.001812093	0.365276167
SLGC2008_M_11	61.05006	2.044555643	0.04828	0.001306439	0.482885162
SLGC2008_M_12	62.5	1.5625	0.0478	0.001950368	0.269276803
Analysis: SLGC2018	^{206}Pb/^{238}U	error (2σ)	^{207}Pb/^{235}U	error (2σ)	rho
SLGC2018_M_1	64.80881	2.155368889	0.04823	0.001048119	0.504350113
SLGC2018_M_2	64.72492	1.833662081	0.04995	0.00111714	0.507106999
SLGC2018_M_3	9.775171	0.316139479	0.07244	0.001553262	0.49443758
SLGC2018_M_4	65.06181	1.65085656	0.04816	0.001089887	0.462775384
SLGC2018_M_5	63.37136	1.748674969	0.04936	0.001377013	0.453458957
SLGC2018_M_6	60.02401	1.639695912	0.05025	0.001309819	0.409512935
SLGC2018_M_7	62.53909	1.587613696	0.04843	0.001023272	0.529677329
SLGC2018_M_8	62.3053	2.0520834	0.04978	0.001194495	0.485358392
SLGC2018_M_9	64.26735	1.701687725	0.04859	0.00108388	0.457849995
SLGC2018_M_10	61.34969	1.772882569	0.05529	0.001444885	0.363857301
SLGC2018_M_11	60.09615	1.93531724	0.0634	0.002892719	0.395269763
SLGC2018_M_12	61.84292	1.937681273	0.04844	0.001094839	0.540031911
SLGC2018_M_13	61.9195	1.614069985	0.0549	0.002730495	0.247529735
SLGC2018_M_14	63.69427	1.628332518	0.0481	0.00116101	0.487697681
SLGC2018_M_15	63.49206	1.753590524	0.04939	0.001150586	0.512546952
SLGC2018_M_16	63.09148	1.879676556	0.04925	0.001220092	0.433938065
SLGC2018_M_17	63.85696	1.825860081	0.04864	0.001132581	0.532519314
SLGC2018_M_18	7.304602	0.21280527	0.08776	0.001771532	0.521176323
SLGC2018_M_19	61.76652	2.177440061	0.05197	0.001124834	0.506829424
SLGC2018_M_20	62.07325	2.101303758	0.04988	0.001370695	0.502102317
SLGC2018_M_21	63.01197	1.935567849	0.04891	0.001158134	0.472382227
SLGC2018_M_22	62.42197	2.027515243	0.04938	0.00108529	0.527586977
Analysis: SLGC2019	^{206}Pb/^{238}U	error (2σ)	^{207}Pb/^{235}U	error (2σ)	rho
SLGC2019_M_1	89.6861	2.576827219	0.0478	0.001457373	0.477876629
SLGC2019_M_2	83.33333	2.890090433	0.0478	0.001383451	0.442663662
SLGC2019_M_3	84.81764	2.224359577	0.04885	0.001262747	0.197088445
SLGC2019_M_4	84.67401	3.087051229	0.0772	0.008835946	0.168897474
SLGC2019_M_5	89.84726	2.470388673	0.04805	0.001379718	0.494572195
SLGC2019_M_6	85.76329	2.514648007	0.0478	0.001383451	0.325972884
SLGC2019_M_7	88.10573	2.508527091	0.04727	0.001232023	0.426072461
SLGC2019_M_8	88.88889	2.657506266	0.04745	0.001046041	0.511790789

Table 3. U-Pb geochronology LA-ICP-MS data, reduced using *Iolite*. See methods section for sample processing information and analysis details.

Table 4.

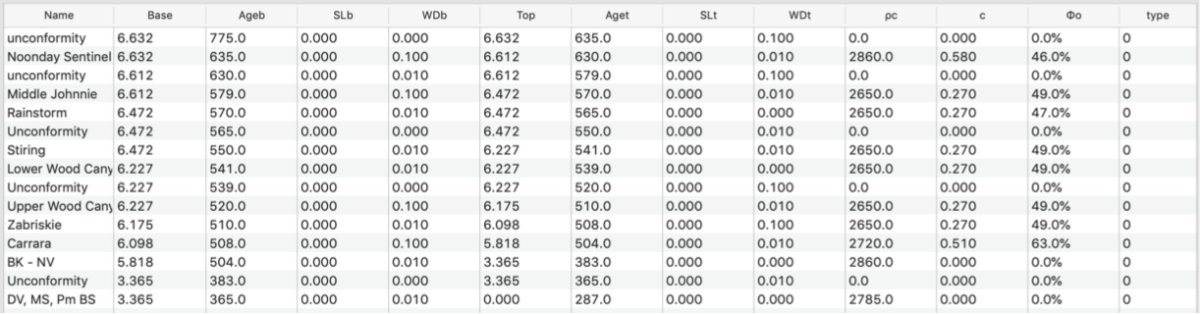

Name	Base	Ageb	SLb	WDb	Top	Aget	SLt	WDt	ρc	c	Φo	type
unconformity	6.632	775.0	0.000	0.000	6.632	635.0	0.000	0.100	0.0	0.000	0.0%	0
Noonday Sentinel	6.632	635.0	0.000	0.100	6.612	630.0	0.000	0.010	2860.0	0.580	46.0%	0
unconformity	6.612	630.0	0.000	0.010	6.612	579.0	0.000	0.100	0.0	0.000	0.0%	0
Middle Johnnie	6.612	579.0	0.000	0.100	6.472	570.0	0.000	0.010	2650.0	0.270	49.0%	0
Rainstorm	6.472	570.0	0.000	0.010	6.472	565.0	0.000	0.000	2650.0	0.270	47.0%	0
Unconformity	6.472	565.0	0.000	0.000	6.472	550.0	0.000	0.010	0.0	0.000	0.0%	0
Stiring	6.472	550.0	0.000	0.010	6.227	541.0	0.000	0.010	2650.0	0.270	49.0%	0
Lower Wood Cany	6.227	541.0	0.000	0.010	6.227	539.0	0.000	0.000	2650.0	0.270	49.0%	0
Unconformity	6.227	539.0	0.000	0.000	6.227	520.0	0.000	0.100	0.0	0.000	0.0%	0
Upper Wood Cany	6.227	520.0	0.000	0.100	6.175	510.0	0.000	0.010	2650.0	0.270	49.0%	0
Zabriskie	6.175	510.0	0.000	0.010	6.098	508.0	0.000	0.100	2650.0	0.270	49.0%	0
Carrara	6.098	508.0	0.000	0.100	5.818	504.0	0.000	0.010	2720.0	0.510	63.0%	0
BK - NV	5.818	504.0	0.000	0.010	3.365	383.0	0.000	0.000	2860.0	0.000	0.0%	0
Unconformity	3.365	383.0	0.000	0.000	3.365	365.0	0.000	0.010	0.0	0.000	0.0%	0
DV, MS, Pm BS	3.365	365.0	0.000	0.010	0.000	287.0	0.000	0.000	2785.0	0.000	0.0%	0

Backstrip data for Northwest Clark Mountain. Base and Top thicknesses represent measured section thickness in km.

Name	Base	Ageb	SLb	WDb	Top	Aget	SLt	WDt	ρc	c	Φo	type
unconformity	7.384	775.0	0.000	0.000	7.384	635.0	0.000	0.100	0.0	0.000	0.0%	0
Noonday Sentinel	7.384	635.0	0.000	0.100	7.354	630.0	0.000	0.010	2860.0	0.580	46.0%	0
Noonday Radcliff	7.354	630.0	0.000	0.010	7.354	610.0	0.000	0.100	2650.0	0.270	49.0%	0
Lower Johnnie	7.354	610.0	0.000	0.100	7.354	579.0	0.000	0.100	2650.0	0.270	49.0%	0
Middle Johnnie	7.354	579.0	0.000	0.100	7.034	570.0	0.000	0.010	2650.0	0.270	49.0%	0
Rainstorm	7.034	570.0	0.000	0.010	6.984	565.0	0.000	0.000	2650.0	0.270	47.0%	0
Unconformity	6.984	565.0	0.000	0.000	6.984	550.0	0.000	0.010	0.0	0.000	0.0%	0
Stiring	6.984	550.0	0.000	0.010	6.686	541.0	0.000	0.010	2650.0	0.270	49.0%	0
Lower Wood Cany	6.686	541.0	0.000	0.010	6.356	539.0	0.000	0.000	2650.0	0.270	49.0%	0
Unconformity	6.356	539.0	0.000	0.000	6.356	520.0	0.000	0.100	0.0	0.000	0.0%	0
Upper Wood Cany	6.356	520.0	0.000	0.100	6.175	510.0	0.000	0.010	2650.0	0.270	49.0%	0
Zabriskie	6.175	510.0	0.000	0.010	6.098	508.0	0.000	0.100	2650.0	0.270	49.0%	0
Carrara	6.098	508.0	0.000	0.100	5.818	504.0	0.000	0.010	2720.0	0.510	63.0%	0
BK - NV	5.818	504.0	0.000	0.010	3.365	383.0	0.000	0.000	2860.0	0.000	0.0%	0
Unconformity	3.365	383.0	0.000	0.000	3.365	365.0	0.000	0.010	0.0	0.000	0.0%	0
DV, MS, Pm BS	3.365	365.0	0.000	0.010	0.000	287.0	0.000	0.000	2785.0	0.000	0.0%	0

Backstrip data for the eastern Winter’s Pass Hills. Base and Top thicknesses represent measured section thickness in km.

Name	Base	Ageb	SLb	WDb	Top	Aget	SLt	WDt	ρc	c	Φo	type
Tonian	10.000	775.0	0.000	0.100	9.680	720.0	0.000	0.010	0.0	0.000	0.0%	0
Kingston Peak	9.680	720.0	0.000	0.010	7.380	660.0	0.000	0.000	2650.0	0.270	49.0%	0
Unconformity	7.380	660.0	0.000	0.000	7.380	635.0	0.000	0.000	0.0	0.000	0.0%	0
Noonday Sentinel	7.380	635.0	0.000	0.000	7.350	630.0	0.000	0.010	2860.0	0.580	46.0%	0
Noonday Radcliff	7.350	630.0	0.000	0.010	7.290	610.0	0.000	0.100	2650.0	0.270	49.0%	0
Lower Johnnie	7.290	610.0	0.000	0.100	7.230	579.0	0.000	0.100	2650.0	0.270	49.0%	0
Middle Johnnie	7.230	579.0	0.000	0.100	7.090	570.0	0.000	0.010	2650.0	0.270	49.0%	0
Rainstorm	7.090	570.0	0.000	0.010	6.970	565.0	0.000	0.000	2650.0	0.270	47.0%	0
Unconformity	6.970	565.0	0.000	0.000	6.970	550.0	0.000	0.010	0.0	0.000	0.0%	0
Stiring	6.970	550.0	0.000	0.010	6.510	541.0	0.000	0.010	2650.0	0.270	49.0%	0
Lower Wood Cany	6.510	541.0	0.000	0.010	6.510	539.0	0.000	0.000	2650.0	0.270	49.0%	0
Unconformity	6.510	539.0	0.000	0.000	6.510	520.0	0.000	0.100	0.0	0.000	0.0%	0
Upper Wood Cany	6.510	520.0	0.000	0.100	6.175	510.0	0.000	0.010	2650.0	0.270	49.0%	0
Zabriskie	6.175	510.0	0.000	0.010	6.098	508.0	0.000	0.100	2650.0	0.270	49.0%	0
Carrara	6.098	508.0	0.000	0.100	5.818	504.0	0.000	0.010	2720.0	0.510	63.0%	0
BK - NV	5.818	504.0	0.000	0.010	3.365	383.0	0.000	0.000	2860.0	0.000	0.0%	0
Unconformity	3.365	383.0	0.000	0.000	3.365	365.0	0.000	0.010	0.0	0.000	0.0%	0
DV, MS, Pm BS	3.365	365.0	0.000	0.010	0.000	287.0	0.000	0.000	2785.0	0.000	0.0%	0

Backstrip data for the Kingston Range. Base and Top thicknesses represent measured section thickness in km.

Name	Base	Ageb	SLb	WDb	Top	Aget	SLt	WDt	ρc	c	Φo	type
unconformity	7.399	775.0	0.000	0.000	7.399	635.0	0.000	0.100	0.0	0.000	0.0%	0
Noonday Sentinel	7.399	635.0	0.000	0.100	7.384	630.0	0.000	0.010	2860.0	0.580	46.0%	0
Noonday Radcliff	7.384	630.0	0.000	0.010	7.334	610.0	0.000	0.100	2650.0	0.270	49.0%	0
Lower Johnnie	7.334	610.0	0.000	0.100	7.264	579.0	0.000	0.100	2650.0	0.270	49.0%	0
Middle Johnnie	7.264	579.0	0.000	0.100	7.064	570.0	0.000	0.010	2650.0	0.270	49.0%	0
Rainstorm	7.064	570.0	0.000	0.010	6.984	565.0	0.000	0.000	2650.0	0.270	47.0%	0
Unconformity	6.984	565.0	0.000	0.000	6.984	550.0	0.000	0.010	0.0	0.000	0.0%	0
Stiring	6.984	550.0	0.000	0.010	6.686	541.0	0.000	0.010	2650.0	0.270	49.0%	0
Lower Wood Cany	6.686	541.0	0.000	0.010	6.356	539.0	0.000	0.000	2650.0	0.270	49.0%	0
Unconformity	6.356	539.0	0.000	0.000	6.356	520.0	0.000	0.100	0.0	0.000	0.0%	0
Upper Wood Cany	6.356	520.0	0.000	0.100	6.175	510.0	0.000	0.010	2650.0	0.270	49.0%	0
Zabriskie	6.175	510.0	0.000	0.010	6.098	508.0	0.000	0.100	2650.0	0.270	49.0%	0
Carrara	6.098	508.0	0.000	0.100	5.818	504.0	0.000	0.010	2720.0	0.510	63.0%	0
BK - NV	5.818	504.0	0.000	0.010	3.365	383.0	0.000	0.000	2860.0	0.000	0.0%	0
Unconformity	3.365	383.0	0.000	0.000	3.365	365.0	0.000	0.010	0.0	0.000	0.0%	0
DV, MS, Pm BS	3.365	365.0	0.000	0.010	0.000	287.0	0.000	0.000	2785.0	0.000	0.0%	0

Backstrip data for the northern Winter's Pass Hills. Base and Top thicknesses represent measured section thickness in km.

Name	Base	Ageb	SLb	WDb	Top	Aget	SLt	WDt	ρc	c	Φo	type
Tonian	9.138	775.0	0.000	0.010	8.488	720.0	0.000	0.010	2650.0	0.270	49.0%	0
Kingston Peak	8.488	720.0	0.000	0.010	7.168	660.0	0.000	0.000	2650.0	0.270	49.0%	0
Unconformity	7.168	660.0	0.000	0.000	7.168	635.0	0.000	0.000	0.0	0.000	0.0%	0
Noonday Sentinel	7.168	635.0	0.000	0.000	7.163	630.0	0.000	0.010	2860.0	0.580	46.0%	0
Noonday Radcliff	7.163	630.0	0.000	0.010	7.073	610.0	0.000	0.100	2650.0	0.270	49.0%	0
Lower Johnnie	7.073	610.0	0.000	0.100	6.993	579.0	0.000	0.100	2650.0	0.270	49.0%	0
Middle Johnnie	6.993	579.0	0.000	0.100	6.873	570.0	0.000	0.010	2650.0	0.270	49.0%	0
Rainstorm	6.873	570.0	0.000	0.010	6.813	565.0	0.000	0.000	2650.0	0.270	47.0%	0
Unconformity	6.813	565.0	0.000	0.000	6.813	550.0	0.000	0.010	0.0	0.000	0.0%	0
Stiring	6.813	550.0	0.000	0.010	6.557	541.0	0.000	0.010	2650.0	0.270	49.0%	0
Lower Wood Cany	6.557	541.0	0.000	0.010	6.544	539.0	0.000	0.000	2650.0	0.270	49.0%	0
Unconformity	6.544	539.0	0.000	0.000	6.544	520.0	0.000	0.100	0.0	0.000	0.0%	0
Upper Wood Cany	6.544	520.0	0.000	0.100	6.155	510.0	0.000	0.010	2650.0	0.270	49.0%	0
Zabriskie	6.155	510.0	0.000	0.010	6.098	508.0	0.000	0.100	2650.0	0.270	49.0%	0
Carrara	6.098	508.0	0.000	0.100	5.818	504.0	0.000	0.010	2720.0	0.510	63.0%	0
BK - NV	5.818	504.0	0.000	0.010	3.365	383.0	0.000	0.000	2860.0	0.000	0.0%	0
Unconformity	3.365	383.0	0.000	0.000	3.365	365.0	0.000	0.010	0.0	0.000	0.0%	0
DV, MS, Pm BS	3.365	365.0	0.000	0.010	0.000	287.0	0.000	0.000	2785.0	0.000	0.0%	0

Backstrip data for the southern Salt Spring Hills. Base and Top thicknesses represent measured section thickness in km.

Name	Base	Ageb	SLb	WDb	Top	Aget	SLt	WDt	ρc	c	Φo	type
Tonian	9.138	775.0	0.000	0.010	8.488	720.0	0.000	0.010	2650.0	0.270	49.0%	0
Kingston Peak	8.488	720.0	0.000	0.010	7.168	660.0	0.000	0.000	2650.0	0.270	49.0%	0
Unconformity	7.168	660.0	0.000	0.000	7.168	635.0	0.000	0.000	0.0	0.000	0.0%	0
Noonday Sentinel	7.168	635.0	0.000	0.000	7.163	630.0	0.000	0.010	2860.0	0.580	46.0%	0
Noonday Radcliff	7.163	630.0	0.000	0.010	7.073	610.0	0.000	0.100	2650.0	0.270	49.0%	0
Lower Johnnie	7.073	610.0	0.000	0.100	6.993	579.0	0.000	0.100	2650.0	0.270	49.0%	0
Middle Johnnie	6.993	579.0	0.000	0.100	6.873	570.0	0.000	0.010	2650.0	0.270	49.0%	0
Rainstorm	6.873	570.0	0.000	0.010	6.813	565.0	0.000	0.000	2650.0	0.270	47.0%	0
Unconformity	6.813	565.0	0.000	0.000	6.813	550.0	0.000	0.010	0.0	0.000	0.0%	0
Stiring	6.813	550.0	0.000	0.010	6.557	541.0	0.000	0.010	2650.0	0.270	49.0%	0
Lower Wood Cany	6.557	541.0	0.000	0.010	6.544	539.0	0.000	0.000	2650.0	0.270	49.0%	0
Unconformity	6.544	539.0	0.000	0.000	6.544	520.0	0.000	0.100	0.0	0.000	0.0%	0
Upper Wood Cany	6.544	520.0	0.000	0.100	6.155	510.0	0.000	0.010	2650.0	0.270	49.0%	0
Zabriskie	6.155	510.0	0.000	0.010	6.098	508.0	0.000	0.100	2650.0	0.270	49.0%	0
Carrara	6.098	508.0	0.000	0.100	5.818	504.0	0.000	0.010	2720.0	0.510	63.0%	0
BK - NV	5.818	504.0	0.000	0.010	3.365	383.0	0.000	0.000	2860.0	0.000	0.0%	0
Unconformity	3.365	383.0	0.000	0.000	3.365	365.0	0.000	0.010	0.0	0.000	0.0%	0
DV, MS, Pm BS	3.365	365.0	0.000	0.010	0.000	287.0	0.000	0.000	2785.0	0.000	0.0%	0

Backstrip data for the Silurian Hills. Base and Top thicknesses represent measured section thickness in km.

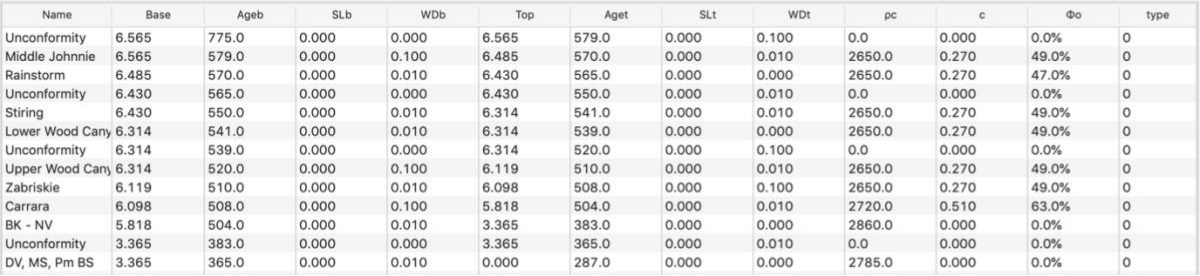

Name	Base	Ageb	SLb	WDb	Top	Aget	SLt	WDt	ρc	c	Φo	type
Unconformity	6.565	775.0	0.000	0.000	6.565	579.0	0.000	0.100	0.0	0.000	0.0%	0
Middle Johnnie	6.565	579.0	0.000	0.100	6.485	570.0	0.000	0.010	2650.0	0.270	49.0%	0
Rainstorm	6.485	570.0	0.000	0.010	6.430	565.0	0.000	0.000	2650.0	0.270	47.0%	0
Unconformity	6.430	565.0	0.000	0.000	6.430	550.0	0.000	0.010	0.0	0.000	0.0%	0
Stiring	6.430	550.0	0.000	0.010	6.314	541.0	0.000	0.010	2650.0	0.270	49.0%	0
Lower Wood Cany	6.314	541.0	0.000	0.010	6.314	539.0	0.000	0.000	2650.0	0.270	49.0%	0
Unconformity	6.314	539.0	0.000	0.000	6.314	520.0	0.000	0.100	0.0	0.000	0.0%	0
Upper Wood Cany	6.314	520.0	0.000	0.100	6.119	510.0	0.000	0.010	2650.0	0.270	49.0%	0
Zabriskie	6.119	510.0	0.000	0.010	6.098	508.0	0.000	0.100	2650.0	0.270	49.0%	0
Carrara	6.098	508.0	0.000	0.100	5.818	504.0	0.000	0.010	2720.0	0.510	63.0%	0
BK - NV	5.818	504.0	0.000	0.010	3.365	383.0	0.000	0.000	2860.0	0.000	0.0%	0
Unconformity	3.365	383.0	0.000	0.000	3.365	365.0	0.000	0.010	0.0	0.000	0.0%	0
DV, MS, Pm BS	3.365	365.0	0.000	0.010	0.000	287.0	0.000	0.000	2785.0	0.000	0.0%	0

Backstrip data for Old Dad Mountain. Base and Top thicknesses represent measured section thickness in km.

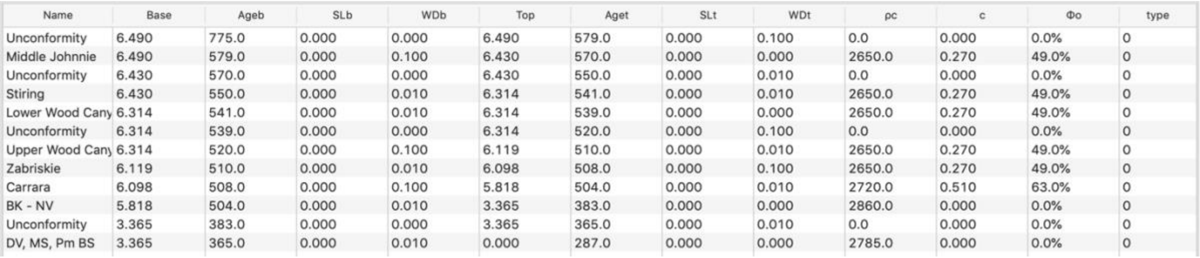

Name	Base	Ageb	SLb	WDb	Top	Aget	SLt	WDt	ρc	c	Φo	type
Unconformity	6.490	775.0	0.000	0.000	6.490	579.0	0.000	0.100	0.0	0.000	0.0%	0
Middle Johnnie	6.490	579.0	0.000	0.100	6.430	570.0	0.000	0.000	2650.0	0.270	49.0%	0
Unconformity	6.430	570.0	0.000	0.000	6.430	550.0	0.000	0.010	0.0	0.000	0.0%	0
Stiring	6.430	550.0	0.000	0.010	6.314	541.0	0.000	0.010	2650.0	0.270	49.0%	0
Lower Wood Cany	6.314	541.0	0.000	0.010	6.314	539.0	0.000	0.000	2650.0	0.270	49.0%	0
Unconformity	6.314	539.0	0.000	0.000	6.314	520.0	0.000	0.100	0.0	0.000	0.0%	0
Upper Wood Cany	6.314	520.0	0.000	0.100	6.119	510.0	0.000	0.010	2650.0	0.270	49.0%	0
Zabriskie	6.119	510.0	0.000	0.010	6.098	508.0	0.000	0.100	2650.0	0.270	49.0%	0
Carrara	6.098	508.0	0.000	0.100	5.818	504.0	0.000	0.010	2720.0	0.510	63.0%	0
BK - NV	5.818	504.0	0.000	0.010	3.365	383.0	0.000	0.000	2860.0	0.000	0.0%	0
Unconformity	3.365	383.0	0.000	0.000	3.365	365.0	0.000	0.010	0.0	0.000	0.0%	0
DV, MS, Pm BS	3.365	365.0	0.000	0.010	0.000	287.0	0.000	0.000	2785.0	0.000	0.0%	0

Backstrip data for the Kelso Mountains. Base and Top thicknesses represent measured section thickness in km.

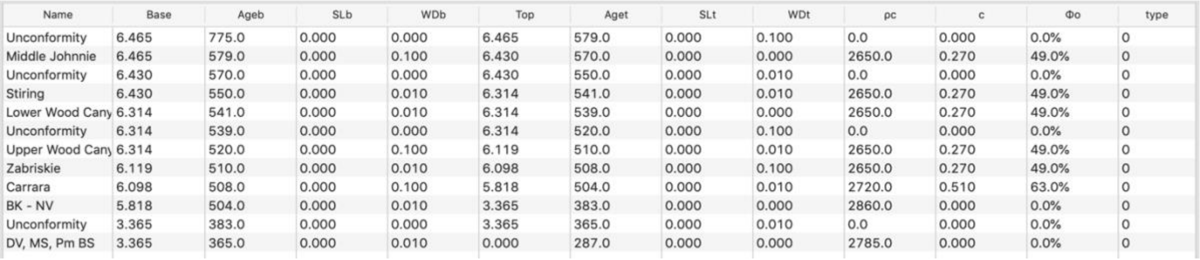

Name	Base	Ageb	SLb	WDb	Top	Aget	SLt	WDt	ρc	c	Φo	type
Unconformity	6.465	775.0	0.000	0.000	6.465	579.0	0.000	0.100	0.0	0.000	0.0%	0
Middle Johnnie	6.465	579.0	0.000	0.100	6.430	570.0	0.000	0.000	2650.0	0.270	49.0%	0
Unconformity	6.430	570.0	0.000	0.000	6.430	550.0	0.000	0.010	0.0	0.000	0.0%	0
Stiring	6.430	550.0	0.000	0.010	6.314	541.0	0.000	0.010	2650.0	0.270	49.0%	0
Lower Wood Cany	6.314	541.0	0.000	0.010	6.314	539.0	0.000	0.000	2650.0	0.270	49.0%	0
Unconformity	6.314	539.0	0.000	0.000	6.314	520.0	0.000	0.100	0.0	0.000	0.0%	0
Upper Wood Cany	6.314	520.0	0.000	0.100	6.119	510.0	0.000	0.010	2650.0	0.270	49.0%	0
Zabriskie	6.119	510.0	0.000	0.010	6.098	508.0	0.000	0.100	2650.0	0.270	49.0%	0
Carrara	6.098	508.0	0.000	0.100	5.818	504.0	0.000	0.010	2720.0	0.510	63.0%	0
BK - NV	5.818	504.0	0.000	0.010	3.365	383.0	0.000	0.000	2860.0	0.000	0.0%	0
Unconformity	3.365	383.0	0.000	0.000	3.365	365.0	0.000	0.010	0.0	0.000	0.0%	0
DV, MS, Pm BS	3.365	365.0	0.000	0.010	0.000	287.0	0.000	0.000	2785.0	0.000	0.0%	0

Backstrip data for the Providence Mountains. Base and Top thicknesses represent measured section thickness in km.